DEVELOPMENT OF A NEW TOOL

FOR METALLIC FUEL PERFORMANCE EVALUATIONS

A Dissertation

by

HYOCHEOL LEE

Submitted to the Office of Graduate and Professional Studies of
Texas A&M University
in partial fulfillment of the requirements for the degree of

DOCTOR OF PHILOSOPHY

Chair of Committee,	Pavel V. Tsvetkov
Committee Members,	Lin Shao
	Sean M. McDeavitt
	Miladin Radovic
Head of Department,	Michael Nastasi

December 2019

Major Subject: Nuclear Engineering

ABSTRACT

Accurate evaluations of fuel behavior is a crucial part in the determination of fuel operation limits and in the verification of burnup capabilities and reliability characteristics. In-pile behaviors of metallic fuels are closely connected with one another under a wide variety of irradiation histories. In most cases, each individual behavior cannot be evaluated by considering its own physical phenomena in isolation. Due to the high degree of interconnection among the fuel behaviors, the models that predict and quantify the fuel behaviors contain nonlinear mathematical expressions, and the coefficients and boundary conditions of each model are dependent on the calculations of other models. These complex relations generally require an integrated platform which has high-performance computing capabilities to handle the fuel behavior models simultaneously. In this research, a comprehensive computational tool has been developed to provide an optimized platform where each model can communicate with other models to calculate the synergistic effects of the fuel behaviors. The tool was named Tool for Analyzing Metallic U-Zr Fuel Performance (TAMU-ZFP).

The framework of the TAMU-ZFP code was erected by implementing improved thermo-mechanical models in the code with new advanced algorithms. The governing equations (GEs) of the thermo-mechanical models were established for each individual cell of the spatial and temporal mesh employed in the code, and the GEs of a cell were solved with the boundary conditions pertaining to the specific cell. These cell-based models effectively describe the spatial variation and time dependence of thermo-

mechanical behaviors. By supplying the specific behavioral history of each cell, the new thermo-mechanical models enable the framework to be an optimized environment for the coupling of fuel performance models. TAMU-ZFP adopted new advanced algorithms to implicitly calculate the synergic effects of the irradiation behaviors. The radial and axial interlocking in a fuel performance calculation, coupling of fuel perform models, contact analysis, and dynamic dimensioning and power adjustment after fuel pin deformation are executed in three main algorithms: open-gap algorithm, serial-contact algorithm, and random-contact algorithm. Also, transient modules that allow one job-step for the simulations of design-based off-normal fuel behaviors were installed in the TAMU-ZFP code.

ACKNOWLEDGEMENTS

CONTRIBUTORS AND FUNDING SOURCES

Contributors

This work was supervised by a dissertation committee consisting of Professor Tsvetkov (advisor), Professor Shao, and Professor McDeavitt of the Department of Nuclear Engineering and Professor Radovic of the Department of Materials Science and Engineering.

All work conducted for the dissertation was completed by the student independently.

Funding Sources

NOMENCLATURE

Section 2.1

$\rho^{cool}(z,t)$ = coolant density at elevation z on the pin axis at time t [g/cm^3]

$A_c^{channel}(z,t)$ = cross-sectional area of the single coolant channel at elevation z on the pin

axis at time t [cm^2]

$c_p^{cool}(z,t)$ = heat capacity of the coolant at elevation z at time t [J/g-K]

$T^{cool}(z,t)$ = coolant temperature at elevation z at time t [K]

$P_h(z,t)$ = heated perimeter of the single coolant channel at elevation z on the pin axis at

time t [cm]

$q''_{pin-surf}(z,t)$ = incoming heat flux from the fuel pin surface at elevation z on the pin axis

at time t [W/cm^2]

$\dot{m}_{channel}^{cool}(t)$ = coolant mass flow rate in the single channel at time t [g/s]

$r_{pin}(z,t)$ = fuel pin radius at elevation z at time t [cm]

L = pin pitch [cm]

$T_{(i)}^{cool}$ = coolant temperature at axial node $z_{(i)}$ [K]

$c_p^{cool-s(i)}$ = average heat capacity of the coolant in axial section *(i)* [J/g-K]

f_h = fraction of incoming linear heat

$\Delta z^{s(i)}$ = length of axial section *(i)* [cm]

N = number of pieces of the linear power function pertaining to axial section *(i)*

$p_{(i)}$ = linear heat generation rate at axial node $z_{(i)}$ [W/cm]

$T^{cool-s(i)s[n]}_{(sub\_i+1)[n-1]}$ = coolant temperature at axial sub-node $z^{s(i)s[n]}_{(sub\_i+1)[n-1]}$ in axial section *(i)* at time

$t_{[n-1]}$ of time section *[n]* [K]

$\Delta t^{s[n]}$ = size of time section *[n]* [s]

$a^{s(i)s[n]}$ = average coolant velocity in axial section *(i)* for time section *[n]* [cm/s]

$b^{s(i)s[n]}$ = average coolant temperature increase rate by the fuel pin surface heat flux in

axial section *(i)* for time section *[n]* [K/s]

$\Delta z^{sub-s(i)s[n]}_{[n-1]}$ = size of axial sub-sections in axial section *(i)* at time $t_{[n-1]}$ of time section *[n]*

[cm]

$T^{cool-s(i)s[n]}_{(sub\_top)[n]}$ = coolant temperature at the last axial sub-node, $z^{s(i)s[n]}_{(sub\_top)[n]}$, in axial section *(i)*

at time $t_{[n]}$ of time section *[n]* [K]

$q''_{pin-surf}(z,t)$ = heat flux on the fuel pin surface at elevation z on the pin axis at time t

[W/cm^2]

$\Delta T^{film}(z,t)$ = temperature drop across the coolant film layer by forced convection [K]

$T^{c}_{out}(z,t)$ = cladding outside temperature at elevation z at time t [K]

$h^{cool}_{conv}(z,t)$ = convective heat transfer coefficient of the coolant at elevation z on the pin

axis at time t [W/cm^2-K]

$T^{cool-s(i)}$ = average temperature of the coolant in axial section *(i)* [K]

$p^{s(i)}$ = average linear heat generation rate in axial section *(i)* [W/cm]

$r_{out}^{c-s(i)}$ = radius up to the outer surface of the cladding in axial section *(i)* [cm]

radial section *<c>* = the outermost radial section of the cladding

$T_{\langle c+1\rangle[n]}^{c-s\langle c\rangle s(i)s[n]}$ = cladding temperature at the last radial sub-node, $r_{\langle c+1\rangle[n]}^{c-s(i)s[n]}$, in radial section

        <c> of axial section *(i)* at time $t_{[n]}$ of time section *[n]* [K]

$\chi_{[n]}^{s\langle c\rangle s(i)s[n]}$ = ratio of the convective heat transfer coefficient of the coolant to the conductive

        heat transfer coefficient of the cladding in axial section *(i)* at time $t_{[n]}$ of time

        section *[n]*

$\Delta r_{[n]}^{c-s\langle c\rangle s(i)s[n]}$ = size of radial section *<c>* of the cladding in axial section *(i)* at time $t_{[n]}$ of

        time section *[n]* [cm]

$k_{[n]}^{c-s\langle c\rangle s(i)s[n]}$ = average thermal conductivity of the cladding in radial section *<c>* of axial

        section *(i)* at time $t_{[n]}$ of time section *[n]* [W/cm-K]

$T_{\langle c+\frac{1}{2}\rangle[n]}^{c-s\langle c\rangle s(i)s[n]}$ = cladding temperature at radial sub-node $r_{\langle c+\frac{1}{2}\rangle[n]}^{c-s(i)s[n]}$ in radial section *<c>* of

        axial section *(i)* at time $t_{[n]}$ of time section *[n]* [K]

$k_{[n]}^{cool-s(i)s[n]}$ = average thermal conductivity of the coolant in axial section *(i)* at time $t_{[n]}$ of

        time section *[n]* [W/cm-K]

$D_{e}^{heated-s(i)s[n]}$ = equivalent heated diameter of the coolant channel in axial section *(i)* for

        time section *[n]* [cm]

$Nu_{[n]}^{s(i)s[n]}$ = Nusselt number of the coolant in axial section *(i)* at time $t_{[n]}$ of time section

        [n] [dimensionless]

$Re_{[n]}^{s(i)s[n]}$ = Reynolds number of the coolant in axial section *(i)* at time $t_{[n]}$ of time section

        [n] [dimensionless]

$Pr_{[n]}^{s(i)s[n]}$ = Prandtl number of the coolant in axial section *(i)* at time $t_{[n]}$ of time section *[n]*

        [dimensionless]

$\mu_{[n]}^{cool-s(i)s[n]}$ = average dynamic viscosity of the coolant in axial section *(i)* at time $t_{[n]}$ of

        time section *[n]* [P]

$D_e^{hydraulic-s(i)s[n]}$ = equivalent hydraulic diameter of the coolant channel in axial section *(i)*

        for time section *[n]* [cm]

$E^c(\vec{r},t)$ = thermal energy of the cladding per unit volume at point $\vec{r}$ in three-dimensional

        space at time t [J/cm^3]

$\vec{e}_n$ = unit vector which is normal to the surface

$T_{\langle j+1 \rangle}^{c-s\langle j \rangle s(i)}$ = cladding temperature at radial node $r_{\langle j+1 \rangle}^{c-s(i)}$ in radial section *<j>* of axial section

        (i) [K]

$\Delta r^{c-s\langle j \rangle s(i)}$ = size of radial section *<j>* of the cladding in axial section *(i)* [cm]

$T_{\langle j-1 \rangle}^{c-s\langle j \rangle s(i)}$ = virtual variable at ghost node $r_{\langle j \rangle}^{c-s(i)} - \Delta r^{c-s\langle j \rangle s(i)}$ [K]

$\rho^{c-s\langle j \rangle s(i)s[n]}(r,t)$ = density of the cladding at radius r in radial section *<j>* of axial section

        (i) at time t of time section *[n]* [g/cm^3]

$c_p^{c-s\langle j\rangle s(i)s[n]}(r,t)$ = heat capacity of the cladding at radius r in radial section $\langle j\rangle$ of axial

section (i) at time t of time section $[n]$ [J/g-K]

$k^{c-s\langle j\rangle s(i)s[n]}(t)$ = average thermal conductivity of the cladding in radial section $\langle j\rangle$ of axial

section (i) at time t of time section $[n]$ [W/cm-K]

$V_{\langle j\rangle[n-1]}^{c-s\langle j\rangle s(i)s[n]}$ = diffusion number at radial node $r_{\langle j\rangle[n-1]}^{c-s(i)s[n]}$ in radial section $\langle j\rangle$ of axial section

(i) at time $t_{[n-1]}$ of time section $[n]$ [dimensionless]

$\alpha_{D\langle j\rangle[n-1]}^{c-s\langle j\rangle s(i)s[n]}$ = thermal diffusivity of the cladding at radial node $r_{\langle j\rangle[n-1]}^{c-s(i)s[n]}$ in radial section

$\langle j\rangle$ of axial section (i) at time $t_{[n-1]}$ of time section $[n]$ [cm^2/s]

$W_{[n-1]}^{c-s\langle j\rangle s(i)s[n]}$ = ratio of the conductive heat transfer coefficient of radial section $\langle j-1\rangle$ to

the conductive heat transfer coefficient of radial section $\langle j\rangle$ in axial

section (i) of the cladding at time $t_{[n-1]}$ of time section $[n]$

radial section $\langle g\rangle$ = the outermost radial section of the gap

$T_{\langle g\rangle[n-1]}^{g-s(i)s[n]}$ = gap temperature at radial sub-node $r_{\langle g\rangle[n-1]}^{g-s(i)s[n]}$ in axial section (i) at time $t_{[n-1]}$ of

time section $[n]$ [K]

$T_{in}^{g-s(i)}$ = gap inside temperature in axial section (i) [K]

$T_{out}^{g-s(i)}$ = gap outside temperature in axial section (i) [K]

$r_m^{g-s(i)}$ = logarithmic mean radius of the gap in axial section (i) [cm]

$h^{g-s(i)}$ = the intensive-property representation of the gap conductance in axial section (i)

[W/cm^2-K]

$E^f(\vec{r},t)$ = thermal energy of the fuel per unit volume at point $\vec{r}$ in three-dimensional space at time t [J/cm^3]

$S^f(\vec{r},t)$ = internal heat sources in the fuel slug region [W/cm^3]

$\vec{q}_{net}^{\prime\prime f}(\vec{r},t)$ = net current of heat at point $\vec{r}$ at time t [W/cm^2]

$q_{gen}^{\prime\prime\prime f}(\vec{r},t)$ = volumetric heat generation rate at point $\vec{r}$ in three-dimensional space at time t [W/cm^3]

$T_{\langle j+1/2\rangle}^{f-s\langle j\rangle s(i)}$ = fuel temperature at radial sub-node $r_{\langle j+1/2\rangle}^{f-s(i)}$ in radial section $<j>$ of axial section (i) [K]

$q_{gen}^{\prime\prime\prime f-s\langle j\rangle s(i)}$ = average volumetric heat generation rate in radial section $<j>$ of axial section (i) [W/cm^3]

$k^{f-s\langle j\rangle s(i)}$ = average thermal conductivity of the fuel in radial section $<j>$ of axial section (i) [W/cm-K]

$\Delta r^{f-s\langle j\rangle s(i)}$ = size of radial section $<j>$ of the fuel slug in axial section (i) [cm]

$T_{out}^{f-s(i)}$ = fuel outside temperature in axial section (i) [K]

$\rho^{f-s\langle j\rangle s(i)s[n]}(r,t)$ = density of the fuel at radius r in radial section $<j>$ of axial section (i) at time t of time section $[n]$ [g/cm^3]

$c_p^{f-s\langle j\rangle s(i)s[n]}(r,t)$ = heat capacity of the fuel at radius r in radial section $<j>$ of axial section (i) at time t of time section $[n]$ [J/g-K]

$V_{D\langle j\rangle[n-1]}^{f-s\langle j\rangle s(i)s[n]}$ = diffusion number at radial sub-node $r_{\langle j\rangle[n-1]}^{f-s(i)s[n]}$ in radial section *<j>* of axial

section *(i)* at time $t_{[n-1]}$ of time section *[n]* [dimensionless]

$\alpha_{D\langle j\rangle[n-1]}^{f-s\langle j\rangle s(i)s[n]}$ = thermal diffusivity at radial sub-node $r_{\langle j\rangle[n-1]}^{f-s(i)s[n]}$ in radial section *<j>* of axial

section *(i)* at time $t_{[n-1]}$ of time section *[n]* [cm^2/s]

$Q_{T\langle j\rangle[n-1]}^{f-s\langle j\rangle s(i)s[n]}$ = fuel temperature increase at radial sub-node $r_{\langle j\rangle[n-1]}^{f-s(i)s[n]}$ in radial section *<j>*

of axial section *(i)* for time section *[n]* by the internal heat source at time

$t_{[n-1]}$ of time section *[n]* [K]

$q_{T\langle j\rangle[n-1]}^{f-s\langle j\rangle s(i)s[n]}$ = fuel temperature increase rate at radial sub-node $r_{\langle j\rangle[n-1]}^{f-s(i)s[n]}$ in radial section

<j> of axial section *(i)* by the internal heat source at time $t_{[n-1]}$ of time

section *[n]* [K/s]

$W_{[n-1]}^{f-s\langle j\rangle s(i)s[n]}$ = ratio of the conductive heat transfer coefficient of radial section *<j-1>* to

the conductive heat transfer coefficient of radial section *<j>* in axial

section *(i)* of the fuel at time $t_{[n-1]}$ of time section *[n]*

$T_{\langle 1\rangle[n-1]}^{g-s(i)s[n]}$ = gap temperature at radial sub-node $r_{\langle 1\rangle[n-1]}^{g-s(i)s[n]}$ in axial section *(i)* at time $t_{[n-1]}$ of

time section *[n]* [K]

Section 2.2

ψ_k = permanent deformations due to swelling, creep, and plastic flow [dimensionless]

$(k = r, \theta,$ or $z)$

E = Young's modulus (modulus of elasticity) [MPa]

G = shear modulus (modulus of rigidity) [MPa]

ν = Poisson's ratio [dimensionless]

α = coefficient of linear thermal-expansion [K^{-1}]

ε^s = swelling strain [dimensionless]

ε_k^c = creep and plastic strain [dimensionless] ($k = r$, θ, or z)

$\nu^{s\langle j \rangle s(i)}$ = average Poisson's ratio in radial section $\langle j \rangle$ of axial section (i)

$\alpha^{s\langle j \rangle s(i)}$ = average linear thermal-expansion coefficient in radial section $\langle j \rangle$ of axial section (i) [K^{-1}]

$\varepsilon^{s-s\langle j \rangle s(i)}$ = swelling strain averaged over radial section $\langle j \rangle$ of axial section (i) [dimensionless]

$\varepsilon_r^{c-s\langle j \rangle s(i)}$ = creep and plastic strains in the radial direction averaged over radial section $\langle j \rangle$ of axial section (i) [dimensionless]

$\varepsilon_\theta^{c-s\langle j \rangle s(i)}$ = creep and plastic strains in the angular direction averaged over radial section $\langle j \rangle$ of axial section (i) [dimensionless]

$T^{s\langle j \rangle s(i)}$ = average temperature in radial section $\langle j \rangle$ of axial section (i) [K]

$C_1^{s\langle j \rangle s(i)}$ = constant of integration for radial section $\langle j \rangle$ of axial section (i) [dimensionless]

$C_2^{s\langle j \rangle s(i)}$ = constant of integration for radial section $\langle j \rangle$ of axial section (i) [cm^2]

$$a^{s\langle j \rangle s(i)} = \frac{E^{s\langle j \rangle s(i)}}{1+\nu^{s\langle j \rangle s(i)}} \text{ [MPa]}$$

$$b^{s\langle j\rangle s(i)} = \frac{v^{s\langle j\rangle s(i)}}{1-2v^{s\langle j\rangle s(i)}}$$

$$c^{s\langle j\rangle s(i)} = -3\left[\alpha^{s\langle j\rangle s(i)}\left(T^{s\langle j\rangle s(i)} - T_0^{s\langle j\rangle s(i)}\right) + \varepsilon^{s-s\langle j\rangle s(i)}\right]$$

$$d_k^{s\langle j\rangle s(i)} = -\left[\alpha^{s\langle j\rangle s(i)}\left(T^{s\langle j\rangle s(i)} - T_0^{s\langle j\rangle s(i)}\right) + \varepsilon^{s-s\langle j\rangle s(i)} + \varepsilon_k^{c-s\langle j\rangle s(i)}\right] \quad (k = r,\, \theta,\, \text{or } z)$$

$$X^{s\langle j\rangle s(i)}(r) = \frac{1}{2}\left(\frac{1+v^{s\langle j\rangle s(i)}}{1-v^{s\langle j\rangle s(i)}}\right)\left(\alpha^{s\langle j\rangle s(i)}T^{s\langle j\rangle s(i)} + \varepsilon^{s-s\langle j\rangle s(i)}\right)$$
$$+ \frac{1}{2}\left(\frac{1-2v^{s\langle j\rangle s(i)}}{1-v^{s\langle j\rangle s(i)}}\right)\left[\frac{1}{2}\left(\varepsilon_r^{c-s\langle j\rangle s(i)} + \varepsilon_\theta^{c-s\langle j\rangle s(i)}\right) + \left(\varepsilon_r^{c-s\langle j\rangle s(i)} - \varepsilon_\theta^{c-s\langle j\rangle s(i)}\right)(\ln r + 1)\right]$$

$$m^{s\langle j\rangle s(i)} = \frac{1}{2}\left(\frac{1-2v^{s\langle j\rangle s(i)}}{1-v^{s\langle j\rangle s(i)}}\right)\left(\varepsilon_r^{c-s\langle j\rangle s(i)} - \varepsilon_\theta^{c-s\langle j\rangle s(i)}\right)$$

$u_{z(i)}^{s(i)}$ = axial displacement of axial node $z_{(i)}$ in axial section *(i)* [cm]

radial section *<f>* = the outermost radial section of the fuel

$\left. u_r^{f-s\langle 1\rangle s(i)}(r)\right|_{r=r_{\langle 1\rangle}^{f-s(i)}}$ = radial displacement of the first radial node $r_{\langle 1\rangle}^{f-s(i)}$ in axial section *(i)*

of the fuel [cm]

$\left. \sigma_r^{f-s\langle f\rangle s(i)}(r)\right|_{r=r_{\langle f+1\rangle}^{f-s(i)}}$ = radial stress at the last radial node $r_{\langle f+1\rangle}^{f-s(i)}$ in axial section *(i)* of the

fuel [MPa]

P_{plenum} = plenum pressure in the fuel pin of interest [MPa]

$\left. u_r^{f-s\langle j-1\rangle s(i)}(r)\right|_{r=r_{\langle j\rangle}^{f-s(i)}}$ = radial displacement of radial node $r_{\langle j\rangle}^{f-s(i)}$ of radial section *<j-1>* in

axial section *(i)* of the fuel [cm]

$\sigma_r^{f-s\langle j\rangle s(i)}\left(r\right)\Big|_{r=r_{\langle j+1\rangle}^{f-s(i)}}$ = radial stress at radial node $r_{\langle j+1\rangle}^{f-s(i)}$ of radial section $<j>$ in axial

section *(i)* of the fuel [MPa]

P_{cool} = coolant pressure acting on the outside of the cladding [MPa]

$\sigma_z^{f-s(i)}\left(r\right)$ = axial stress at radial node r in axial section *(i)* of the fuel [MPa]

$W_t^{f-s(i+1)}$ = weight of axial section *(i+1)* of the fuel [MPa·cm^2] or [10^2·N]

N = number of axial sections

$P_{contact}^{s(i)}$ = contact pressure at axial section *(i)* [MPa]

$F_f^{s(i)}$ = friction force acting vertically on the outer surface of the fuel at axial section *(i)*

[MPa·cm^2] or [10^2·N]

$u_r^{f-s\langle f\rangle s(i)}\left(r\right)\Big|_{r=r_{\langle f+1\rangle}^{f-s(i)}}$ = radial displacement of the last radial node $r_{\langle f+1\rangle}^{f-s(i)}$ in axial section *(i)*

of the fuel [cm]

$\left[u_r^{c-s\langle 1\rangle s(i)}\left(r\right)\Big|_{r=r_{\langle 1\rangle}^{c-s(i)}}\right]_{contact}$ = radial displacement of the first radial node $r_{\langle 1\rangle}^{c-s(i)}$ in axial

section *(i)* of the cladding until gap closure [cm]

$\left[u_z^{f-s(i)}\left(z\right)\Big|_{z=z_{(i+1)}^f}\right]_{contact}$ = axial displacement of axial node $z_{(i+1)}^f$ in axial section *(i)* of the

fuel until gap closure [cm]

μ_{static} = coefficient of static friction

$\mu_{sliding}$ = coefficient of sliding friction

$$X_{\langle j+1\rangle}^{f-s\langle j\rangle s(i)} = \frac{1}{2}\left(\frac{1+\nu^{f-s\langle j\rangle s(i)}}{1-\nu^{f-s\langle j\rangle s(i)}}\right)\left(\alpha^{f-s\langle j\rangle s(i)}T^{f-s\langle j\rangle s(i)} + \varepsilon^{s-f-s\langle j\rangle s(i)}\right)$$

$$+\frac{1}{2}\left(\frac{1-2\nu^{f-s\langle j\rangle s(i)}}{1-\nu^{f-s\langle j\rangle s(i)}}\right)\left[\frac{1}{2}\left(\varepsilon_r^{c-f-s\langle j\rangle s(i)} + \varepsilon_\theta^{c-f-s\langle j\rangle s(i)}\right)\right.$$

$$\left.+\left(\varepsilon_r^{c-f-s\langle j\rangle s(i)} - \varepsilon_\theta^{c-f-s\langle j\rangle s(i)}\right)\left(\ln r_{\langle j+1\rangle}^{f-s(i)} + 1\right)\right]$$

$$W_{\langle j\rangle}^{f-s\langle j-1\rangle s(i)} = \left(\frac{1+\nu^{f-s\langle j-1\rangle s(i)}}{1-\nu^{f-s\langle j-1\rangle s(i)}}\right)\left(\alpha^{f-s\langle j-1\rangle s(i)}T^{f-s\langle j-1\rangle s(i)} + \varepsilon^{s-f-s\langle j-1\rangle s(i)}\right)\frac{r_{\langle j\rangle}^{f-s(i)}}{2}$$

$$+\frac{1}{2}\left(\frac{1-2\nu^{f-s\langle j-1\rangle s(i)}}{1-\nu^{f-s\langle j-1\rangle s(i)}}\right)\left[\left(\varepsilon_r^{c-f-s\langle j-1\rangle s(i)} + \varepsilon_\theta^{c-f-s\langle j-1\rangle s(i)}\right)\frac{r_{\langle j\rangle}^{f-s(i)}}{2}\right.$$

$$\left.+\left(\varepsilon_r^{c-f-s\langle j-1\rangle s(i)} - \varepsilon_\theta^{c-f-s\langle j-1\rangle s(i)}\right)\left(r_{\langle j\rangle}^{f-s(i)}\ln r_{\langle j\rangle}^{f-s(i)}\right)\right]$$

$$F_{\delta r}^{f-s\langle j\rangle s(i)} = a^{f-s\langle j\rangle s(i)}b^{f-s\langle j\rangle s(i)}\left[\left(r_{\langle j+1\rangle}^{f-s(i)}\right)^2 - \left(r_{\langle j\rangle}^{f-s(i)}\right)^2\right]$$

$$G_{\delta r}^{f-s\langle j\rangle s(i)} = a^{f-s\langle j\rangle s(i)}\left(1+b^{f-s\langle j\rangle s(i)}\right)\left[\frac{\left(r_{\langle j+1\rangle}^{f-s(i)}\right)^2 - \left(r_{\langle j\rangle}^{f-s(i)}\right)^2}{2}\right]$$

$$H_{\delta r}^{f-s\langle j\rangle s(i)} = a^{f-s\langle j\rangle s(i)}\left(b^{f-s\langle j\rangle s(i)}c^{f-s\langle j\rangle s(i)} + d_z^{f-s\langle j\rangle s(i)}\right)\left[\frac{\left(r_{\langle j+1\rangle}^{f-s(i)}\right)^2 - \left(r_{\langle j\rangle}^{f-s(i)}\right)^2}{2}\right]$$

Section 3.1

F_{f-open} = friction force induced by the deformation of the axial sections having the open

gap [MPa·cm^2] or [10^2·N]

ρ_A = as-cast fuel density [g/cm^3]

SD = smeared density [%TD]

r_f = radius of the as-fabricated fuel [cm]

r_g = radius up to the inner surface of the as-fabricated cladding [cm]

ρ_T = theoretical density of the fuel at room temperature [g/cm^3]

p_0 = porosity of the as-fabricated fuel [%]

Section 3.2

$H^{s(i)}$ = length of axial section *(i)* [cm]

M_0 = initial mole of gas in the fuel pin [mol]

M_{FGR} = mole of the fission gas released to the gap and plenum [mol]

R = gas constant [J/mol-K]

V_0^{plenum} = initial volume of the plenum region [cm^3]

T_0^{plenum} = initial average temperature of the plenum region [K]

$V^{p-s(i)}$ = volume of the pores in axial section *(i)* [cm^3]

$T^{p-s(i)}$ = average temperature of the pores in axial section *(i)* [K]

TABLE OF CONTENTS

LIST OF FIGURES

xxi

LIST OF TABLES

1. INTRODUCTION

Interest in the sodium fast reactor (SFR) systems whose primary missions are improved utilization of uranium resources and efficient management of high-level wastes [1] has been renewed and invigorated for the past ten years [2]. With innovations for economical electricity production, the SFR development is now aiming at establishment of the advanced nuclear energy system selected by the Generation IV International Forum (GIF) [1]. The GIF system has the following four criteria: safety and reliability, economic competitiveness, sustainability, and proliferation resistance and high physical protection [3].

The sodium-cooled fast reactor features a fast neutron spectrum and liquid-metal cooling. Abundant high-energy neutrons in the SFR core provide ability to burn long-lived radiotoxic nuclides, plutonium and other actinides in particular, included in the spent nuclear fuel (SNF) of the in-service commercial reactors such as the light water reactor (LWR) [4]. This TRU-burning ability of the SFR can be used to reduce the volume and toxicity of high-level wastes. With pyro-electro-chemical processing technology [5], the SFR system can have a fully closed fuel cycle and achieve ultimate utilization of uranium resources owing to its excellent transmutation efficiency. The fast neutron spectrum also minimizes the reactivity and power oscillation attributed to the variation of xenon and samarium concentrations because the neutron cross sections of xenon and samarium are relatively low in the high-energy region [4].
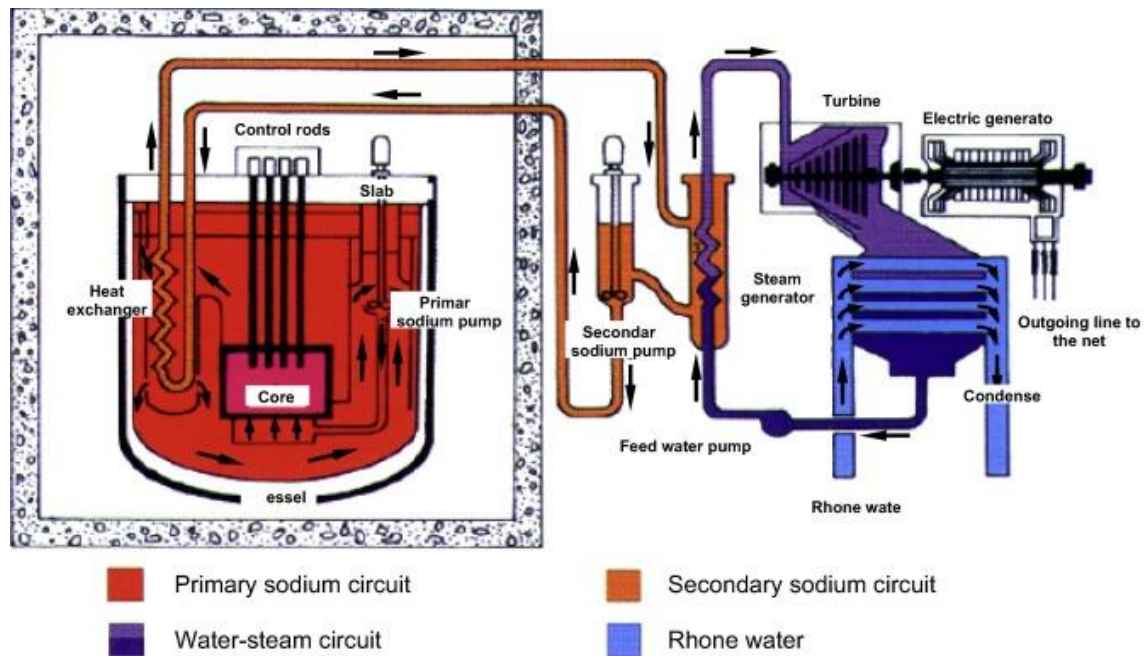
Figure 1.1. Plant layout of the PHENIX reactor as a typical representative of the pool design of fast reactors. Reprinted from reference [2].

The liquid-sodium coolant basically allows high power density with a low coolant volume fraction [1]. The liquid sodium is chemically compatible with the steel materials [4] and provides an oxygen-free environment which prevents corrosion of the core components [1]. This characteristic permits the pool-type reactor configuration illustrated in Figure 1.1 [2] as a possible option of the SFR design. The liquid sodium also has a high boiling point of 883 ℃ at atmospheric pressure [4], which gives an ample boiling margin from the normal coolant-operating temperatures (typically 350 ℃ inlet and 510 ℃ outlet) [6]. The atmospheric pressure eliminates the possibility of high-pressure release accidents [4]. Moreover, an atmospheric-pressure primary system does not need the thick pressure vessels necessary to contain the high pressures, and it, in turn, enables the pool-type

reactor configuration [7] together with the chemical compatibility of the liquid-sodium coolant. The large sodium inventory of the pool configuration generally provides a large thermal inertia [7] which makes thermal transients mild and allows a relatively longer grace period in an accident condition [4].

Table 1.1. Physical properties of fuel candidates (Pu / (U+Pu) = 20%). Reprinted from reference [3].

Property	$(U, Pu)O_2$	$(U, Pu)Zr$	$(U, Pu)N$	$(U, Pu)C$
Density $[g/cm^3]$	11.0	15.6	14.3	13.6
HM Density $[g/cm^3]$	9.7	14.0	13.5	12.9
Melting Point $[°C]$	2730	1070	2720 (atm. N_2)	2320
Thermal Conductivity $[W/m-K]$	2.9 (1000 °C)	35 (500 °C)	19.8 (1000 °C)	19.6 (1000 °C)
Thermal Expansion $[10^{-6}/°C]$ (20~1000 °C)	12.6	16.5	10.0	12.4

1.1. Motivations

The advantages of the SFR system are boosted by using metallic fuels which have high burnup capability and reliable steady-state and off-normal performance characteristics [8] originating from their intrinsic thermal, mechanical, chemical and neutronics properties. The metal fuels have higher fissile and fertile densities than oxide or carbide fuels, as shown in Table 1.1 [3]. The higher heavy-metal densities allow higher breeding ratios (Figure 1.2 [6]) and smaller core sizes for a specific reactor power [9]. The superior

neutron economy further enables improvements in the reactor core design such as minimizing the reactivity swing over an operating cycle and increasing the cycle length [6]. Also, the metal fuel is chemically compatible with the liquid-sodium coolant, and it eliminates the potential of energetic fuel-coolant reactions and flow blockages in the case of cladding breach [10]. Thus, the metallic fuel exhibits benign run beyond cladding breach (RBCB) behaviors as shown in Figure 1.3 [8].
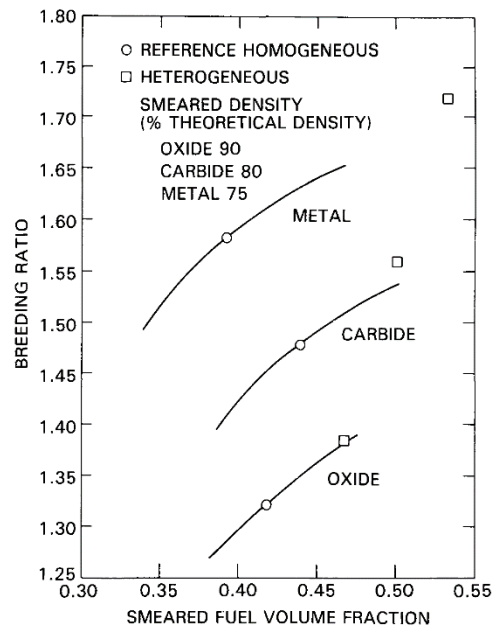
Figure 1.2. Comparison of breeding ratio potentials of oxide, carbide, and metal fuels. Reprinted from reference [6].

Another safety-related benefit of the metal fuel is its high thermal conductivity and consequent low fuel-operating-temperatures that afford a sufficient power-to-melt margin [4]. In the anticipated transient without scram (ATWS) events such as loss of flow without

4

scram (LOFWS), loss of heat sink without scram (LOHSWS), and transient overpower without scram (TOPWS) [6], the fuel and core expand with increased core temperatures [4], and the thermal expansion favorably induces a negative reactivity feedback and a power rundown. After the power rundown, the metallic fuel can retain this inherent passive safety characteristic with a negligible retraction of the negative reactivity as a result of smaller variations in the Doppler reactivity feedback attributed to the significantly lower operating-temperatures. Therefore, the metallic fuels show reliable thermal transient behaviors, and could deterministically survive in the accident scenarios without human interventions or operations of engineered components [6]. As an additional intrinsic safety feature of the metal fuel, the large amount of axial and radial expansion driven by fission gases provides negative reactivity feedback before the fuel pin itself fails [6].

(a)   (b)
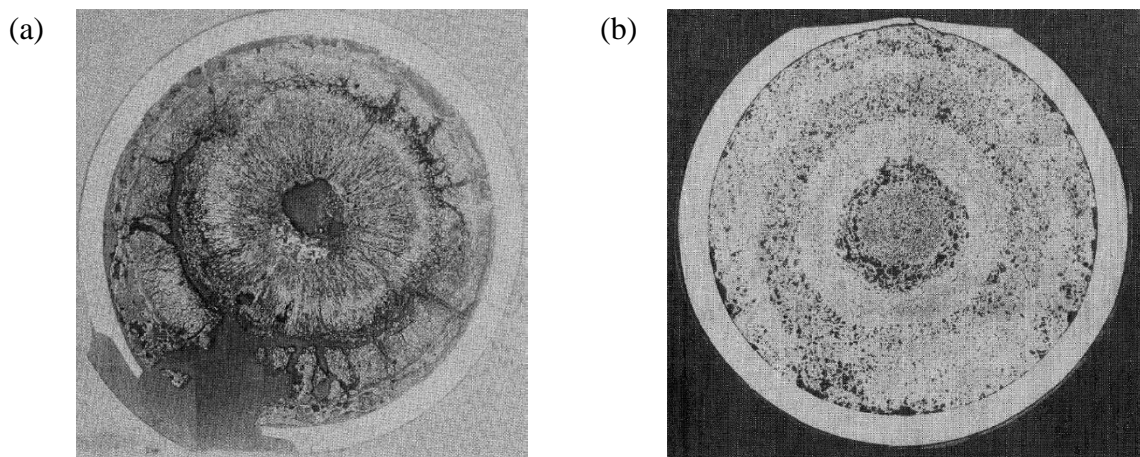
Figure 1.3. Cross-sections of the oxide fuel and the metal fuel after RBCB tests. (a) During the oxide fuel RBCB test (9% burnup), the initial breach site is widened by the low density sodium-fuel-interaction-product, $Na_3(PuU)O_4$, which results in a small amount of fuel loss to the coolant. (b) There are no reaction products and no indications of breach site enlargement in the metal fuel RBCB test (12% burnup). Also, the fuel loss is practically zero in the metal fuel experiment. Reprinted from reference [8].

Furthermore, the metallic fuel is easily fabricated by simple injection-casting. Extensive experience on the metallurgical processes of the injection-casting [11] is available, and the fuel slug can be manufactured without crystallographic texture which induces unusual irradiation growth and swelling [9]. The relatively short fabrication sequence of the injection-casting with easy-to-build and easy-to-use equipment [3] brings more economic competitiveness to the metal fuel. In addition to the ease of fabrication, the metal fuel can be supported by straightforward recycling technology that fundamentally precludes undetected diversion of the fuel material and its use for nuclear weapons through difficulties of handling the reprocessed product containing uranium and highly radioactive fission products along with plutonium [12]. This recycling method basically allows all the actinides to remain in the fuel cycle and to be fabricated back into the recycled fuel and fissioned for useful energy [12]. Also, its process involves batch operations, and thus is easily scaled to meet local requirements [12].

The beneficial intrinsic properties and reliable high-burnup performance of the metallic fuels are closely related to an alloying element which is added to the uranium or uranium-plutonium metal. The additive is primarily intended for enhancing dimensional stability under irradiation, but also for improving corrosion resistance and tailoring solidus and liquidus temperatures toward desired values for fabrication and operational performance [9]. Several elements were explored as candidates for the alloying agent, and chromium, molybdenum, titanium, and zirconium exhibited an adequate increase in melting temperature [12] for both of the uranium and plutonium bearing fuels. However, zirconium was exceptional among them in that it enhanced compatibility between the fuel

6

and cladding materials by suppressing the inter-diffusion of fuel and cladding components [12]. The inter-diffusion of fuel and cladding components and their chemical reaction generally deteriorate the cladding mechanical properties and lead to the formation of compounds having relatively low melting points in both fuel and cladding [13]. During an off-normal event, the lower-melting-temperature compositions can result in eutectic liquefaction, which effectively reduces the thickness of the load-bearing cladding wall. This fuel-cladding chemical interaction (FCCI) is initiated from high fuel swelling and enhanced by rare-earth fission products (lanthanides) present in increasing amounts with higher burnup [9].
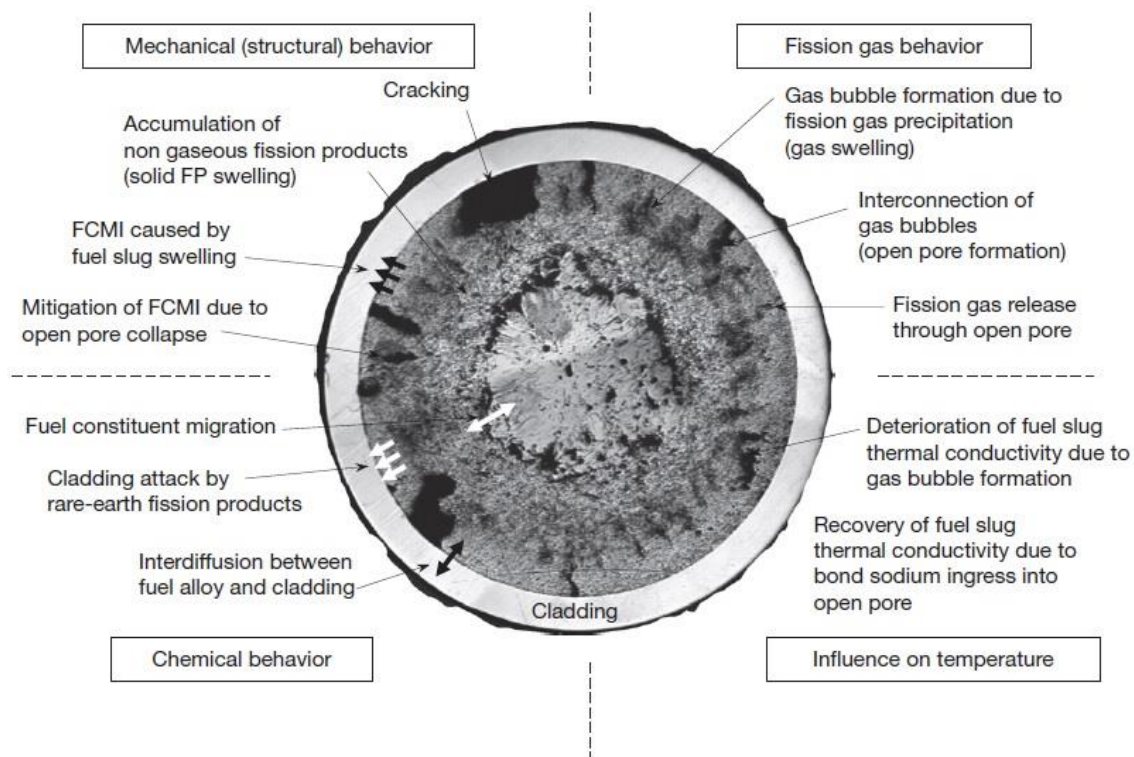
Figure 1.4. Major Irradiation behaviors of metal fuel. Reprinted from reference [14].
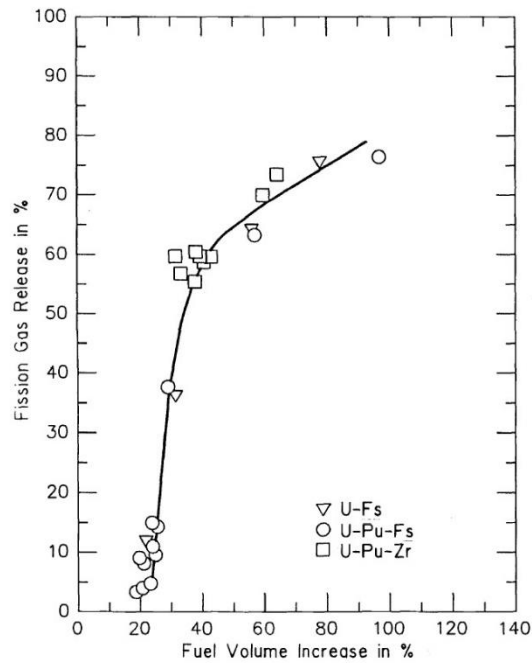
Figure 1.5. Fission gas release versus fuel volume increase. The bubble interlinkage and open-channel formation appear to be rather independent of fuel alloy. Reprinted from reference [12].

Although the U-Zr and U-Pu-Zr fuels were shown to have sufficient reliability to high burnups by earlier irradiation tests, further evaluations of key fuel-performance phenomena outlined in Figure 1.4 [14] are still of interest for determining fuel operational limits [9] and for demonstrating the enhanced safety characteristics of the zirconium alloy fuels. Fission gas release (FGR) and fission-gas-induced swelling had been considered as the most serious obstacle to achieving high burnup in early stages of the metallic fuel development. These issues were addressed with two simple design changes: ① a reduced planar smeared density for accommodating fuel swelling to the point where fission gas bubbles are interconnected to develop open channels for fission gas to be continuously

8

released into the pin plenum (thus minimizing the driving force for further swelling) and

② a larger fuel pin plenum for capturing the released fission gas with less stress placed on

the cladding [9]. Figure 1.5 shows that FGR is rapidly increased at about 30% fuel swelling

which is allowed by the low smeared density for the bubble interconnection and open-

channel formation [12].
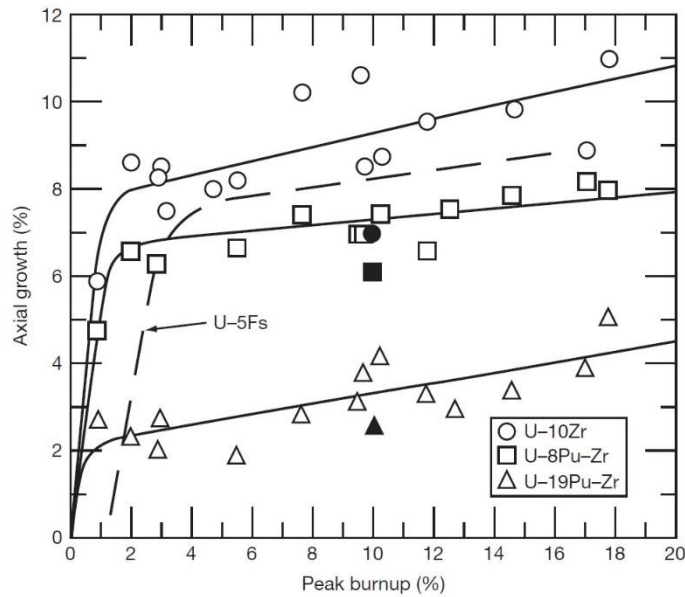
Figure 1.6. Fuel length increase in various metallic fuels as a function of burnup. The open symbols represent EBR-II irradiation data, and the closed symbols indicate IFR-1 irradiation data. Reprinted from reference [13].

Another critical irradiation behavior to be considered for the zirconium alloy fuels

is fuel constituent redistribution, which is radial inter-diffusion of U, Pu, and Zr within the

fuel. It occurs in the early stage of irradiation and creates Zr-depleted radial zones

consequently having lower and local solidus temperatures. The constituent redistribution

9

and zone formation are due to phase equilibria effects established in the temperature gradient across the radius of the fuel [9], and hence they are temperature dependent and have radial patterns. The formation of radial zones accelerates the radial swelling markedly. The high rate of radial swelling induces stresses in the peripheral region of the fuel, which is large enough to result in crack formations [8]. This anisotropic swelling also leads to much smaller axial growth. The radial zone formation and anisotropic swelling are more pronounced in the plutonium ternary fuel than in the U-Zr fuels or U-fissium fuels [8], as shown in Figure 1.6 [13].
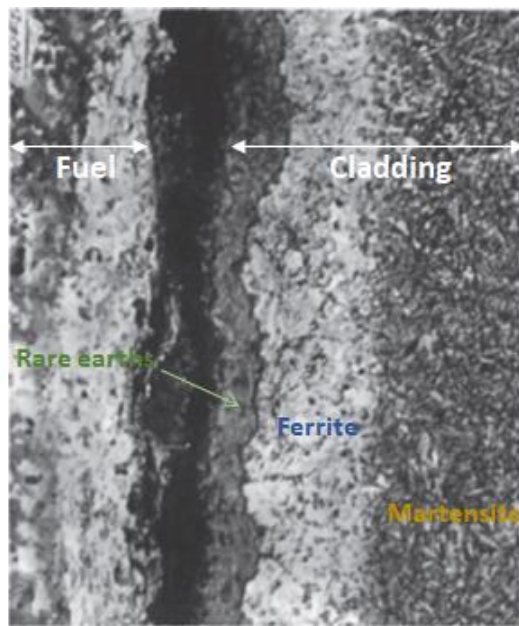
Figure 1.7. Inter-diffusion between U-10Zr fuel and HT9 cladding irradiated to 6 at.% burnup at ~ 620 °C. Reprinted from reference [13].

Although the addition of zirconium as an alloying element greatly improves the chemical compatibility between the fuel and cladding materials, FCCI is still one of the

life-threatening fuel-performance phenomena under high burnup and long reactor-residence time. The FCCI in metallic fuels is characterized by two stages of interaction which have different cladding wastage mechanisms [13]. The first stage occurs prior to the accumulation of rare-earth fission products (lanthanides) at the fuel-cladding interface [13]. In this stage, the cladding components, nickel/carbon and iron in particular, diffuse into the fuel [12], and then develop lower-melting-temperature compositions near the interface. The Ni-depletion in the austenitic cladding and the decarburization of the martensitic cladding also cause the formation of a ferretic layer in the cladding region, as shown in Figure 1.7 [13]. During the second stage, the lanthanide fission products (FPs) eventually control the overall FCCI phenomena as more lanthanides migrate to the fuel-cladding interface in higher burnup. The radial migration of the lanthanide FPs and the lanthanides-controlled FCCI increase with both fuel temperature and presence of Pu in the fuel [13]. The FCCI could be reduced by using a protective barrier (zirconium, vanadium, or zirconium-nitride) on the cladding inner surface or by using alloy agents that can slow down or impede the diffusion of critical FPs [13].

1.2. Background

As mentioned in section 1.1, accurate evaluations of fuel performance is a crucial part in the determination of limiting conditions of operation (LCOs) [9] and in the verification of burnup capabilities and reliability characteristics. The fuel performance analysis generally requires a comprehensive computational tool which can predict and quantify in-pile fuel

behaviors that are elaborately linked to one another under diverse irradiation histories. The tool is also required as a practical guide for fuel modeling, irradiation experiments, and development of advanced fuel materials and designs.

Table 1.2. Metallic fuel performance codes. Reprinted from reference [15].

	LIFE-METAL	SESAME	ALFUS	MACSIS	FEAST-METAL
Developer	ANL (US)	CRIEPI (JAPAN)	CRIEPI (JAPAN)	KAERI (Korea)	MIT (US)
General capabilities	Steady-state and transient behavior	Steady-state behavior	Steady-state behavior	Steady-state behavior	Steady-state and transient behavior
Fission gas release and fuel swelling	Empirical correlation	Empirical correlation	Mechanistic model, based on UO_2 Fuel	Mechanistic model, based on UO_2 Fuel	Mechanistic model, based on metal fuel
Constituent redistribution	Empirical correlation	Chemical equilibrium model	Thermo-transport theory	Thermo-transport theory	Thermo-transport theory
Temperature distribution	1D model	1D model	1D model	1D model	1D model
Mechanical analysis	1D model	1D model	2D model	1D model	1D model
FCCI	Empirical correlation	Not included	Empirical correlation	Not included	Diffusion model based on precipitation kinetics
Creep fracture	Cumulative damage fraction model	N/A	N/A	N/A	(1) Cumulative damage fraction model (2) Constrained diffusional cavity growth model

Several fuel performance codes have been developed as the comprehensive computational tool to simulate irradiation behaviors of metallic fuels. Table 1.2 summarizes representative metal fuel performance codes [15–19]. The first metal fuel code is LIFE-METAL which evolved from the LIFE series. The original version of the LIFE code had been built for oxide fuels, and the later versions, including LIFE-METAL, retained the same code structure with employing different materials properties and

12

behavior models according to the fuel type [13]. LIFE-METAL is a combined code for steady-state and transient fuel performance evaluations. It predicts thermo-mechanical behaviors of a metallic fuel pin in the sodium-cooled fast reactor as a function of reactor operating history. The code calculations are executed in the radial direction of the fuel pin where up to 20 radial rings are allowed to account for radial variations in the fuel behaviors (thermal analysis and mechanical analysis use different radial rings) [13]. Axial variations are represented through assigning the local power and fast flux at up to 9 axial nodes [13]. The axial nodes are thermally combined by coolant temperature calculations, but are not mechanically affected by the conditions or behaviors of any other axial nodes, which means axial lock-up effects on mechanical performance are not taken into account. LIFE-METAL adopted empirical correlations for critical fuel performance phenomena such as fission gas release, fission-gas-induced swelling, and fuel constituent redistribution.

SESAME (Simulating Evaluation System of Alloyed Metallic Element) [17] was developed next to LIFE-METAL by the Central Research Institute of the Electric Power Industry (CRIEPI) in Japan. The code predicts the steady-state irradiation behavior of both U-Fs and U-Pu-Zr alloy fuels. A single fuel element is divided into several axial nodes, each containing several equiaxial radial meshes in which performance variables such as stress, strain, temperature, and material properties are assumed to be uniform. Temperature calculations are done by a conventional one degree of freedom finite element method (FEM) in a temperature convergence loop for handling the nonlinearity of thermal conductance. The constituent redistribution model, fission gas release model, and fuel swelling model are also included in the temperature convergence loop due to the mutual

dependence of those models and temperature calculations. The convergence of the temperature calculations is achieved more easily than the gap conductance problem of oxide fuel performance codes, and hence the code uses relatively longer time-steps except the shortened time-step right before the gap closure. Like the LIFE-METAL code, SESAME employed many empirical correlations that could be invalid when applied to the outside of the database range for which they were formulated originally.

The later codes MACSIS (Metal fuel performance Analysis Code for Simulating the In-reactor behavior under Steady-state conditions) and ALFUS (ALloyed Fuel Unified Simulator) contain more theoretical models based on the fundamental physics of fuel performance phenomena. MACSIS [19,20] was developed by Korea Atomic Energy Research Institute (KAERI) as a fuel design tool for the Korea advanced liquid metal reactor (KALIMER) program. Major models of MACSIS are included in the calculation scheme of temperature profiles that consider the effects of sodium infiltration, fuel constituent redistribution, fission gas release, and fuel pin deformation. The scheme is structured with a convergence loop where the gap conductance is iteratively calculated until convergence by the Ross-Stoute model which takes account of conduction through the sodium bond, radiant heat transfer, and solid-solid conduction through points of contact. The fuel constituent redistribution model was derived from the thermo-transport theory. The code computes fission gas release and fuel swelling by evaluating the intra-granular diffusion of fission gas atoms (first suggested in Booth's classical diffusion theory) and the inter-granular movements of fission gas bubbles. However, those mechanisms were originally introduced for ceramic fuels and may not be valid in metallic

fuels. The fuel slug is divided into up to 20 axial nodes, and each axial node is radially divided into ten concentric annuli of equal thickness. The detailed thermo-mechanical analyses are performed in the radial direction at each axial node as one-dimensional calculations. The axial nodes are thermally coupled through coolant temperature calculations, but the mechanical coupling between axial nodes is not considered in the code. MACSIS can simulate only steady-state fuel behaviors like the SESAME code.

ALFUS [14,18,21–23] was developed by CRIEPI for a comprehensive understanding of the mechanical behaviors of metal fuels during irradiation. It consists of four major calculation parts: temperature distribution, fuel constituent migration, fission gas swelling and release, and stress-strain of the fuel slug and cladding. The stress-stain analysis is based on a 2D (r-direction and z-direction) finite element method which was used in the LWR fuel performance code FEMAXI-III. The mechanical analysis model assumes axial symmetry and takes account of gas bubble compressibility and open pore volume decrease. ALFUS adopted a mechanistic model to simulate fission gas release and fuel swelling phenomena. The model includes detailed descriptions about intra-granular diffusion, bubble growth and coalescence, and open pore formation, but it was originally developed for UO_2 fuel. Temperature calculations use effective thermal conductivity of the porous slug infiltrated by the bond sodium. Fuel constituent migration is computed by a thermo-diffusion model. The code employed several empirical correlations to estimate solid fission product swelling, cladding wastage by rare-earth FPs, and anisotropic slug deformation due to cracks. Simulations can be applied only to the fuel pin under steady-state conditions, and the usual time-step interval of the steady-state simulations is 20

15

hours. This preset time interval is divided into smaller intervals automatically in accordance with the rate of gap closure and the creep rate of the hottest part of the fuel slug.

FEAST (Fuel Engineering And Structural analysis Tool) was developed by the Massachusetts Institute of Technology (MIT) to predict the irradiation behaviors of U-Zr and U-Pu-Zr metal fuel pins and UO_2-PuO_2 mixed oxide fuel pins in sodium-cooled fast reactors. FEAST-METAL [15,24] is the metal fuel version of the FEAST code. FEAST-METAL can simulate the thermo-mechanical behaviors under both steady-state and design-based (non-disruptive) transient scenarios. The fuel pin is divided into up to 20 axial nodes, and each axial node of the fuel slug and cladding is further divided into up to 8 radial nodes. The code emphasized the importance of mechanistic models and attempted to adopt non-empirical models to the extent possible. Fission gas release and fuel swelling are calculated by the Gas Release and Swelling in ISotropic fuel matrix (GRSIS) model [25], which is based on detailed tracking of fission gas bubbles within the metal fuel. The fuel constituent redistribution model was derived from the thermo-transport theory. Fuel-cladding chemical interaction was modeled with precipitation kinetics, and the transient creep-fracture of the cladding was modeled by using the diffusion-controlled cavity-growth model. Temperature calculations assume no axial heat conduction. A thermal conductivity model that considers the effects of porosity and sodium-bond infiltration is used to calculate fuel temperature distributions. The thermal analysis models contain unrealistic assumptions such as constant heat flow within each radial node, and the transient thermal models employ some numerical methods which are inferior in stability

16

and accuracy. For mechanical analysis, FEAST-METAL adopted the mechanical models of LIFE-METAL. The mechanical models do not have any logical algorithm for updating dimensional information and mesh data with time-dependent net strains and displacements calculated iteratively in the time loop of the code; similarly, there is no specific algorithm for calculating new accumulated strains and displacements by using updated dimensions and mesh. The compressibility of open pores and the anisotropic deformation of the fuel are estimated by the empirical models used in ALFUS. In the FEAST-METAL code, thermal performance phenomena and mechanical performance phenomena are not evaluated simultaneously; instead, temperature-related behaviors are explicitly calculated by using the data generated in the mechanical analysis of the previous time-step. This decoupled algorithm has a tendency to become somewhat unstable and produce oscillating solutions under certain conditions. The code also utilizes ineffective matrix-solvers which generally entail an increased numerical error and are not efficient in terms of speed and computation load.

1.3. Objectives

As explained above, several codes were developed as the comprehensive computational tool for the evaluation of metallic fuel performance. However, those codes have various limitations on their ability to predict irradiation behaviors. The limitations are mainly caused by unrealistic assumptions such as radial and/or axial independency in fuel performance calculations, drastic simplifications for explicit code algorithms, decoupled

solution schemes of fuel perform models, adoption of empirical models, and employment of inferior numerical methods (in terms of stability and accuracy). To overcome the limitations of the existing codes, a study having the following objectives was conducted herein:

① Erect a robust framework for a comprehensive computational tool by implementing improved thermo-mechanical models in the tool. The computational tool was named Tool for Analyzing Metallic U-Zr Fuel Performance (TAMU-ZFP).

② Derive new improved thermal analysis models and mechanical analysis models that effectively describe the spatial variation and time dependence of thermo-mechanical behaviors.

③ Develop fully implicit solution schemes for handling the nonlinearity and information propagation involved in fuel performance models.

④ Establish advanced code algorithms which process the radial and axial interlocking in a fuel performance calculation, coupling of fuel perform models, contact analysis, and dynamic dimensioning and power adjustment after fuel pin deformation.

⑤ Construct transient code modules for the simulations of design-based off-normal fuel behaviors with installing efficient numerical methods for transient modeling.

⑥ Implant physics-based fuel performance models and up-to-date materials properties into the TAMU-ZFP code.

⑦ Build a 3D graphical tool for the visualization of the code output. Also, the graphical tool should include a module which provides basic post-processing.

In addition, the TAMU-ZFP code was aimed at having enhanced applicability and flexibility. The binary U-Zr alloys were considered as the primary fuel type in this research because of their superior performance characteristics. However, the irradiation behaviors of the ternary U-Pu-Zr alloy fuels can be simulated identically in TAMU-ZFP without any further restriction. The code is also applicable to various fuel pin designs (e.g., fuel pin designs having axial blanket regions, new cladding materials, etc.).

In this dissertation, the following contents will be covered:

- SECTION 2: modeling work for the evaluations of thermo-mechanical performance of metallic fuels.

- SECTION 3: descriptions about the structure of the TAMU-ZFP code and calculation schemes.

- SECTION 4: assessment of the TAMU-ZFP code with experimental data available in the open literature.

2. MODELS FOR EVALUATIONS OF METAL FUEL PERFORMANCE

This section describes the fuel performance models which evaluate the irradiation behaviors of metallic fuels in sodium fast reactors. The phenomena considered in the models include heat conduction through the fuel and cladding, elastic and plastic deformation, fuel-cladding mechanical interaction, fission gas release and fuel swelling, pin internal gas pressure, heat transfer from cladding to coolant, and fuel restructuring.

The models involve various numerical methods that need an adaptable mesh system and dynamic dimensioning. The adaptable mesh system means that the size and number of meshes are variable and non-uniform in order to accommodate the spatial and temporal dependence of the fuel pin deformation. Figure 2.1 shows an example of the subdivision of a fuel pin into radial and axial sections. Axial section *(i)* is located between axial node $z_{(i)}$ and $z_{(i+1)}$, and radial section $<j>$ is located between radial node $r_{<j>}$ and $r_{<j+1>}$. $E_{<j>(i)}$ depicted in Figure 2.1 indicates the element enclosed with radial node $r_{<j>}$ and $r_{<j+1>}$ within axial section *(i)*. The round brackets are used for the axial space indexes and the axial mesh point numbers, while the angle brackets are used for the radial space indexes and the radial mesh point numbers. For transient modeling, the square brackets are additionally introduced to represent time space indexes and time node numbers.

Each of the fuel performance models is implanted into the TAMU-ZFP code as an individual module, and the modules communicate with each other in iterative convergence loops to calculate the interrelated effects of the fuel behaviors. Details about the calculation procedure and loop structure in the code are represented in SECTION 3.
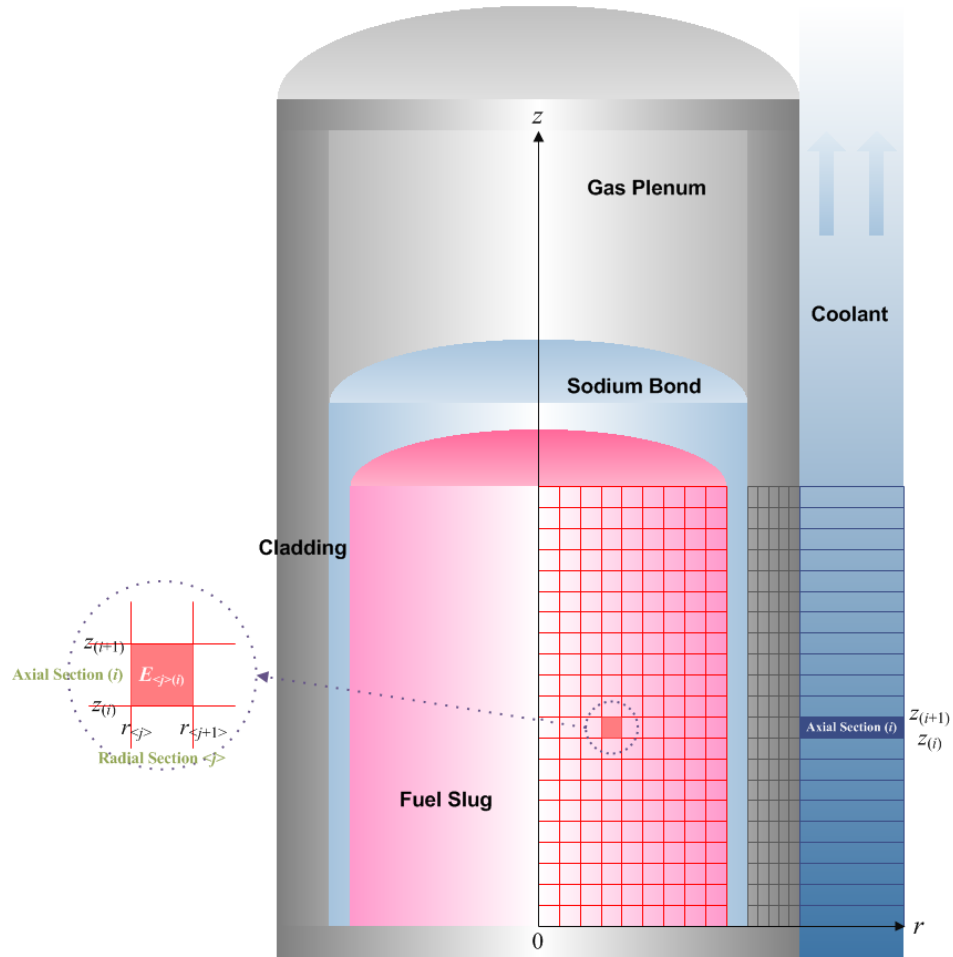
Figure 2.1. Subdivision of a fuel pin into radial and axial sections.

2.1. Thermal Response Models

Thermal response models calculate temperature distributions in a fuel pin and coolant temperatures in a coolant channel. Advanced numerical methods are used in the models for enhanced spatial and temporal definition of the internal heat source, heat conduction, and materials properties. The computed temperature distributions feed the calculations of mechanical response, fission gas release, and so forth.

21

2.1.1. Coolant Temperature

The coolant temperature associated with the fuel pin of interest is calculated by a single channel coolant enthalpy rise model [26]:

$$\rho^{cool}(z,t) A_c^{channel}(z,t) c_p^{cool}(z,t) \frac{\partial T^{cool}(z,t)}{\partial t} =$$

$$P_h(z,t) q''_{pin-surf}(z,t) - \dot{m}_{channel}^{cool}(t) c_p^{cool}(z,t) \frac{\partial T^{cool}(z,t)}{\partial z} \qquad (2.1)$$

where $\rho^{cool}(z,t)$ = coolant density at elevation z on the pin axis at time t [g/cm^3]

$A_c^{channel}(z,t)$ = cross-sectional area of the single coolant channel at elevation z on

the pin axis at time t [cm^2]

$c_p^{cool}(z,t)$ = heat capacity of the coolant at elevation z at time t [J/g-K]

$T^{cool}(z,t)$ = coolant temperature at elevation z at time t [K]

$P_h(z,t)$ = heated perimeter of the single coolant channel at elevation z on the pin

axis at time t [cm]

$q''_{pin-surf}(z,t)$ = incoming heat flux from the fuel pin surface at elevation z on the

pin axis at time t [W/cm^2]

$\dot{m}_{channel}^{cool}(t)$ = coolant mass flow rate in the single channel at time t [g/s].

User-supplied linear heat generation rates (LHGRs), which are given for each time period, are used to calculate the local fuel pin surface heat flux. The coolant inlet temperature and mass flow rate are given as user-supplied boundary conditions, and can be specified for each time period. The cross-sectional area and heated perimeter of the single coolant channel are computed with the given values for pin pitch and pin radius as

22

depicted in Figure 2.2, which shows a schematic geometry of the single coolant channel in the sodium fast reactor.
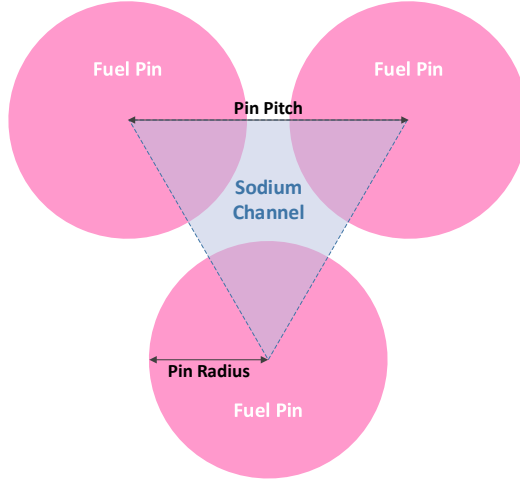
Figure 2.2. Schematic geometry of the single coolant channel in the sodium fast reactor.

$$P_h(z,t) = \pi r_{pin}(z,t) \qquad (2.2)$$

$$A_c^{channel}(z,t) = \frac{\sqrt{3}L^2 - 2\pi\left[r_{pin}(z,t)\right]^2}{4} \qquad (2.3)$$

where $r_{pin}(z,t)$ = fuel pin radius at elevation z at time t [cm]

L = pin pitch [cm].

The fuel pin radius varies with the axial positon and time due to the cladding displacements, while the pin pitch is assumed to be invariant during irradiation time.

Steady State

When power and boundary condition changes are sufficiently slow for the term "steady state" to apply [26], the linear heat removed by the coolant flow is fully compensated by

23

the linear heat coming from the fuel pin. Thus, the thermal energy of coolant per unit of channel length does not change in time, and the left-hand side of Equation 2.1 becomes zero. Integration of the steady state equation yields an expression for the coolant temperature:

$$T^{cool}(b) - T^{cool}(a) = \int_a^b \frac{P_h(z)\, q''_{pin-surf}(z)}{\dot{m}^{cool}_{channel}\, c_p^{cool}(z)}\, dz \tag{2.4}$$

When the linear heat generation rates are given as a piecewise-linear function of z, applying Equation 2.4 over axial section *(i)* leads to the following equation for the coolant temperature at axial node $z_{(i+1)}$:

$$T^{cool}_{(i+1)} = T^{cool}_{(i)} + \frac{f_h}{\dot{m}^{cool}_{channel}\, c_p^{cool-s(i)}} \sum_{n=1}^{N} \frac{p_{\left(i+\frac{n-1}{N}\right)} + p_{\left(i+\frac{n}{N}\right)}}{2} \left(z_{\left(i+\frac{n}{N}\right)} - z_{\left(i+\frac{n-1}{N}\right)} \right) \tag{2.5}$$

where $T^{cool}_{(i)}$ = coolant temperature at axial node $z_{(i)}$ [K] (if $i = 1$, $T^{cool}_{(i)} = T^{cool}_{(1)}$ which is

the coolant inlet temperature T^{cool}_{inlet} given by the boundary conditions)

$c_p^{cool-s(i)}$ = average heat capacity of the coolant in axial section *(i)* [J/g-K]

f_h = fraction of incoming linear heat = $\dfrac{P_h^{s(i)}}{2\pi r_{pin}^{s(i)}}$ ($f_h = \dfrac{1}{2}$ for the triangular channel

of SFRs)

$\Delta z^{s(i)}$ = length of axial section *(i)* [cm] = $z_{(i+1)} - z_{(i)}$ = $\displaystyle\sum_{n=1}^{N}\left(z_{\left(i+\frac{n}{N}\right)} - z_{\left(i+\frac{n-1}{N}\right)} \right)$

N = number of pieces of the linear power function pertaining to axial section *(i)*

$p_{(i)}$ = linear heat generation rate at axial node $z_{(i)}$ [W/cm].

Equation 2.5 is based on an assumption that the heat capacity of the coolant is constant within an axial section to which the equation is applied. Therefore, the size of axial sections should be small enough for the heat capacity to be reasonably represented by the sectional average. Figure 2.3 shows a coolant temperature distribution computed by the TAMU-ZFP code when the linear heat generation rate is given by the code user as a piecewise-linear function.
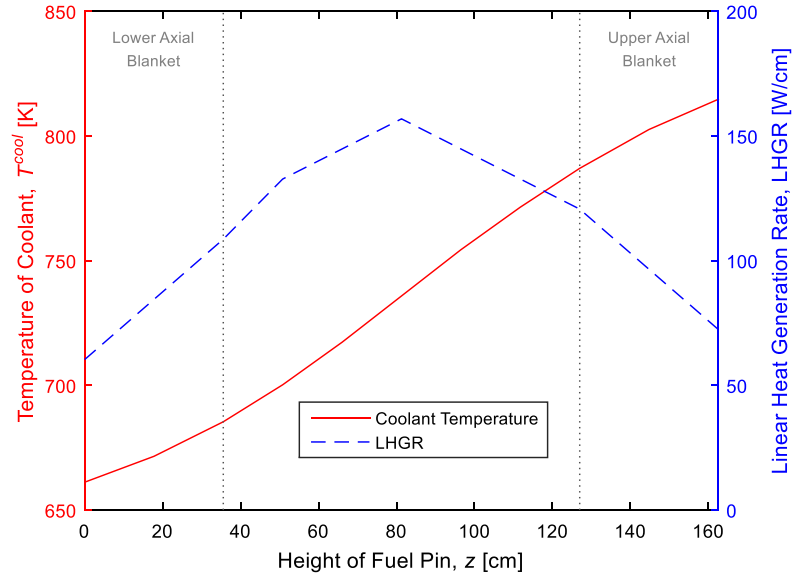
Figure 2.3. Coolant temperature distribution in the single channel where the pin-average of a user-supplied LHGR is 117.1 W/cm. The coolant mass flow rate and the coolant inlet temperature used in the calculation are 48.68 g/s and 661.15 K, respectively.

If the linear heat generation rates have a chopped cosine shape, the coolant temperature at axial node $z_{(i+1)}$ is written as

$$T_{(i+1)}^{cool} = T_{(i)}^{cool} + \frac{f_h}{\dot{m}_{channel}^{cool} c_p^{cool-s(i)}} \cdot Composite\_Simpson\left(p(z),\ z_{(i)},\ z_{(i+1)} \right) \qquad (2.6)$$

25

where *Composite_Simpson*($p(z)$, $z_{(i)}$, $z_{(i+1)}$) is a numerical function that computes the integral with respect to z of the linear heat generation rate function $p(z)$ on the interval [$z_{(i)}$, $z_{(i+1)}$], using the composite Simpson's 1/3 rule[1]. Figure 2.4 shows a result of the coolant temperature calculation for the case in which the LHGR has a cosine shape.
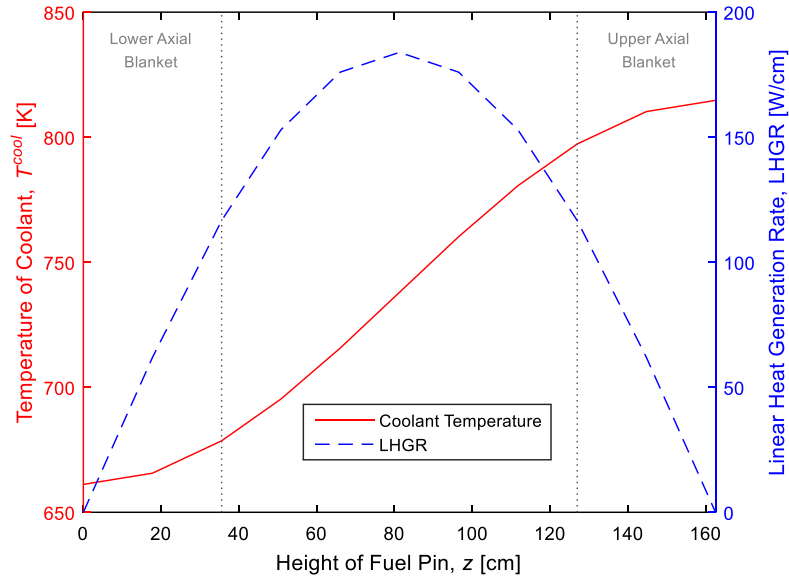
Figure 2.4. Coolant temperature distribution in the single channel where the pin-average of a cosine-shaped LHGR is 117.1 W/cm. The coolant mass flow rate and the coolant inlet temperature used in the calculation are 48.68 g/s and 661.15 K, respectively.

Transient State

The rapid change of reactor operating conditions, like power ramps, induces a transient state where the linear heat taken by the coolant flow is not balanced with the incoming linear heat from the fuel pin to the coolant channel. Thus, the thermal energy of coolant

---

[1]The composite Simpson's 1/3 rule is one of the Newton-Cotes integration formulas, which uses the composite rule and Simpson's 1/3 rule.

per unit of channel length varies with time, and Equation 2.1 should be treated in the full form of a hyperbolic partial differential equation. The Lax-Wendroff one step method is one of the most efficient and stable numerical algorithms for the linear hyperbolic partial differential equation, and is hardly influenced by the implicit numerical diffusion term[2].
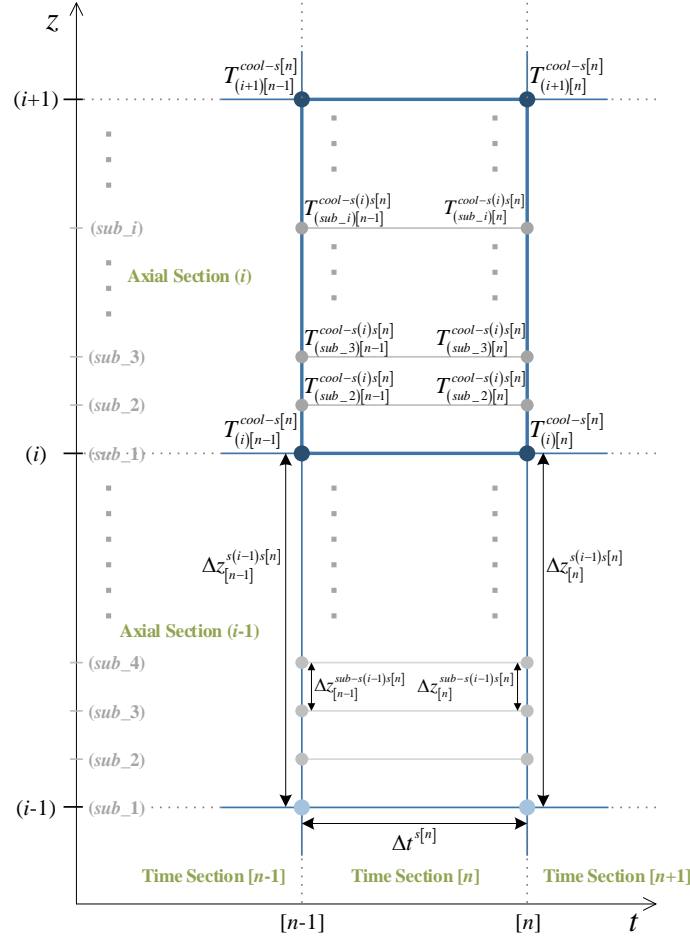
Figure 2.5. Stencil for the Lax-Wendroff one step method. The stencil shows a spatial and temporal discretization of the coolant temperature.

---

[2]The implicit numerical diffusion term is also known as the implicit numerical dissipation term or artificial diffusion term. It can appear in the modified differential equation (MDE), and contributes to the increase of the numerical error by lowering the amplitude and curvature of the numerical solution.

Applying Equation 2.1 to axial section *(i)* of the coolant for time period *[n]* yields

$$\frac{\partial T^{cool}(z,t)}{\partial t} =$$

$$\frac{P_h^{s(i)s[n]} q''^{s(i)s[n]}_{pin-surf}}{\rho^{cool-s(i)s[n]} A_c^{channel-s(i)s[n]} c_p^{cool-s(i)s[n]}} - \frac{\dot{m}^{cool-s[n]}_{channel}}{\rho^{cool-s(i)s[n]} A_c^{channel-s(i)s[n]}} \frac{\partial T^{cool}(z,t)}{\partial z} \quad (2.7)$$

The cross-sectional area and heated perimeter of the coolant channel, density and heat capacity of the coolant, and mass flow rate are considered to be constant within axial section *(i)* for time section *[n]*[3] and have been represented by the sectional averages. When the Lax-Wendroff one step method is implemented to Equation 2.7 at axial sub-node $z_{(sub\_i)}$ in axial section *(i)* shown in Figure 2.5, the following finite difference equation is obtained:

$$T^{cool-s(i)s[n]}_{(sub\_i)[n]} = T^{cool-s(i)s[n]}_{(sub\_i)[n-1]} - \frac{1}{2}\left(\frac{a^{s(i)s[n]}\Delta t^{s[n]}}{\Delta z^{sub-s(i)s[n]}_{[n-1]}}\right)\left(T^{cool-s(i)s[n]}_{(sub\_i+1)[n-1]} - T^{cool-s(i)s[n]}_{(sub\_i-1)[n-1]}\right)$$

$$+ b^{s(i)s[n]}\Delta t^{s[n]} + \frac{1}{2}\left(\frac{a^{s(i)s[n]}\Delta t^{s[n]}}{\Delta z^{sub-s(i)s[n]}_{[n-1]}}\right)^2\left(T^{cool-s(i)s[n]}_{(sub\_i+1)[n-1]} - 2T^{cool-s(i)s[n]}_{(sub\_i)[n-1]} + T^{cool-s(i)s[n]}_{(sub\_i-1)[n-1]}\right) \quad (2.8)$$

where $T^{cool-s(i)s[n]}_{(sub\_i+1)[n-1]}$ = coolant temperature at axial sub-node $z^{s(i)s[n]}_{(sub\_i+1)[n-1]}$ in axial section *(i)*

at time $t_{[n-1]}$ of time section *[n]* [K]

$\Delta t^{s[n]}$ = size of time section *[n]* [s] = $t_{[n]} - t_{[n-1]}$

$a^{s(i)s[n]}$ = average coolant velocity in axial section *(i)* for time section *[n]* [cm/s]

$$= \frac{\dot{m}^{cool-s[n]}_{channel}}{\rho^{cool-s(i)s[n]} A_c^{channel-s(i)s[n]}}$$

---

[3]Time section *[n]* indicates the time period from $t_{[n-1]}$ to $t_{[n]}$.

$b^{s(i)s[n]}$ = average coolant temperature increase rate by the fuel pin surface heat flux

in axial section *(i)* for time section *[n]* [K/s]

$$= \frac{P_h^{s(i)s[n]} q_{pin-surf}^{\prime\prime s(i)s[n]}}{\rho^{cool-s(i)s[n]} A_c^{channel-s(i)s[n]} c_p^{cool-s(i)s[n]}}$$

$\Delta z_{[n-1]}^{sub-s(i)s[n]}$ = size of axial sub-sections in axial section *(i)* at time $t_{[n-1]}$ of time

section *[n]* [cm]

$$= z_{(sub\_2)[n-1]}^{s(i)s[n]} - z_{(sub\_1)[n-1]}^{s(i)s[n]} = \cdots = z_{(sub\_i+1)[n-1]}^{s(i)s[n]} - z_{(sub\_i)[n-1]}^{s(i)s[n]} = \cdots \text{ (the size of}$$

axial sub-sections in axial section *(i)* is uniform).

The Courant-Friedrichs-Lewy (CFL) condition for Equation 2.8 is

$$C^{s(i)s[n]} \leq 1 \tag{2.9}$$

where $C^{s(i)s[n]}$ = Courant number in axial section *(i)* for time section *[n]* [dimensionless]

$$= \frac{a^{s(i)s[n]} \Delta t^{s[n]}}{\Delta z_{[n-1]}^{sub-s(i)s[n]}}.$$

This condition means that the numerical propagation velocity ($\Delta z/\Delta t$) should be higher

than the physical propagation velocity (*a*) in order to maintain stability[4]. If the Courant

number is one, Equation 2.8 becomes the exact solution. On the other hand, the solution

is gradually affected by the implicit numerical dispersion as the Courant number

approaches to zero. The implicit numerical dispersion induces the oscillation of the

numerical solution, which results in the increase of error. Therefore, to make the Courant

---

[4]The numerical domain of dependence includes the physical domain of dependence when the numerical propagation velocity is higher than the physical propagation velocity.

number in axial section *(i)* for time section *[n]* close to 1, the size of axial sub-sections in axial section *(i)* must properly be determined according to the size of time section *[n]*.

Equation 2.8 explicitly calculates the coolant temperature at axial sub-node $z_{(sub\_i)}$ from the temperatures at the previous time node, and it corresponds with the characteristic of hyperbolic partial differential equations that have a finite propagation velocity. The temperatures at the other axial sub-nodes in axial section *(i)* are also calculated in the same way, using the equations derived by the Lax-Wendroff one step method. However, the last axial sub-node in axial section *(i)* is an open boundary, and the temperature at the open boundary should be calculated by the following equation which employs a modified Lax-Wendroff one step method:

$$
\begin{aligned}
T_{(sub\_top)[n]}^{cool-s(i)s[n]} &= T_{(sub\_top)[n-1]}^{cool-s(i)s[n]} + b^{s(i)s[n]}\Delta t^{s[n]} \\
&\quad -\frac{1}{2}\left(\frac{a^{s(i)s[n]}\Delta t^{s[n]}}{\Delta z_{[n-1]}^{sub-s(i)s[n]}}\right)\left(3T_{(sub\_top)[n-1]}^{cool-s(i)s[n]} - 4T_{(sub\_top-1)[n-1]}^{cool-s(i)s[n]} + T_{(sub\_top-2)[n-1]}^{cool-s(i)s[n]}\right) \\
&\quad +\frac{1}{2}\left(\frac{a^{s(i)s[n]}\Delta t^{s[n]}}{\Delta z_{[n-1]}^{sub-s(i)s[n]}}\right)^{2}\left(2T_{(sub\_top)[n-1]}^{cool-s(i)s[n]} - 5T_{(sub\_top-1)[n-1]}^{cool-s(i)s[n]} + 4T_{(sub\_top-2)[n-1]}^{cool-s(i)s[n]} - T_{(sub\_top-3)[n-1]}^{cool-s(i)s[n]}\right)
\end{aligned}
\tag{2.10}
$$

where $T_{(sub\_top)[n]}^{cool-s(i)s[n]}$ = coolant temperature at the last axial sub-node, $z_{(sub\_top)[n]}^{s(i)s[n]}$, in axial section *(i)* at time $t_{[n]}$ of time section *[n]* [K].

As shown in Equation 2.10, each axial section must have more than three axial sub-sections for the implementation of the modified Lax-Wendroff one step method. Figure 2.6 shows a coolant temperature distribution for a time interval over which the pin-average LHGR and the coolant inlet temperature are maintained at 117.1 W/cm and 661.15 K, respectively.
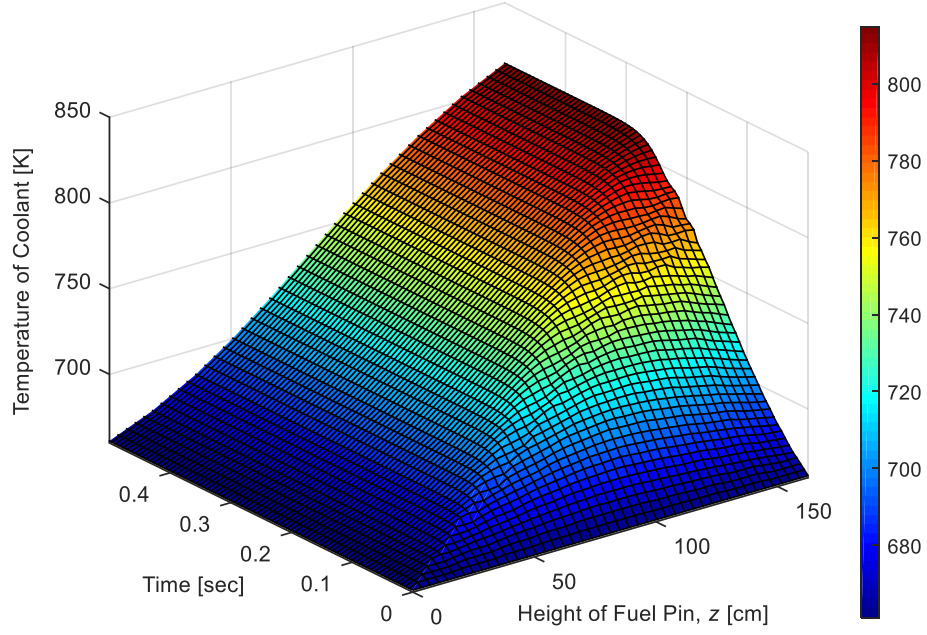
Figure 2.6. Computed coolant temperature distribution in the single channel where the coolant mass flow rate is 48.68 g/s.

2.1.2. Fuel Pin Surface Temperature

The cladding outside temperature is evaluated by a forced convection film temperature drop model:

$$\frac{q''_{pin-surf}(z,t)}{h^{cool}_{conv}(z,t)} = \Delta T^{film}(z,t) \tag{2.11}$$

where $q''_{pin-surf}(z,t)$ = heat flux on the fuel pin surface at elevation z on the pin axis at

time t [W/cm^2]

$\Delta T^{film}(z,t)$ = temperature drop across the coolant film layer by forced convection

$[\text{K}] = T^c_{out}(z,t) - T^{cool}(z,t)$

31

$T_{out}^c\left(z,t\right)$ = cladding outside temperature at elevation z at time t [K]

$h_{conv}^{cool}\left(z,t\right)$ = convective heat transfer coefficient of the coolant at elevation z on the

pin axis at time t [W/cm²-K].

In steady state, the local fuel pin surface heat flux can be obtained from the linear heat generation rate, so Equation 2.11 becomes

$$T_{out}^{c-s(i)} = T^{cool-s(i)} + \frac{p^{s(i)}}{2\pi r_{out}^{c-s(i)}} \frac{1}{h_{conv}^{cool-s(i)}} \qquad (2.12)$$

where $T^{cool-s(i)}$ = average temperature of the coolant in axial section *(i)* [K]

$p^{s(i)}$ = average linear heat generation rate in axial section *(i)* [W/cm]

$$= \int_{z_{(i)}}^{z_{(i+1)}} p\left(z\right)dz \; / \; \left(z_{(i+1)} - z_{(i)}\right)$$

$r_{out}^{c-s(i)}$ = radius up to the outer surface of the cladding in axial section *(i)* [cm].

The average coolant temperature is evaluated from the result of the coolant temperature calculation. Once the coolant temperatures are computed at all the axial nodes, a temperature distribution function can be created by the first degree polynomial regression, and the average coolant temperature in axial section *(i)* is given by

$$T^{cool-s(i)} = \frac{\int_{z_{(i)}}^{z_{(i+1)}} T^{cool}\left(z\right)dz}{z_{(i+1)} - z_{(i)}} \qquad (2.13)$$

The definite integral with respect to z of the temperature distribution function is efficiently handled with the composite trapezoidal rule because the coolant temperatures are expressed as piecewise-linear functions of z.

In transient state, the local fuel pin surface heat flux is directly defined by Fourier's law. The derivative of the cladding temperature with respect to the cladding radius in the Fourier's law can be represented by the high order spatial discretization, and Equation 2.11 becomes

$$T_{\langle c \rangle [n]}^{c-s\langle c \rangle s(i)s[n]} - 4T_{\langle c+\frac{1}{2} \rangle [n]}^{c-s\langle c \rangle s(i)s[n]} + \left(3 + \chi_{[n]}^{s\langle c \rangle s(i)s[n]}\right) T_{\langle c+1 \rangle [n]}^{c-s\langle c \rangle s(i)s[n]} = \chi_{[n]}^{s\langle c \rangle s(i)s[n]} T_{[n]}^{cool-s(i)s[n]} \quad (2.14)$$

where radial section $<c>$ = the outermost radial section of the cladding

$T_{\langle c+1 \rangle [n]}^{c-s\langle c \rangle s(i)s[n]}$ = cladding temperature at the last radial sub-node, $r_{\langle c+1 \rangle [n]}^{c-s(i)s[n]}$, in radial

section $<c>$ of axial section (i) at time $t_{[n]}$ of time section $[n]$ [K]

$$= T_{out[n]}^{c-s(i)s[n]}$$

$\chi_{[n]}^{s\langle c \rangle s(i)s[n]}$ = ratio of the convective heat transfer coefficient of the coolant to the

conductive heat transfer coefficient of the cladding in axial section (i)

at time $t_{[n]}$ of time section $[n]$ = $\dfrac{h_{conv[n]}^{cool-s(i)s[n]} \Delta r_{[n]}^{c-s\langle c \rangle s(i)s[n]}}{k_{[n]}^{c-s\langle c \rangle s(i)s[n]}}$

$\Delta r_{[n]}^{c-s\langle c \rangle s(i)s[n]}$ = size of radial section $<c>$ of the cladding in axial section (i) at time

$t_{[n]}$ of time section $[n]$ [cm] = $r_{\langle c+1 \rangle [n]}^{c-s(i)s[n]} - r_{\langle c \rangle [n]}^{c-s(i)s[n]}$

$k_{[n]}^{c-s\langle c \rangle s(i)s[n]}$ = average thermal conductivity of the cladding in radial section $<c>$ of

axial section (i) at time $t_{[n]}$ of time section $[n]$ [W/cm-K]

$T_{\langle c+\frac{1}{2} \rangle [n]}^{c-s\langle c \rangle s(i)s[n]}$ = cladding temperature at radial sub-node $r_{\langle c+\frac{1}{2} \rangle [n]}^{c-s(i)s[n]}$ in radial section

$<c>$ of axial section (i) at time $t_{[n]}$ of time section $[n]$ [K].

33

The outermost radial section of the cladding contains radial sub-nodes for the transient case because a high order one-way finite difference equation is used for representing the conductive heat transfer at the cladding surface. Equation 2.14 is added into a simultaneous linear system which computes the cladding temperatures in axial section *(i)* at time $t_{[n]}$ of time section *[n]*.

The convective heat transfer coefficient of the coolant in axial section *(i)* at time $t_{[n]}$ of time section *[n]* is given by

$$h_{conv[n]}^{cool-s(i)s[n]} = \frac{k_{[n]}^{cool-s(i)s[n]}}{D_e^{heated-s(i)s[n]}} Nu_{[n]}^{s(i)s[n]}$$

(2.15)

where $k_{[n]}^{cool-s(i)s[n]}$ = average thermal conductivity of the coolant in axial section *(i)* at time

$t_{[n]}$ of time section *[n]* [W/cm-K]

$D_e^{heated-s(i)s[n]}$ = equivalent heated diameter of the coolant channel in axial section

(i) for time section *[n]*[5] [cm] = $4A_c^{channel-s(i)s[n]} / P_h^{s(i)s[n]}$

$Nu_{[n]}^{s(i)s[n]}$ = Nusselt number of the coolant in axial section *(i)* at time $t_{[n]}$ of time

section *[n]* [dimensionless].

Equations 2.2 and 2.3 are used again for the calculation of the equivalent heated diameter.

The Nusselt number can be obtained from the Dittus-Boelter correlation:

---

[5]While the thermal conductivity and Nusselt number of the coolant are values at a specific time node, the equivalent heated diameter of the coolant channel in an axial section was already used as a time-sectional value for the calculation of the coolant temperature. Therefore, in the forced convection film temperature drop model, it is compatibly treated as a constant for a time section. The coolant heat capacity in the Prandtl number and the mass flow rate in the Reynolds number are also time-sectional values due to the same reason.

$$Nu_{[n]}^{s(i)s[n]} = 0.023 \left(\text{Re}_{[n]}^{s(i)s[n]} \right)^{0.8} \left(\text{Pr}_{[n]}^{s(i)s[n]} \right)^{0.4} \tag{2.16}$$

where $\text{Re}_{[n]}^{s(i)s[n]}$ = Reynolds number of the coolant in axial section *(i)* at time $t_{[n]}$ of time

section *[n]* [dimensionless] = $\dfrac{\dot{m}_{channel}^{cool-s[n]} D_e^{hydraulic-s(i)s[n]}}{\mu_{[n]}^{cool-s(i)s[n]} A_c^{channel-s(i)s[n]}}$

$\text{Pr}_{[n]}^{s(i)s[n]}$ = Prandtl number of the coolant in axial section *(i)* at time $t_{[n]}$ of time

section *[n]* [dimensionless] = $\dfrac{c_p^{cool-s(i)s[n]} \mu_{[n]}^{cool-s(i)s[n]}}{k_{[n]}^{cool-s(i)s[n]}}$

$\mu_{[n]}^{cool-s(i)s[n]}$ = average dynamic viscosity of the coolant in axial section *(i)* at time

$t_{[n]}$ of time section *[n]* [P]

$D_e^{hydraulic-s(i)s[n]}$ = equivalent hydraulic diameter of the coolant channel in axial

section *(i)* for time section *[n]* [cm].

The poise, P, is the cgs physical unit for dynamic viscosity, which symbolizes g/cm-s. The

equivalent hydraulic diameter of the single coolant channel in sodium fast reactors has the

same value as the equivalent heated diameter.

2.1.3. Cladding Temperature

The temperature distributions in the cladding region are obtained from an energy balance

equation in which the net current of heat is defined by Fourier's law:

$$\iiint_{volume} \frac{\partial E^c\left(\vec{r},t\right)}{\partial t} dV = -\iint_{surface} \vec{e}_n \cdot \left[-k^c\left(\vec{r},t\right) \vec{\nabla} T^c\left(\vec{r},t\right) \right] dS \tag{2.17}$$

35

where $E^c(\vec{r},t)$ = thermal energy of the cladding per unit volume at point $\vec{r}$ in three-

dimensional space at time t [J/cm^3]

$\vec{e}_n$ = unit vector which is normal to the surface.

Equation 2.17 can be arranged to the following partial differential equation by the Gauss's

divergence theorem which converts the spatial-surface integral to the spatial-volume

integral:

$$\frac{\partial E^c(\vec{r},t)}{\partial t} = -\vec{\nabla} \cdot \left[-k^c(\vec{r},t) \vec{\nabla} T^c(\vec{r},t) \right] \qquad (2.18)$$

Steady State

During steady state, the thermal energy of the cladding does not change in time, and the

net heat flow rate is zero. Thus, in cylindrical coordinates, Equation 2.18 becomes

$$k^c \frac{1}{r} \frac{d}{dr} \left(r \frac{dT^c(r)}{dr} \right) = 0 \qquad (2.19)$$

Heat conduction in the axial and azimuthal directions is considered negligible relative to

radial heat conduction and has been ignored. Equation 2.19 is also based on an assumption

that the thermal conductivity of the cladding is constant within a radial section to which

the equation is applied. Therefore, the radial section should be small enough for the

thermal conductivity to be reasonably represented by the sectional average, and the

equation is valid only within the specific radial section. Applying Equation 2.19 to radial

node $r_{<j>}$ in radial section $<j>$ of axial section *(i)* yields the following finite difference

heat conduction equation:

$$\left(1+\frac{\Delta r^{c-s\langle j\rangle s(i)}}{2r_{\langle j\rangle}^{c-s(i)}}\right)T_{\langle j+1\rangle}^{c-s\langle j\rangle s(i)} - 2T_{\langle j\rangle}^{c-s\langle j\rangle s(i)} + \left(1-\frac{\Delta r^{c-s\langle j\rangle s(i)}}{2r_{\langle j\rangle}^{c-s(i)}}\right)T_{\langle j-1\rangle}^{c-s\langle j\rangle s(i)} = 0 \qquad (2.20)$$

where $T_{\langle j+1\rangle}^{c-s\langle j\rangle s(i)}$ = cladding temperature at radial node $r_{\langle j+1\rangle}^{c-s(i)}$ in radial section <j> of axial

section *(i)* [K]

$\Delta r^{c-s\langle j\rangle s(i)}$ = size of radial section <j> of the cladding in axial section *(i)* [cm]

$$= r_{\langle j+1\rangle}^{c-s(i)} - r_{\langle j\rangle}^{c-s(i)}$$

$T_{\langle j-1\rangle}^{c-s\langle j\rangle s(i)}$ = virtual variable at ghost node $r_{\langle j\rangle}^{c-s(i)} - \Delta r^{c-s\langle j\rangle s(i)}$ [K] (radial section <j>

is from $r_{\langle j\rangle}^{c-s(i)}$ to $r_{\langle j+1\rangle}^{c-s(i)}$).

Equation 2.20 contains virtual variable $T_{\langle j-1\rangle}^{c-s\langle j\rangle s(i)}$ defined at ghost node $r_{\langle j\rangle}^{c-s(i)} - \Delta r^{c-s\langle j\rangle s(i)}$.

$T_{\langle j-1\rangle}^{c-s\langle j\rangle s(i)}$ cannot be identified with $T_{\langle j-1\rangle}^{c-s\langle j-1\rangle s(i)}$ defined at $r_{\langle j-1\rangle}^{c-s(i)}$ because $r_{\langle j-1\rangle}^{c-s(i)}$ is not

$r_{\langle j\rangle}^{c-s(i)} - \Delta r^{c-s\langle j\rangle s(i)}$ but $r_{\langle j\rangle}^{c-s(i)} - \Delta r^{c-s\langle j-1\rangle s(i)}$. Moreover, $T_{\langle j-1\rangle}^{c-s\langle j\rangle s(i)}$ is a variable of the

governing equation established for radial section <j> whose thermal conductivity is

$k^{c-s\langle j\rangle s(i)}$, whereas $T_{\langle j-1\rangle}^{c-s\langle j-1\rangle s(i)}$ is a variable of the governing equation for radial section <j-

1> and is influenced by $k^{c-s\langle j-1\rangle s(i)}$.

The virtual variable can be eliminated by the boundary conditions for radial section

<j> of axial section *(i)*:

$$q_{\langle j\rangle}^{\prime\prime c-s\langle j-1\rangle s(i)} = q_{\langle j\rangle}^{\prime\prime c-s\langle j\rangle s(i)} \qquad (2.21)$$

$$T_{\langle j+1\rangle}^{c-s\langle j\rangle s(i)} = T_{\langle j+1\rangle}^{c-s\langle j+1\rangle s(i)} \qquad (2.22)$$

37

When these boundary conditions are employed for each radial section of axial section *(i)* and are applied to the finite difference heat conduction equations of each radial section for eliminating virtual variables, a simultaneous linear system is finally obtained for axial section *(i)*:

First radial section

$$T_{\langle 1 \rangle}^{c-s(i)} - T_{\langle 2 \rangle}^{c-s(i)} = \left(1 - R_{\langle 1 \rangle}^{c-s\langle 1 \rangle s(i)}\right) R_{\langle 1 \rangle}^{c-s\langle 1 \rangle s(i)} \frac{p^{s(i)}}{\pi k^{c-s\langle 1 \rangle s(i)}} \tag{2.23}$$

Last radial section

$$\frac{k^{c-s\langle c-1 \rangle s(i)}}{\Delta r^{c-s\langle c-1 \rangle s(i)} \left(1 + R_{\langle c \rangle}^{c-s\langle c-1 \rangle s(i)}\right)} T_{\langle c-1 \rangle}^{c-s(i)}$$
$$- \left(\frac{k^{c-s\langle c-1 \rangle s(i)}}{\Delta r^{c-s\langle c-1 \rangle s(i)} \left(1 + R_{\langle c \rangle}^{c-s\langle c-1 \rangle s(i)}\right)} + \frac{k^{c-s\langle c \rangle s(i)}}{\Delta r^{c-s\langle c \rangle s(i)} \left(1 - R_{\langle c \rangle}^{c-s\langle c \rangle s(i)}\right)}\right) T_{\langle c \rangle}^{c-s(i)} \tag{2.24}$$
$$= -\frac{k^{c-s\langle c \rangle s(i)}}{\Delta r^{c-s\langle c \rangle s(i)} \left(1 - R_{\langle c \rangle}^{c-s\langle c \rangle s(i)}\right)} T_{out}^{c-s(i)}$$

The other radial sections

$$\frac{k^{c-s\langle j-1 \rangle s(i)}}{\Delta r^{c-s\langle j-1 \rangle s(i)} \left(1 + R_{\langle j \rangle}^{c-s\langle j-1 \rangle s(i)}\right)} T_{\langle j-1 \rangle}^{c-s(i)}$$
$$- \left(\frac{k^{c-s\langle j-1 \rangle s(i)}}{\Delta r^{c-s\langle j-1 \rangle s(i)} \left(1 + R_{\langle j \rangle}^{c-s\langle j-1 \rangle s(i)}\right)} + \frac{k^{c-s\langle j \rangle s(i)}}{\Delta r^{c-s\langle j \rangle s(i)} \left(1 - R_{\langle j \rangle}^{c-s\langle j \rangle s(i)}\right)}\right) T_{\langle j \rangle}^{c-s(i)} \tag{2.25}$$
$$+ \frac{k^{c-s\langle j \rangle s(i)}}{\Delta r^{c-s\langle j \rangle s(i)} \left(1 - R_{\langle j \rangle}^{c-s\langle j \rangle s(i)}\right)} T_{\langle j+1 \rangle}^{c-s(i)} = 0$$

where $R_{\langle j \rangle}^{c-s\langle j-1 \rangle s(i)}$ = dimensionless number = $\dfrac{\Delta r^{c-s\langle j-1 \rangle s(i)}}{2 r_{\langle j \rangle}^{c-s(i)}}$

radial section *<c>* = the outermost radial section of the cladding

radial section *<j>* = an arbitrary radial section ($1 < j < c$ in Equation 2.25)

$T_{out}^{c-s(i)}$ = cladding outside temperature in axial section *(i)* [K] ($T_{out}^{c-s(i)}$ is given from

the calculation of the film temperature drop).
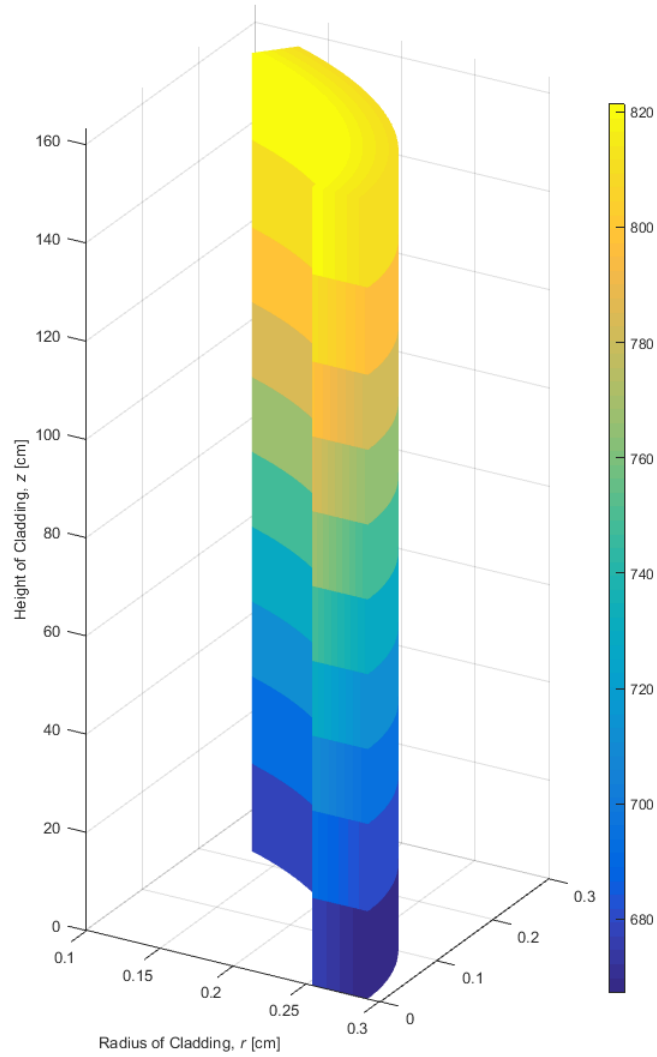
Figure 2.7. Cladding temperature distribution computed by the TAMU-ZFP code. The pin-average LHGR used in the calculation is 117.1 W/cm.
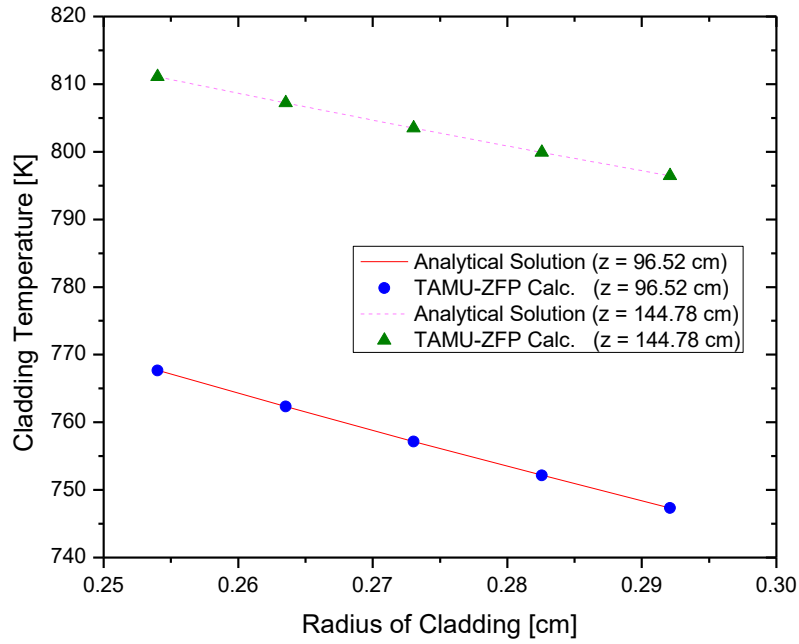
Figure 2.8. Comparison of the computed cladding temperature with the analytical solution.

The number of equations contained in the simultaneous linear system is equal to the number of radial sections of axial section *(i)*. These equations are fully compatible with the adaptable mesh system mentioned previously because the boundary conditions are applied not only to the inside and outside of the cladding but also to the boundaries of each flexible radial section. The coefficient matrix of the simultaneous linear system has the form of a tridiagonal matrix, so TDMA, which is also known as the Thomas algorithm, can be used to find out the cladding temperature distribution in axial section *(i)*. Similar simultaneous linear systems are given to other axial sections and can be treated in the same way. Figure 2.7 shows a cladding temperature distribution computed by the TAMU-ZFP

code. The result of the code calculation has been compared with the analytical solution in Figure 2.8, and they are well matched to each other at all of the axial sections. The analytical solution used in the comparison is represented in APPENDIX A.

Transient State

The net flow rate of heat is not zero in transient state, and the imbalance in the heat flow rate induces the change of the cladding thermal energy with time. Thus, Equation 2.18 should be handled in the full form of a parabolic partial differential equation. Applying Equation 2.18 to radial section *<j>* of axial section *(i)* for time section *[n]* yields

$$
\frac{\partial T^{c-s\langle j\rangle s(i)s[n]}(r,t)}{\partial t} = \\
\frac{k^{c-s\langle j\rangle s(i)s[n]}(t)}{\rho^{c-s\langle j\rangle s(i)s[n]}(r,t)c_p^{c-s\langle j\rangle s(i)s[n]}(r,t)} \frac{1}{r}\frac{\partial}{\partial r}\left(r\frac{\partial T^{c-s\langle j\rangle s(i)s[n]}(r,t)}{\partial r}\right)
$$

(2.26)

where $\rho^{c-s\langle j\rangle s(i)s[n]}(r,t)$ = density of the cladding at radius *r* in radial section *<j>* of axial

section *(i)* at time *t* of time section *[n]* [g/cm^3]

$c_p^{c-s\langle j\rangle s(i)s[n]}(r,t)$ = heat capacity of the cladding at radius *r* in radial section *<j>* of

axial section *(i)* at time *t* of time section *[n]* [J/g-K]

$k^{c-s\langle j\rangle s(i)s[n]}(t)$ = average thermal conductivity of the cladding in radial section *<j>*

of axial section *(i)* at time *t* of time section *[n]* [W/cm-K].

Like the steady state equation (Equation 2.19), Equation 2.26 is based on the assumption that the thermal conductivity of the cladding is not a function of *r* within a radial section. At radial node $r_{<j>}$, the equation can be approximated to the following finite difference heat conduction equation by the Crank-Nicolson method:

41

$$V_{\langle j\rangle[n]}^{c-s\langle j\rangle s(i)s[n]}\left(1+R_{\langle j\rangle[n]}^{c-s\langle j\rangle s(i)s[n]}\right)T_{\langle j+1\rangle[n]}^{c-s\langle j\rangle s(i)s[n]}$$

$$-2\left(1+V_{\langle j\rangle[n]}^{c-s\langle j\rangle s(i)s[n]}\right)T_{\langle j\rangle[n]}^{c-s\langle j\rangle s(i)s[n]}+V_{\langle j\rangle[n]}^{c-s\langle j\rangle s(i)s[n]}\left(1-R_{\langle j\rangle[n]}^{c-s\langle j\rangle s(i)s[n]}\right)T_{\langle j-1\rangle[n]}^{c-s\langle j\rangle s(i)s[n]}$$

$$=-V_{\langle j\rangle[n-1]}^{c-s\langle j\rangle s(i)s[n]}\left(1+R_{\langle j\rangle[n-1]}^{c-s\langle j\rangle s(i)s[n]}\right)T_{\langle j+1\rangle[n-1]}^{c-s\langle j\rangle s(i)s[n]}$$

$$-2\left(1-V_{\langle j\rangle[n-1]}^{c-s\langle j\rangle s(i)s[n]}\right)T_{\langle j\rangle[n-1]}^{c-s\langle j\rangle s(i)s[n]}-V_{\langle j\rangle[n-1]}^{c-s\langle j\rangle s(i)s[n]}\left(1-R_{\langle j\rangle[n-1]}^{c-s\langle j\rangle s(i)s[n]}\right)T_{\langle j-1\rangle[n-1]}^{c-s\langle j\rangle s(i)s[n]} \tag{2.27}$$

where $V_{\langle j\rangle[n-1]}^{c-s\langle j\rangle s(i)s[n]}$ = diffusion number at radial node $r_{\langle j\rangle[n-1]}^{c-s(i)s[n]}$ in radial section $<j>$ of axial

section (i) at time $t_{[n-1]}$ of time section $[n]$ [dimensionless]

$$=\frac{\alpha_{D\langle j\rangle[n-1]}^{c-s\langle j\rangle s(i)s[n]}\Delta t^{s[n]}}{\left(\Delta r_{[n-1]}^{c-s\langle j\rangle s(i)s[n]}\right)^2}$$

$\alpha_{D\langle j\rangle[n-1]}^{c-s\langle j\rangle s(i)s[n]}$ = thermal diffusivity of the cladding at radial node $r_{\langle j\rangle[n-1]}^{c-s(i)s[n]}$ in radial

section $<j>$ of axial section (i) at time $t_{[n-1]}$ of time section $[n]$

$$[\text{cm}^2/\text{s}]=\frac{k_{[n-1]}^{c-s\langle j\rangle s(i)s[n]}}{\rho_{\langle j\rangle[n-1]}^{c-s\langle j\rangle s(i)s[n]}c_{p\langle j\rangle[n-1]}^{c-s\langle j\rangle s(i)s[n]}}$$

$\Delta t^{s[n]}$ = size of time section $[n]$ [s] = $t_{[n]}-t_{[n-1]}$

$$R_{\langle j\rangle[n-1]}^{c-s\langle j\rangle s(i)s[n]}=\text{dimensionless number}=\frac{\Delta r_{[n-1]}^{c-s\langle j\rangle s(i)s[n]}}{2r_{\langle j\rangle[n-1]}^{c-s(i)s[n]}}.$$

The boundary conditions for radial section $<j>$ of axial section (i) are

$$q_{\langle j\rangle[n-1]}''^{c-s\langle j-1\rangle s(i)s[n]}=q_{\langle j\rangle[n-1]}''^{c-s\langle j\rangle s(i)s[n]} \tag{2.28}$$

$$T_{\langle j+1\rangle[n-1]}^{c-s\langle j\rangle s(i)s[n]}=T_{\langle j+1\rangle[n-1]}^{c-s\langle j+1\rangle s(i)s[n]} \tag{2.29}$$

at time $t_{[n-1]}$ of time section $[n]$, and

$$q''^{c-s\langle j-1\rangle s(i)s[n]}_{\langle j\rangle[n]} = q''^{c-s\langle j\rangle s(i)s[n]}_{\langle j\rangle[n]} \tag{2.30}$$

$$T^{c-s\langle j\rangle s(i)s[n]}_{\langle j+1\rangle[n]} = T^{c-s\langle j+1\rangle s(i)s[n]}_{\langle j+1\rangle[n]} \tag{2.31}$$

at time $t_{[n]}$ of time section *[n]*.

Equation 2.27 contains virtual variables $T^{c-s\langle j\rangle s(i)s[n]}_{\langle j-1\rangle[n-1]}$ and $T^{c-s\langle j\rangle s(i)s[n]}_{\langle j-1\rangle[n]}$ defined at ghost nodes $r^{c-s(i)s[n]}_{\langle j\rangle[n-1]} - \Delta r^{c-s\langle j\rangle s(i)s[n]}_{[n-1]}$ and $r^{c-s(i)s[n]}_{\langle j\rangle[n]} - \Delta r^{c-s\langle j\rangle s(i)s[n]}_{[n]}$, respectively. In the case of steady state finite difference heat conduction equations, their virtual variables were removed by applying boundary conditions. However, the virtual variables in the transient equations cannot be eliminated by the boundary conditions due to the time dependence of the material properties in addition to their spatial variation. Therefore, a modified Crank-Nicolson scheme, which employs the three-point backward difference formula for the left-hand side of the Neumann boundary conditions[6], is used instead of the original scheme in order to derive transient finite difference heat conduction equations appropriate to the application of boundary conditions and to the removal of virtual variables. After the

---

[6]Introducing the three-point backward difference formula into the left-hand side of the Neumann boundary condition for radial section *<j>* of axial section *(i)* at $t_{[n-1]}$ of time section *[n]* (Equation 2.28) gives

$$-k^{c-s\langle j-1\rangle s(i)s[n]}_{[n-1]} \frac{3T^{c-s\langle j-1\rangle s(i)s[n]}_{\langle j\rangle[n-1]} - 4T^{c-s\langle j-1\rangle s(i)s[n]}_{\langle j-1/2\rangle[n-1]} + T^{c-s\langle j-1\rangle s(i)s[n]}_{\langle j-1\rangle[n-1]}}{2\left(\dfrac{\Delta r^{c-s\langle j-1\rangle s(i)s[n]}_{[n-1]}}{2}\right)} = -k^{c-s\langle j\rangle s(i)s[n]}_{[n-1]} \frac{T^{c-s\langle j\rangle s(i)s[n]}_{\langle j+1/2\rangle[n-1]} - T^{c-s\langle j\rangle s(i)s[n]}_{\langle j-1/2\rangle[n-1]}}{2\left(\dfrac{\Delta r^{c-s\langle j\rangle s(i)s[n]}_{[n-1]}}{2}\right)}$$

where $T^{c-s\langle j\rangle s(i)s[n]}_{\langle j-1/2\rangle[n-1]}$ is one of the virtual variables which need to be removed from the transient finite difference heat conduction equation derived at radial node $r_{<j>}$ in radial section *<j>* of axial section *(i)* for time section *[n]*.

43

modified numerical scheme has been implemented at the radial nodes in each radial section, combining the modified finite difference equations with the boundary conditions for all the radial sections of axial section *(i)* for time section *[n]* gives a simultaneous linear system for axial section *(i)* at time $t_{[n]}$ of time section *[n]*:

First radial section (radial section *<1>*)

$$
\begin{aligned}
V_{D\langle 1\rangle[n]}^{c-s\langle 1\rangle s(i)s[n]} & \left(1 - R_{sub\langle 1\rangle[n]}^{c-s\langle 1\rangle s(i)s[n]}\right) W_{[n]}^{c-s\langle 1\rangle s(i)s[n]} T_{\langle g\rangle[n]}^{g-s(i)s[n]} \\
& - 4 V_{D\langle 1\rangle[n]}^{c-s\langle 1\rangle s(i)s[n]} \left(1 - R_{sub\langle 1\rangle[n]}^{c-s\langle 1\rangle s(i)s[n]}\right) W_{[n]}^{c-s\langle 1\rangle s(i)s[n]} T_{\langle g+\frac{1}{2}\rangle[n]}^{g-s(i)s[n]} \\
+ & \left[3 V_{D\langle 1\rangle[n]}^{c-s\langle 1\rangle s(i)s[n]} \left(1 - R_{sub\langle 1\rangle[n]}^{c-s\langle 1\rangle s(i)s[n]}\right) W_{[n]}^{c-s\langle 1\rangle s(i)s[n]} + 2\left(1 + V_{D\langle 1\rangle[n]}^{c-s\langle 1\rangle s(i)s[n]}\right) \right] T_{\langle 1\rangle[n]}^{c-s(i)s[n]} \\
& \qquad\qquad\qquad\qquad - 2 V_{D\langle 1\rangle[n]}^{c-s\langle 1\rangle s(i)s[n]} T_{\langle 1.5\rangle[n]}^{c-s(i)s[n]} \\
= - & V_{D\langle 1\rangle[n-1]}^{c-s\langle 1\rangle s(i)s[n]} \left(1 - R_{sub\langle 1\rangle[n-1]}^{c-s\langle 1\rangle s(i)s[n]}\right) W_{[n-1]}^{c-s\langle 1\rangle s(i)s[n]} T_{\langle g\rangle[n-1]}^{g-s(i)s[n]} \\
& + 4 V_{D\langle 1\rangle[n-1]}^{c-s\langle 1\rangle s(i)s[n]} \left(1 - R_{sub\langle 1\rangle[n-1]}^{c-s\langle 1\rangle s(i)s[n]}\right) W_{[n-1]}^{c-s\langle 1\rangle s(i)s[n]} T_{\langle g+\frac{1}{2}\rangle[n-1]}^{g-s(i)s[n]} \\
- & \left[3 V_{D\langle 1\rangle[n-1]}^{c-s\langle 1\rangle s(i)s[n]} \left(1 - R_{sub\langle 1\rangle[n-1]}^{c-s\langle 1\rangle s(i)s[n]}\right) W_{[n-1]}^{c-s\langle 1\rangle s(i)s[n]} - 2\left(1 - V_{D\langle 1\rangle[n-1]}^{c-s\langle 1\rangle s(i)s[n]}\right) \right] T_{\langle 1\rangle[n-1]}^{c-s(i)s[n]} \\
& \qquad\qquad\qquad\qquad + 2 V_{D\langle 1\rangle[n-1]}^{c-s\langle 1\rangle s(i)s[n]} T_{\langle 1.5\rangle[n-1]}^{c-s(i)s[n]}
\end{aligned}
\tag{2.32}
$$

at radial sub-node $r_{\langle 1\rangle\left[n-\frac{1}{2}\right]}^{c-s(i)s[n]}$, and

$$
\begin{aligned}
V_{D\langle 1.5\rangle[n]}^{c-s\langle 1\rangle s(i)s[n]} & \left(1 - R_{sub\langle 1.5\rangle[n]}^{c-s\langle 1\rangle s(i)s[n]}\right) T_{\langle 1\rangle[n]}^{c-s(i)s[n]} \\
& - 2\left(1 + V_{D\langle 1.5\rangle[n]}^{c-s\langle 1\rangle s(i)s[n]}\right) T_{\langle 1.5\rangle[n]}^{c-s(i)s[n]} + V_{D\langle 1.5\rangle[n]}^{c-s\langle 1\rangle s(i)s[n]} \left(1 + R_{sub\langle 1.5\rangle[n]}^{c-s\langle 1\rangle s(i)s[n]}\right) T_{\langle 2\rangle[n]}^{c-s(i)s[n]} \\
= - & V_{D\langle 1.5\rangle[n-1]}^{c-s\langle 1\rangle s(i)s[n]} \left(1 - R_{sub\langle 1.5\rangle[n-1]}^{c-s\langle 1\rangle s(i)s[n]}\right) T_{\langle 1\rangle[n-1]}^{c-s(i)s[n]} \\
& - 2\left(1 - V_{D\langle 1.5\rangle[n-1]}^{c-s\langle 1\rangle s(i)s[n]}\right) T_{\langle 1.5\rangle[n-1]}^{c-s(i)s[n]} - V_{D\langle 1.5\rangle[n-1]}^{c-s\langle 1\rangle s(i)s[n]} \left(1 + R_{sub\langle 1.5\rangle[n-1]}^{c-s\langle 1\rangle s(i)s[n]}\right) T_{\langle 2\rangle[n-1]}^{c-s(i)s[n]}
\end{aligned}
\tag{2.33}
$$

at radial sub-node $r_{\langle 1.5\rangle\left[n-\frac{1}{2}\right]}^{c-s(i)s[n]}$

The others (arbitrary radial section $<j>$, $1 < j \leq c$)

$$
\begin{aligned}
V_{D\langle j\rangle[n]}^{c-s\langle j\rangle s(i)s[n]} &\left(1 - R_{sub\langle j\rangle[n]}^{c-s\langle j\rangle s(i)s[n]}\right) W_{[n]}^{c-s\langle j\rangle s(i)s[n]} T_{\langle j-1\rangle[n]}^{c-s(i)s[n]} \\
&- 4V_{D\langle j\rangle[n]}^{c-s\langle j\rangle s(i)s[n]}\left(1 - R_{sub\langle j\rangle[n]}^{c-s\langle j\rangle s(i)s[n]}\right) W_{[n]}^{c-s\langle j\rangle s(i)s[n]} T_{\langle j-\frac{1}{2}\rangle[n]}^{c-s(i)s[n]} \\
+ \Bigg[3V_{D\langle j\rangle[n]}^{c-s\langle j\rangle s(i)s[n]} &\left(1 - R_{sub\langle j\rangle[n]}^{c-s\langle j\rangle s(i)s[n]}\right) W_{[n]}^{c-s\langle j\rangle s(i)s[n]} + 2\left(1 + V_{D\langle j\rangle[n]}^{c-s\langle j\rangle s(i)s[n]}\right) \Bigg] T_{\langle j\rangle[n]}^{c-s(i)s[n]} \\
&\qquad\qquad\qquad\qquad\qquad - 2V_{D\langle j\rangle[n]}^{c-s\langle j\rangle s(i)s[n]} T_{\langle j+\frac{1}{2}\rangle[n]}^{c-s(i)s[n]} \\
= -V_{D\langle j\rangle[n-1]}^{c-s\langle j\rangle s(i)s[n]} &\left(1 - R_{sub\langle j\rangle[n-1]}^{c-s\langle j\rangle s(i)s[n]}\right) W_{[n-1]}^{c-s\langle j\rangle s(i)s[n]} T_{\langle j-1\rangle[n-1]}^{c-s(i)s[n]} \\
&+ 4V_{D\langle j\rangle[n-1]}^{c-s\langle j\rangle s(i)s[n]}\left(1 - R_{sub\langle j\rangle[n-1]}^{c-s\langle j\rangle s(i)s[n]}\right) W_{[n-1]}^{c-s\langle j\rangle s(i)s[n]} T_{\langle j-\frac{1}{2}\rangle[n-1]}^{c-s(i)s[n]} \\
- \Bigg[3V_{D\langle j\rangle[n-1]}^{c-s\langle j\rangle s(i)s[n]} &\left(1 - R_{sub\langle j\rangle[n-1]}^{c-s\langle j\rangle s(i)s[n]}\right) W_{[n-1]}^{c-s\langle j\rangle s(i)s[n]} - 2\left(1 - V_{D\langle j\rangle[n-1]}^{c-s\langle j\rangle s(i)s[n]}\right) \Bigg] T_{\langle j\rangle[n-1]}^{c-s(i)s[n]} \\
&\qquad\qquad\qquad\qquad\qquad + 2V_{D\langle j\rangle[n-1]}^{c-s\langle j\rangle s(i)s[n]} T_{\langle j+\frac{1}{2}\rangle[n-1]}^{c-s(i)s[n]}
\end{aligned}
\tag{2.34}
$$

at radial sub-node $r_{\langle j\rangle\left[n-\frac{1}{2}\right]}^{c-s(i)s[n]}$, and

$$
\begin{aligned}
V_{D\langle j+\frac{1}{2}\rangle[n]}^{c-s\langle j\rangle s(i)s[n]} &\left(1 - R_{sub\langle j+\frac{1}{2}\rangle[n]}^{c-s\langle j\rangle s(i)s[n]}\right) T_{\langle j\rangle[n]}^{c-s(i)s[n]} \\
&- 2\left(1 + V_{D\langle j+\frac{1}{2}\rangle[n]}^{c-s\langle j\rangle s(i)s[n]}\right) T_{\langle j+\frac{1}{2}\rangle[n]}^{c-s(i)s[n]} + V_{D\langle j+\frac{1}{2}\rangle[n]}^{c-s\langle j\rangle s(i)s[n]}\left(1 + R_{sub\langle j+\frac{1}{2}\rangle[n]}^{c-s\langle j\rangle s(i)s[n]}\right) T_{\langle j+1\rangle[n]}^{c-s(i)s[n]} \\
= -V_{D\langle j+\frac{1}{2}\rangle[n-1]}^{c-s\langle j\rangle s(i)s[n]} &\left(1 - R_{sub\langle j+\frac{1}{2}\rangle[n-1]}^{c-s\langle j\rangle s(i)s[n]}\right) T_{\langle j\rangle[n-1]}^{c-s(i)s[n]} \\
&- 2\left(1 - V_{D\langle j+\frac{1}{2}\rangle[n-1]}^{c-s\langle j\rangle s(i)s[n]}\right) T_{\langle j+\frac{1}{2}\rangle[n-1]}^{c-s(i)s[n]} - V_{D\langle j+\frac{1}{2}\rangle[n-1]}^{c-s\langle j\rangle s(i)s[n]}\left(1 + R_{sub\langle j+\frac{1}{2}\rangle[n-1]}^{c-s\langle j\rangle s(i)s[n]}\right) T_{\langle j+1\rangle[n-1]}^{c-s(i)s[n]}
\end{aligned}
\tag{2.35}
$$

at radial sub-node $r_{\langle j+\frac{1}{2}\rangle\left[n-\frac{1}{2}\right]}^{c-s(i)s[n]}$

where $V_{D\langle j+\frac{1}{2}\rangle[n-1]}^{c-s\langle j\rangle s(i)s[n]}$ = diffusion number at radial sub-node $r_{\langle j+\frac{1}{2}\rangle[n-1]}^{c-s(i)s[n]}$ in radial section $<j>$

of axial section *(i)* at time $t_{[n-1]}$ of time section *[n]* [dimensionless]

$$
= \left(\alpha_{D\langle j+\frac{1}{2}\rangle[n-1]}^{c-s\langle j\rangle s(i)s[n]} \Delta t^{s[n]}\right) \bigg/ \left(\frac{1}{2}\Delta r_{[n-1]}^{c-s\langle j\rangle s(i)s[n]}\right)^2
$$

45

$$R_{sub\langle j+1/2\rangle[n-1]}^{c-s\langle j\rangle s(i)s[n]} = \text{dimensionless number} = \left(\frac{\Delta r_{[n-1]}^{c-s\langle j\rangle s(i)s[n]}}{2}\right) \Bigg/ \left(2 r_{\langle j+1/2\rangle[n-1]}^{c-s(i)s[n]}\right)$$

$W_{[n-1]}^{c-s\langle j\rangle s(i)s[n]}$ = ratio of the conductive heat transfer coefficient of radial section $<j-$

$1>$ to the conductive heat transfer coefficient of radial section $<j>$

in axial section *(i)* at time $t_{[n-1]}$ of time section *[n]*

$$= \left(\frac{k_{[n-1]}^{c-s\langle j-1\rangle s(i)s[n]}}{\Delta r_{[n-1]}^{c-s\langle j-1\rangle s(i)s[n]}}\right) \Bigg/ \left(\frac{k_{[n-1]}^{c-s\langle j\rangle s(i)s[n]}}{\Delta r_{[n-1]}^{c-s\langle j\rangle s(i)s[n]}}\right)$$

radial section $<c>$ = the outermost radial section of the cladding

radial section $<g>$ = the outermost radial section of the gap[7]

$T_{\langle g\rangle[n-1]}^{g-s(i)s[n]}$ = gap temperature at radial sub-node $r_{\langle g\rangle[n-1]}^{g-s(i)s[n]}$ in axial section *(i)* at time

$t_{[n-1]}$ of time section *[n]* [K].

The number of equations contained in the simultaneous linear system is $2c$ where

c is the number of radial sections of axial section *(i)*. These equations have been

established at the radial sub-nodes in each radial section shown in Figure 2.9 because the

high order one-way finite difference method was introduced into the left-hand side of the

Neumann boundary condition of each radial section. The high order one-way finite

difference method generally entails sub-nodes and variables at the sub-nodes. To obtain

the cladding temperatures in axial section *(i)* at time $t_{[n]}$ of time section *[n]*, the

simultaneous linear system should be integrated with the simultaneous linear systems for

---

[7]The gap employs a mesh system for space and time in the transient case, so it has nodes and variables
defined at the nodes.

the fuel temperatures and the gap temperatures in axial section *(i)* at time $t_{[n]}$ of time section *[n]* as well as Equation 2.14. The coefficient matrix of a merged simultaneous linear system can be handled by the Gaussian elimination method[8] or the successive over-relaxation (SOR) method[9].
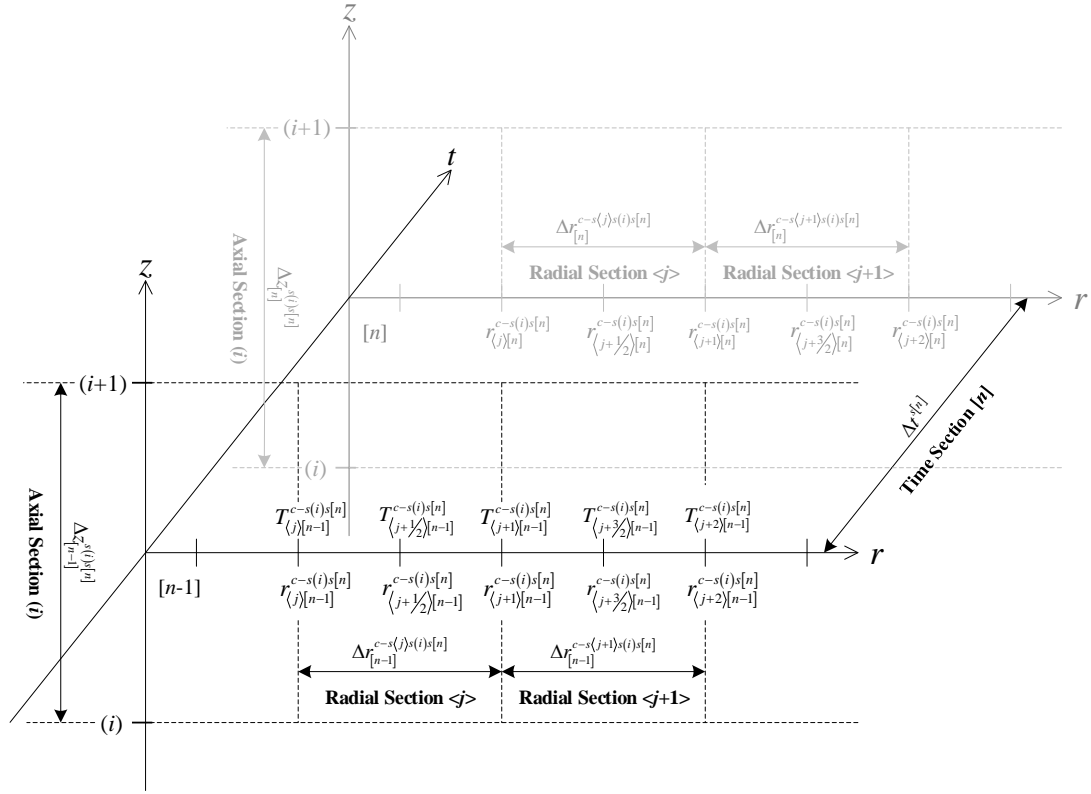
Figure 2.9. Stencil for the modified Crank-Nicolson method. It shows the radial sub-nodes in each radial section of axial section *(i)* for time section *[n]*.

---

[8]This method involves a back substitution algorithm, which is the difference between Gauss elimination and Gauss-Jordan elimination. Also, the Gaussian elimination method requires additional procedures for pivoting and scaling to decrease its propagated round-off error.

[9]The SOR method generally has a higher convergence speed than the Gauss-Seidel method. Also, the SOR method is more appropriate for treating the merged coefficient matrix than the Gaussian elimination method because the size of the merged coefficient matrix is relatively large.

2.1.4. Gap Temperature

The temperature of the fuel-cladding gap in steady state is evaluated by a gap conductance model which computes a gap temperature drop:

$$T_{in}^{g-s(i)} - T_{out}^{g-s(i)} = \frac{p^{s(i)}}{2\pi r_m^{g-s(i)} h^{g-s(i)}}$$ (2.36)

where $T_{in}^{g-s(i)}$ = gap inside temperature in axial section *(i)* [K]

$T_{out}^{g-s(i)}$ = gap outside temperature in axial section *(i)* [K] ($T_{out}^{g-s(i)}$ is given from the calculation of the cladding temperature, and is equal to the cladding inside temperature $T_{\langle 1 \rangle}^{c-s(i)}$)

$r_m^{g-s(i)}$ = logarithmic mean radius of the gap in axial section *(i)* [cm]

$$= \frac{r_{out}^{g-s(i)} - r_{in}^{g-s(i)}}{\ln\left(r_{out}^{g-s(i)} / r_{in}^{g-s(i)}\right)}$$

$h^{g-s(i)}$ = the intensive-property representation of the gap conductance in axial section *(i)* [W/cm^2-K].

According to the parallel thermal resistance formula, the gap conductance should be the sum of three components: conductance derived from ① conduction through the sodium bond, ② radiative heat transfer, and ③ conduction through points of contact.

$$h^{g-s(i)} = h_{sodium}^{g-s(i)} + h_{radiation}^{g-s(i)} + h_{contact}^{g-s(i)}$$ (2.37)

Also, if the gap conductance is calculated by any combination of the three components, the arithmetic mean radius should be used for the extensive-property representation instead of the logarithmic mean radius. On the other hand, the sodium has higher thermal

conductivity and density than the common interstitial materials such as helium and argon, and retains the liquid state under the operating condition of SFRs. These characteristics of the sodium make the effect of radiation and thermal contact on the gap conductance relatively small. Therefore, the conductance can be computed only with the component related to the conduction through the sodium bond:

$$h^{g-s(i)} \approx h_{sodium}^{g-s(i)} = \frac{k^{g-s(i)}}{r_{out}^{g-s(i)} - r_{in}^{g-s(i)}} \tag{2.38}$$

Equation 2.38 gives the gap conductance in axial section *(i)*, which is coupled with the logarithmic mean radius of the gap in axial section *(i)*.

In transient state, the sodium can store and exchange thermal energy dynamically because of its high thermal effusivity. Thus, thermal inertia plays an important role in the calculation of the gap temperature. The transient gap temperatures in radial section *<j>* of axial section *(i)* for time section *[n]* are obtained from the following energy balance equation:

$$\frac{\partial T^{g-s\langle j\rangle s(i)s[n]}(r,t)}{\partial t} =$$
$$\frac{k^{g-s\langle j\rangle s(i)s[n]}(t)}{\rho^{g-s\langle j\rangle s(i)s[n]}(r,t)c_p^{g-s\langle j\rangle s(i)s[n]}(r,t)}\frac{1}{r}\frac{\partial}{\partial r}\left(r\frac{\partial T^{g-s\langle j\rangle s(i)s[n]}(r,t)}{\partial r}\right) \tag{2.39}$$

A mesh system for space and time has been introduced into the gap for the transient case as in the cladding. Equation 2.39 considers only the conductive heat transfer through the sodium bond, and is identical with the equation for the transient cladding temperature (Equation 2.26). Therefore, it can be treated in the same way, which was used for the

transient cladding equation, to derive a simultaneous linear system for the gap temperatures in axial section *(i)* at time $t_{[n]}$ of time section *[n]*.

2.1.5. Fuel Slug Temperature

The temperature distributions in the fuel slug region are obtained from an energy balance equation with internal heat sources:

$$\iiint_{\Delta V} \frac{\partial E^f\left(\vec{r},t\right)}{\partial t}\,dV = \iiint_{\Delta V} S^f\left(\vec{r},t\right)dV - \iint_{\Delta S} \vec{e}_n \cdot \vec{q}_{net}^{\prime\prime f}\left(\vec{r},t\right)dS \qquad (2.40)$$

where $E^f\left(\vec{r},t\right)$ = thermal energy of the fuel per unit volume at point $\vec{r}$ in three-
dimensional space at time t [J/cm^3]

$S^f\left(\vec{r},t\right)$ = internal heat sources in the fuel slug region [W/cm^3]

$\vec{e}_n$ = unit vector which is normal to the surface

$\vec{q}_{net}^{\prime\prime f}\left(\vec{r},t\right)$ = net current of heat at point $\vec{r}$ at time t [W/cm^2].

The net current of heat is described by Fourier's law, and Equation 2.40 becomes

$$\iiint_{\Delta V} \rho^f\left(\vec{r},t\right)c_p^f\left(\vec{r},t\right)\frac{\partial T^f\left(\vec{r},t\right)}{\partial t}\,dV =$$
$$\iiint_{\Delta V} q_{gen}^{\prime\prime\prime f}\left(\vec{r},t\right)dV - \iint_{\Delta S} \vec{e}_n \cdot \left[-k^f\left(\vec{r},t\right)\vec{\nabla}T^f\left(\vec{r},t\right)\right]dS \qquad (2.41)$$

where $q_{gen}^{\prime\prime\prime f}\left(\vec{r},t\right)$ = volumetric heat generation rate at point $\vec{r}$ in three-dimensional space
at time t [W/cm^3].

Equation 2.41 is additionally arranged to the following partial differential equation by the Gauss's divergence theorem which converts the spatial-surface integral to the spatial-volume integral:

50

$$\rho^f\left(\vec{r},t\right)c_p^f\left(\vec{r},t\right)\frac{\partial T^f\left(\vec{r},t\right)}{\partial t}=q_{gen}^{\prime\prime\prime f}\left(\vec{r},t\right)-\vec{\nabla}\cdot\left[-k^f\left(\vec{r},t\right)\vec{\nabla}T^f\left(\vec{r},t\right)\right] \qquad (2.42)$$

Steady State

During steady state, the thermal energy of the fuel does not change in time, and the net flow rate of heat is equal to the heat generation rate. Thus, in cylindrical coordinates, Equation 2.42 becomes

$$q_{gen}^{\prime\prime\prime f}\left(r\right)+k^f\frac{1}{r}\frac{d}{dr}\left(r\frac{dT^f\left(r\right)}{dr}\right)=0 \qquad (2.43)$$

Like the steady state equation for the cladding (Equation 2.19), Equation 2.43 is based on the assumption[10] of constant thermal conductivity. The volumetric heat generation rate is also subject to the spatial variation and needs to be constant within a radial interval. Therefore, Equation 2.43 should be established separately for each radial section of an axial section to employ the sectional averages of the volumetric heat generation rate and thermal conductivity. At radial node $r_{<j>}$, the equation established for radial section $<j>$ of axial section *(i)* is approximated by the following finite difference heat conduction equation:

$$\left(1+\frac{\left(\frac{1}{2}\Delta r^{f-s\langle j\rangle s(i)}\right)}{2r_{\langle j\rangle}^{f-s(i)}}\right)T_{\langle j+\frac{1}{2}\rangle}^{f-s\langle j\rangle s(i)}-2T_{\langle j\rangle}^{f-s\langle j\rangle s(i)}+\left(1-\frac{\left(\frac{1}{2}\Delta r^{f-s\langle j\rangle s(i)}\right)}{2r_{\langle j\rangle}^{f-s(i)}}\right)T_{\langle j-\frac{1}{2}\rangle}^{f-s\langle j\rangle s(i)}$$
$$=-\frac{q_{gen}^{\prime\prime\prime f-s\langle j\rangle s(i)}}{k^{f-s\langle j\rangle s(i)}}\left(\frac{1}{2}\Delta r^{f-s\langle j\rangle s(i)}\right)^2 \qquad (2.44)$$

---

[10]In addition to the assumption of constant thermal conductivity, heat conduction in the axial and azimuthal directions is considered negligible relative to radial heat conduction and has been ignored in Equation 2.43 as in the equation for the cladding temperature.

where $T^{f-s\langle j\rangle s(i)}_{\langle j+\frac{1}{2}\rangle}$ = fuel temperature at radial sub-node $r^{f-s(i)}_{\langle j+\frac{1}{2}\rangle}$ in radial section $<j>$ of axial

section *(i)* [K]

$q^{'''\,f-s\langle j\rangle s(i)}_{gen}$ = average volumetric heat generation rate in radial section $<j>$ of axial

section *(i)* [W/cm^3]

$k^{f-s\langle j\rangle s(i)}$ = average thermal conductivity of the fuel in radial section $<j>$ of axial

section *(i)* [W/cm-K].

Equation 2.44 contains virtual variable $T^{f-s\langle j\rangle s(i)}_{\langle j-\frac{1}{2}\rangle}$ defined at ghost node

$r^{f-s(i)}_{\langle j\rangle} - \dfrac{1}{2}\Delta r^{f-s\langle j\rangle s(i)}$. As explained in the calculation of the cladding temperature, the

virtual variable $T^{f-s\langle j\rangle s(i)}_{\langle j-\frac{1}{2}\rangle}$ is eliminated by the boundary conditions for radial section $<j>$

of axial section *(i)*:

$$q^{''\,f-s\langle j-1\rangle s(i)}_{\langle j\rangle} = q^{''\,f-s\langle j\rangle s(i)}_{\langle j\rangle} \qquad (2.45)$$

$$T^{f-s\langle j\rangle s(i)}_{\langle j+1\rangle} = T^{f-s\langle j+1\rangle s(i)}_{\langle j+1\rangle} \qquad (2.46)$$

These boundary conditions can be employed for each radial section of axial section *(i)* and

be applied to the finite difference heat conduction equations of each radial section for

eliminating virtual variables. However, the finite difference heat conduction equation at

the first radial node[11] has a singularity, which requires the Neumann boundary condition[12]

of the first radial section to be treated with the three-point forward difference

---

[11]The first radial node $r_{<1>}$ is zero when no central void is developed.

[12]The Neumann boundary condition of the first radial section is $q^{''\,f-s\langle 1\rangle s(i)}_{\langle 1\rangle} = 0$.

formula. The three-point forward difference formula generally entails sub-nodes and variables at the sub-nodes. Thus, the finite difference heat conduction equations for the first radial section are derived at the radial sub-nodes in the first radial section. The derivation of equations at sub-nodes is also implemented in the other radial sections for compatibility and enhanced accuracy (Equation 2.44 has also been derived at a radial sub-node).

Combining the finite difference heat conduction equations with the boundary conditions for all the radial sections of axial section *(i)* yield a simultaneous linear system for axial section *(i)*:

First radial section (radial section *<1>*)

$$T_{\langle 1.5 \rangle}^{f-s(i)} - T_{\langle 2 \rangle}^{f-s(i)} = \frac{3}{2\left(1 + 2R_{\langle 1.5 \rangle}^{f-s\langle 1 \rangle s(i)}\right)} \frac{q_{gen}'''^{f-s\langle 1 \rangle s(i)}}{k^{f-s\langle 1 \rangle s(i)}} \left(\frac{\Delta r^{f-s\langle 1 \rangle s(i)}}{2}\right)^2 \tag{2.47}$$

Last radial section (radial section *<f>*)

$$
\frac{k^{f-s\langle f-1 \rangle s(i)}}{\Delta r^{f-s\langle f-1 \rangle s(i)}\left(1 + R_{\langle f \rangle}^{f-s\langle f-1 \rangle s(i)}\right)} T_{\langle f-\frac{1}{2} \rangle}^{f-s(i)}
$$

$$
-\left(\frac{k^{f-s\langle f-1 \rangle s(i)}}{\Delta r^{f-s\langle f-1 \rangle s(i)}\left(1 + R_{\langle f \rangle}^{f-s\langle f-1 \rangle s(i)}\right)} + \frac{k^{f-s\langle f \rangle s(i)}}{\Delta r^{f-s\langle f \rangle s(i)}\left(1 - R_{\langle f \rangle}^{f-s\langle f \rangle s(i)}\right)}\right) T_{\langle f \rangle}^{f-s(i)}
$$

$$
+ \frac{k^{f-s\langle f \rangle s(i)}}{\Delta r^{f-s\langle f \rangle s(i)}\left(1 - R_{\langle f \rangle}^{f-s\langle f \rangle s(i)}\right)} T_{\langle f+\frac{1}{2} \rangle}^{f-s(i)}
$$

$$
= -\frac{q_{gen}'''^{f-s\langle f-1 \rangle s(i)} \Delta r^{f-s\langle f-1 \rangle s(i)}}{8\left(1 + R_{\langle f \rangle}^{f-s\langle f-1 \rangle s(i)}\right)} - \frac{q_{gen}'''^{f-s\langle f \rangle s(i)} \Delta r^{f-s\langle f \rangle s(i)}}{8\left(1 - R_{\langle f \rangle}^{f-s\langle f \rangle s(i)}\right)}
$$

$$\tag{2.48}$$

at radial sub-node $r_{\langle f \rangle}^{f-s(i)}$, and

$$\left(1 - R^{f-s\langle f\rangle s(i)}_{\langle f+\frac{1}{2}\rangle}\right)T^{f-s(i)}_{\langle f\rangle} - 2T^{f-s(i)}_{\langle f+\frac{1}{2}\rangle} =$$

$$-\left(1 + R^{f-s\langle f\rangle s(i)}_{\langle f+\frac{1}{2}\rangle}\right)T^{f-s(i)}_{out} - \frac{q'''^{f-s\langle f\rangle s(i)}_{gen}}{k^{f-s\langle f\rangle s(i)}}\left(\frac{\Delta r^{f-s\langle f\rangle s(i)}}{2}\right)^2 \qquad (2.49)$$

at radial sub-node $r^{f-s(i)}_{\langle f+\frac{1}{2}\rangle}$

The others (arbitrary radial section $<j>$, $1 < j < f$)

$$\frac{k^{f-s\langle j-1\rangle s(i)}}{\Delta r^{f-s\langle j-1\rangle s(i)}\left(1 + R^{f-s\langle j-1\rangle s(i)}_{\langle j\rangle}\right)}T^{f-s(i)}_{\langle j-\frac{1}{2}\rangle}$$

$$-\left(\frac{k^{f-s\langle j-1\rangle s(i)}}{\Delta r^{f-s\langle j-1\rangle s(i)}\left(1 + R^{f-s\langle j-1\rangle s(i)}_{\langle j\rangle}\right)} + \frac{k^{f-s\langle j\rangle s(i)}}{\Delta r^{f-s\langle j\rangle s(i)}\left(1 - R^{f-s\langle j\rangle s(i)}_{\langle j\rangle}\right)}\right)T^{f-s(i)}_{\langle j\rangle}$$

$$+ \frac{k^{f-s\langle j\rangle s(i)}}{\Delta r^{f-s\langle j\rangle s(i)}\left(1 - R^{f-s\langle j\rangle s(i)}_{\langle j\rangle}\right)}T^{f-s(i)}_{\langle j+\frac{1}{2}\rangle} \qquad (2.50)$$

$$= -\frac{q'''^{f-s\langle j-1\rangle s(i)}_{gen}\Delta r^{f-s\langle j-1\rangle s(i)}}{8\left(1 + R^{f-s\langle j-1\rangle s(i)}_{\langle j\rangle}\right)} - \frac{q'''^{f-s\langle j\rangle s(i)}_{gen}\Delta r^{f-s\langle j\rangle s(i)}}{8\left(1 - R^{f-s\langle j\rangle s(i)}_{\langle j\rangle}\right)}$$

at radial sub-node $r^{f-s(i)}_{\langle j\rangle}$, and

$$\left(1 - R^{f-s\langle j\rangle s(i)}_{\langle j+\frac{1}{2}\rangle}\right)T^{f-s(i)}_{\langle j\rangle} - 2T^{f-s(i)}_{\langle j+\frac{1}{2}\rangle} - \left(1 + R^{f-s\langle j\rangle s(i)}_{\langle j+\frac{1}{2}\rangle}\right)T^{f-s(i)}_{\langle j+1\rangle}$$

$$= -\frac{q'''^{f-s\langle j\rangle s(i)}_{gen}}{k^{f-s\langle j\rangle s(i)}}\left(\frac{\Delta r^{f-s\langle j\rangle s(i)}}{2}\right)^2 \qquad (2.51)$$

at radial sub-node $r^{f-s(i)}_{\langle j+\frac{1}{2}\rangle}$

where $R^{f-s\langle j-1\rangle s(i)}_{\langle j\rangle} = $ dimensionless number $= \dfrac{\left(\frac{1}{2}\Delta r^{f-s\langle j-1\rangle s(i)}\right)}{2r^{f-s(i)}_{\langle j\rangle}}$

$\Delta r^{f-s\langle j\rangle s(i)} = $ size of radial section $<j>$ of the fuel slug in axial section (i) [cm]

54

$$= r_{\langle j+1 \rangle}^{f-s(i)} - r_{\langle j \rangle}^{f-s(i)}$$

$T_{out}^{f-s(i)}$ = fuel outside temperature in axial section *(i)* [K] ($T_{out}^{f-s(i)}$ is given from the calculation of the gap temperature, and is equal to the gap inside temperature $T_{in}^{g-s(i)}$).

    The number of equations contained in the simultaneous linear system is 2*f*–1 where *f* is the number of radial sections of axial section *(i)* in the fuel slug region. These equations are fully compatible with the adaptable mesh system mentioned previously, and well accommodate the spatial dependence of the volumetric heat generation rate and material properties. The coefficient matrix of the simultaneous linear system has the form of a tridiagonal matrix, so TDMA can be used to find out the fuel temperatures in axial section *(i)*. The fuel temperature at the first radial node is calculated from the following relation once the fuel temperatures at the other radial nodes are determined by the tridiagonal matrix algorithm:

$$T_{\langle 1 \rangle}^{f-s(i)} = \frac{4 T_{\langle 1.5 \rangle}^{f-s(i)} - T_{\langle 2 \rangle}^{f-s(i)}}{3} \tag{2.52}$$

Similar simultaneous linear systems are given to other axial sections and can be treated in the same way. Figure 2.10 shows a fuel temperature distribution computed by the TAMU-ZFP code. The result of the code calculation has been compared with the analytical solution in Figure 2.11, and they are well matched to each other at all of the axial sections. The analytical solution used in the comparison is represented in APPENDIX A.
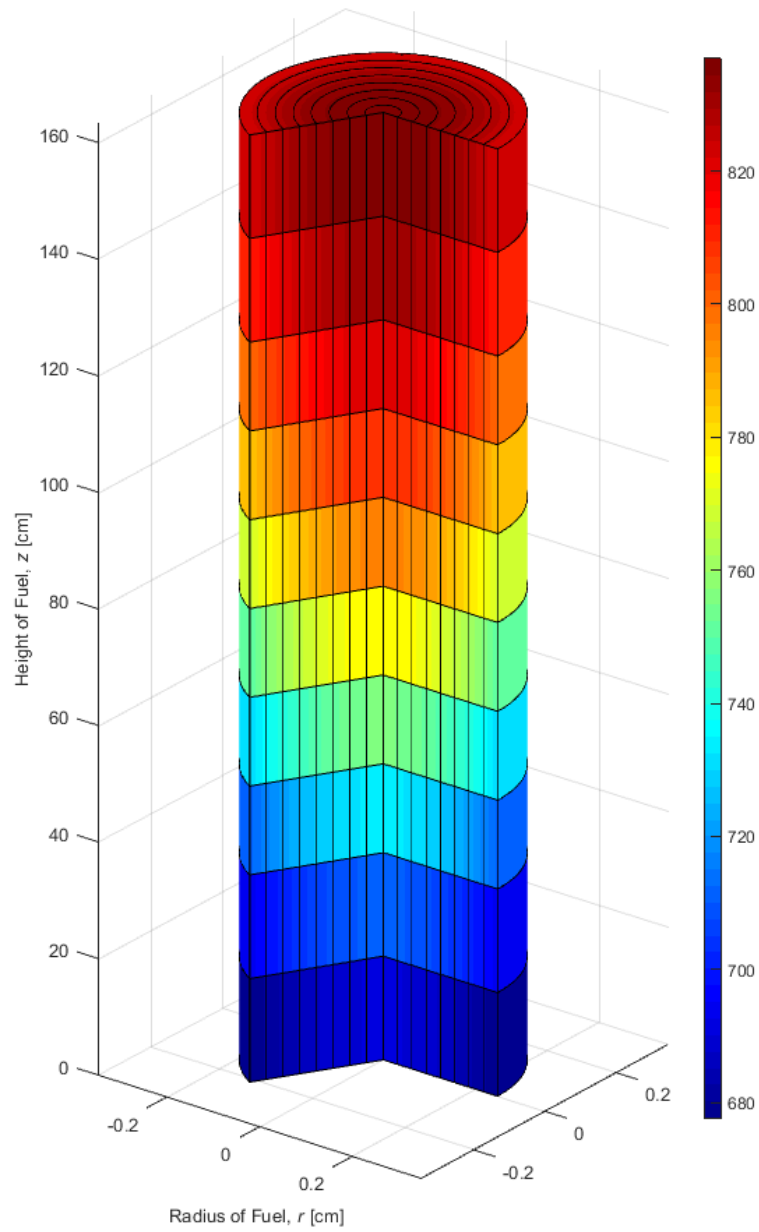
Figure 2.10. Fuel temperature distribution computed by the TAMU-ZFP code. The pin-average LHGR used in the calculation is 117.1 W/cm.
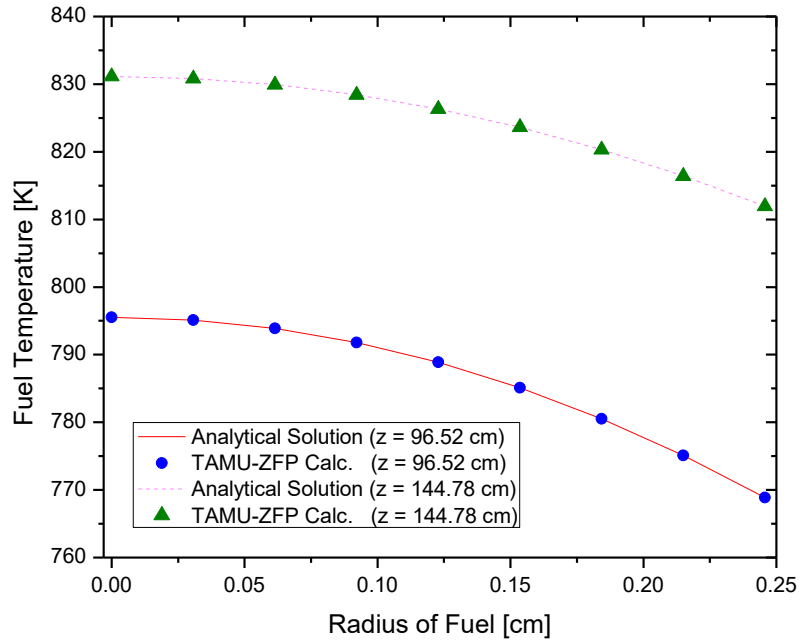
Figure 2.11. Comparison of the computed fuel temperature with the analytical solution.

Transient State

In transient state, the net flow rate of heat is not balanced with the heat generation rate, and the imbalance between them induces the change of the fuel thermal energy with time. Thus, Equation 2.42 should be handled in the full form of a parabolic partial differential equation. Applying Equation 2.42 to radial section *<j>* of axial section *(i)* for time section *[n]* yields

$$
\begin{aligned}
\frac{\partial T^{f-s\langle j\rangle s(i)s[n]}(r,t)}{\partial t} &= \frac{q_{gen}'''^{\,f-s\langle j\rangle s(i)s[n]}(t)}{\rho^{f-s\langle j\rangle s(i)s[n]}(r,t)\,c_{p}^{f-s\langle j\rangle s(i)s[n]}(r,t)} \\
&+ \frac{k^{f-s\langle j\rangle s(i)s[n]}(t)}{\rho^{f-s\langle j\rangle s(i)s[n]}(r,t)\,c_{p}^{f-s\langle j\rangle s(i)s[n]}(r,t)}\frac{1}{r}\frac{\partial}{\partial r}\left(r\frac{\partial T^{f-s\langle j\rangle s(i)s[n]}(r,t)}{\partial r}\right)
\end{aligned} \tag{2.53}
$$

57

where $\rho^{f-s\langle j\rangle s(i)s[n]}(r,t)$ = density of the fuel at radius r in radial section $\langle j\rangle$ of axial

section (i) at time t of time section $[n]$ [g/cm^3]

$c_p^{f-s\langle j\rangle s(i)s[n]}(r,t)$ = heat capacity of the fuel at radius r in radial section $\langle j\rangle$ of axial

section (i) at time t of time section $[n]$ [J/g-K].

Like the steady state equation, Equation 2.53 is based on the assumption that the volumetric heat generation rate and thermal conductivity are not functions of r within a radial section. At radial sub-node $r_{\langle j\rangle}$, the equation can be approximated to the following finite difference heat conduction equation by the modified Crank-Nicolson method which was used for the transient cladding equation:

$$
\begin{aligned}
V_{D\langle j\rangle[n]}^{f-s\langle j\rangle s(i)s[n]} &\left(1 + R_{\langle j\rangle[n]}^{f-s\langle j\rangle s(i)s[n]}\right) T_{\langle j+\frac{1}{2}\rangle[n]}^{f-s\langle j\rangle s(i)s[n]} \\
&- 2\left(1 + V_{D\langle j\rangle[n]}^{f-s\langle j\rangle s(i)s[n]}\right) T_{\langle j\rangle[n]}^{f-s\langle j\rangle s(i)s[n]} + V_{D\langle j\rangle[n]}^{f-s\langle j\rangle s(i)s[n]}\left(1 - R_{\langle j\rangle[n]}^{f-s\langle j\rangle s(i)s[n]}\right) T_{\langle j-\frac{1}{2}\rangle[n]}^{f-s\langle j\rangle s(i)s[n]} \\
= &-V_{D\langle j\rangle[n-1]}^{f-s\langle j\rangle s(i)s[n]}\left(1 + R_{\langle j\rangle[n-1]}^{f-s\langle j\rangle s(i)s[n]}\right) T_{\langle j+\frac{1}{2}\rangle[n-1]}^{f-s\langle j\rangle s(i)s[n]} \qquad (2.54) \\
&- 2\left(1 - V_{D\langle j\rangle[n-1]}^{f-s\langle j\rangle s(i)s[n]}\right) T_{\langle j\rangle[n-1]}^{f-s\langle j\rangle s(i)s[n]} - V_{D\langle j\rangle[n-1]}^{f-s\langle j\rangle s(i)s[n]}\left(1 - R_{\langle j\rangle[n-1]}^{f-s\langle j\rangle s(i)s[n]}\right) T_{\langle j-\frac{1}{2}\rangle[n-1]}^{f-s\langle j\rangle s(i)s[n]} \\
&- Q_{T\langle j\rangle[n-1]}^{f-s\langle j\rangle s(i)s[n]} - Q_{T\langle j\rangle[n]}^{f-s\langle j\rangle s(i)s[n]}
\end{aligned}
$$

where $V_{D\langle j\rangle[n-1]}^{f-s\langle j\rangle s(i)s[n]}$ = diffusion number at radial sub-node $r_{\langle j\rangle[n-1]}^{f-s(i)s[n]}$ in radial section $\langle j\rangle$

of axial section (i) at time $t_{[n-1]}$ of time section $[n]$ [dimensionless]

$$
= \frac{\alpha_{D\langle j\rangle[n-1]}^{f-s\langle j\rangle s(i)s[n]} \Delta t^{s[n]}}{\left(\dfrac{1}{2}\Delta r_{[n-1]}^{f-s\langle j\rangle s(i)s[n]}\right)^2}
$$

$\alpha_{D\langle j\rangle[n-1]}^{f-s\langle j\rangle s(i)s[n]}$ = thermal diffusivity at radial sub-node $r_{\langle j\rangle[n-1]}^{f-s(i)s[n]}$ in radial section $\langle j\rangle$

of axial section (i) at time $t_{[n-1]}$ of time section $[n]$ [cm^2/s]

58

$$= \frac{k_{[n-1]}^{f-s\langle j\rangle s(i)s[n]}}{\rho_{\langle j\rangle[n-1]}^{f-s\langle j\rangle s(i)s[n]} c_{p\langle j\rangle[n-1]}^{f-s\langle j\rangle s(i)s[n]}}$$

$R_{\langle j\rangle[n-1]}^{f-s\langle j\rangle s(i)s[n]}$ = dimensionless number = $\dfrac{\left(\dfrac{\Delta r_{[n-1]}^{f-s\langle j\rangle s(i)s[n]}}{2}\right)}{2 r_{\langle j\rangle[n-1]}^{f-s(i)s[n]}}$

$Q_{T\langle j\rangle[n-1]}^{f-s\langle j\rangle s(i)s[n]}$ = fuel temperature increase at radial sub-node $r_{\langle j\rangle[n-1]}^{f-s(i)s[n]}$ in radial

section *<j>* of axial section *(i)* for time section *[n]* by the internal

heat source at time $t_{[n-1]}$ of time section *[n]* [K] = $q_{T\langle j\rangle[n-1]}^{f-s\langle j\rangle s(i)s[n]} \Delta t^{s[n]}$

$q_{T\langle j\rangle[n-1]}^{f-s\langle j\rangle s(i)s[n]}$ = fuel temperature increase rate at radial sub-node $r_{\langle j\rangle[n-1]}^{f-s(i)s[n]}$ in radial

section *<j>* of axial section *(i)* by the internal heat source at time

$t_{[n-1]}$ of time section *[n]* [K/s] = $\dfrac{q_{gen[n-1]}^{m\,f-s\langle j\rangle s(i)s[n]}}{\rho_{\langle j\rangle[n-1]}^{f-s\langle j\rangle s(i)s[n]} c_{p\langle j\rangle[n-1]}^{f-s\langle j\rangle s(i)s[n]}}$.

Equation 2.54 contains virtual variables $T_{\langle j-\frac{1}{2}\rangle[n]}^{f-s\langle j\rangle s(i)s[n]}$ and $T_{\langle j-\frac{1}{2}\rangle[n-1]}^{f-s\langle j\rangle s(i)s[n]}$ defined at

ghost nodes $r_{\langle j\rangle[n]}^{f-s(i)s[n]} - \left(\Delta r_{[n]}^{f-s\langle j\rangle s(i)s[n]} / 2\right)$ and $r_{\langle j\rangle[n-1]}^{f-s(i)s[n]} - \left(\Delta r_{[n-1]}^{f-s\langle j\rangle s(i)s[n]} / 2\right)$, respectively.

As explained in the calculation of the transient cladding temperature, the virtual variables

in the finite difference heat conduction equation derived with the modified Crank-

Nicolson method can be removed by applying related boundary conditions. Therefore,

$T_{\langle j-\frac{1}{2}\rangle[n]}^{f-s\langle j\rangle s(i)s[n]}$ and $T_{\langle j-\frac{1}{2}\rangle[n-1]}^{f-s\langle j\rangle s(i)s[n]}$ are eliminated by the boundary conditions for radial section

<j> of axial section *(i)* for time section *[n]*:

$$q''^{f-s\langle j-1\rangle s(i)s[n]}_{\langle j\rangle[n-1]} = q''^{f-s\langle j\rangle s(i)s[n]}_{\langle j\rangle[n-1]} \qquad (2.55)$$

$$T^{f-s\langle j\rangle s(i)s[n]}_{\langle j+1\rangle[n-1]} = T^{f-s\langle j+1\rangle s(i)s[n]}_{\langle j+1\rangle[n-1]} \qquad (2.56)$$

at time $t_{[n-1]}$ of time section *[n]*, and

$$q''^{f-s\langle j-1\rangle s(i)s[n]}_{\langle j\rangle[n]} = q''^{f-s\langle j\rangle s(i)s[n]}_{\langle j\rangle[n]} \qquad (2.57)$$

$$T^{f-s\langle j\rangle s(i)s[n]}_{\langle j+1\rangle[n]} = T^{f-s\langle j+1\rangle s(i)s[n]}_{\langle j+1\rangle[n]} \qquad (2.58)$$

at time $t_{[n]}$ of time section *[n]*.

When these boundary conditions are employed for each radial section of axial section *(i)* and applied to the finite difference heat conduction equations of each radial section for eliminating virtual variables, a simultaneous linear system is obtained for axial section *(i)* at time $t_{[n]}$ of time section *[n]*:

First radial section (radial section *<1>*)

$$3T^{f-s(i)s[n]}_{\langle 1\rangle[n]} - 4T^{f-s(i)s[n]}_{\langle 1.5\rangle[n]} + T^{f-s(i)s[n]}_{\langle 2\rangle[n]} = 0 \qquad (2.59)$$

at radial sub-node $r^{f-s(i)s[n]}_{\langle 1\rangle\left[n-\frac{1}{2}\right]}$, and

$$
\begin{aligned}
&V^{f-s\langle 1\rangle s(i)s[n]}_{D\langle 1.5\rangle[n]}\left(1-R^{f-s\langle 1\rangle s(i)s[n]}_{\langle 1.5\rangle[n]}\right)T^{f-s(i)s[n]}_{\langle 1\rangle[n]} \\
&\quad -2\left(1+V^{f-s\langle 1\rangle s(i)s[n]}_{D\langle 1.5\rangle[n]}\right)T^{f-s(i)s[n]}_{\langle 1.5\rangle[n]} + V^{f-s\langle 1\rangle s(i)s[n]}_{D\langle 1.5\rangle[n]}\left(1+R^{f-s\langle 1\rangle s(i)s[n]}_{\langle 1.5\rangle[n]}\right)T^{f-s(i)s[n]}_{\langle 2\rangle[n]} \\
&= -V^{f-s\langle 1\rangle s(i)s[n]}_{D\langle 1.5\rangle[n-1]}\left(1-R^{f-s\langle 1\rangle s(i)s[n]}_{\langle 1.5\rangle[n-1]}\right)T^{f-s(i)s[n]}_{\langle 1\rangle[n-1]} \\
&\quad -2\left(1-V^{f-s\langle 1\rangle s(i)s[n]}_{D\langle 1.5\rangle[n-1]}\right)T^{f-s(i)s[n]}_{\langle 1.5\rangle[n-1]} - V^{f-s\langle 1\rangle s(i)s[n]}_{D\langle 1.5\rangle[n-1]}\left(1+R^{f-s\langle 1\rangle s(i)s[n]}_{\langle 1.5\rangle[n-1]}\right)T^{f-s(i)s[n]}_{\langle 2\rangle[n-1]} \\
&\qquad\qquad\qquad\qquad\qquad -Q^{f-s\langle 1\rangle s(i)s[n]}_{T\langle 1.5\rangle[n-1]} - Q^{f-s\langle 1\rangle s(i)s[n]}_{T\langle 1.5\rangle[n]}
\end{aligned}
\qquad (2.60)
$$

at radial sub-node $r^{f-s(i)s[n]}_{\langle 1.5\rangle\left[n-\frac{1}{2}\right]}$

60

Last radial section (radial section <f>)

$$V_{D\langle f\rangle[n]}^{f-s\langle f\rangle s(i)s[n]}\left(1-R_{\langle f\rangle[n]}^{f-s\langle f\rangle s(i)s[n]}\right)W_{[n]}^{f-s\langle f\rangle s(i)s[n]}T_{\langle f-1\rangle[n]}^{f-s(i)s[n]}$$

$$-4V_{D\langle f\rangle[n]}^{f-s\langle f\rangle s(i)s[n]}\left(1-R_{\langle f\rangle[n]}^{f-s\langle f\rangle s(i)s[n]}\right)W_{[n]}^{f-s\langle f\rangle s(i)s[n]}T_{\langle f-\frac{1}{2}\rangle[n]}^{f-s(i)s[n]}$$

$$+\left[3V_{D\langle f\rangle[n]}^{f-s\langle f\rangle s(i)s[n]}\left(1-R_{\langle f\rangle[n]}^{f-s\langle f\rangle s(i)s[n]}\right)W_{[n]}^{f-s\langle f\rangle s(i)s[n]}+2\left(1+V_{D\langle f\rangle[n]}^{f-s\langle f\rangle s(i)s[n]}\right)\right]T_{\langle f\rangle[n]}^{f-s(i)s[n]}$$

$$-2V_{D\langle f\rangle[n]}^{f-s\langle f\rangle s(i)s[n]}T_{\langle f+\frac{1}{2}\rangle[n]}^{f-s(i)s[n]}$$

$$=-V_{D\langle f\rangle[n-1]}^{f-s\langle f\rangle s(i)s[n]}\left(1-R_{\langle f\rangle[n-1]}^{f-s\langle f\rangle s(i)s[n]}\right)W_{[n-1]}^{f-s\langle f\rangle s(i)s[n]}T_{\langle f-1\rangle[n-1]}^{f-s(i)s[n]} \quad (2.61)$$

$$+4V_{D\langle f\rangle[n-1]}^{f-s\langle f\rangle s(i)s[n]}\left(1-R_{\langle f\rangle[n-1]}^{f-s\langle f\rangle s(i)s[n]}\right)W_{[n-1]}^{f-s\langle f\rangle s(i)s[n]}T_{\langle f-\frac{1}{2}\rangle[n-1]}^{f-s(i)s[n]}$$

$$-\left[3V_{D\langle f\rangle[n-1]}^{f-s\langle f\rangle s(i)s[n]}\left(1-R_{\langle f\rangle[n-1]}^{f-s\langle f\rangle s(i)s[n]}\right)W_{[n-1]}^{f-s\langle f\rangle s(i)s[n]}-2\left(1-V_{D\langle f\rangle[n-1]}^{f-s\langle f\rangle s(i)s[n]}\right)\right]T_{\langle f\rangle[n-1]}^{f-s(i)s[n]}$$

$$+2V_{D\langle f\rangle[n-1]}^{f-s\langle f\rangle s(i)s[n]}T_{\langle f+\frac{1}{2}\rangle[n-1]}^{f-s(i)s[n]}+Q_{T\langle f\rangle[n-1]}^{f-s\langle f\rangle s(i)s[n]}+Q_{T\langle f\rangle[n]}^{f-s\langle f\rangle s(i)s[n]}$$

at radial sub-node $r_{\langle f\rangle\left[n-\frac{1}{2}\right]}^{f-s(i)s[n]}$, and

$$V_{D\langle f+\frac{1}{2}\rangle[n]}^{f-s\langle f\rangle s(i)s[n]}\left(1-R_{\langle f+\frac{1}{2}\rangle[n]}^{f-s\langle f\rangle s(i)s[n]}\right)T_{\langle f\rangle[n]}^{f-s(i)s[n]}$$

$$-2\left(1+V_{D\langle f+\frac{1}{2}\rangle[n]}^{f-s\langle f\rangle s(i)s[n]}\right)T_{\langle f+\frac{1}{2}\rangle[n]}^{f-s(i)s[n]}+V_{D\langle f+\frac{1}{2}\rangle[n]}^{f-s\langle f\rangle s(i)s[n]}\left(1+R_{\langle f+\frac{1}{2}\rangle[n]}^{f-s\langle f\rangle s(i)s[n]}\right)T_{\langle 1\rangle[n]}^{g-s(i)s[n]}$$

$$=-V_{D\langle f+\frac{1}{2}\rangle[n-1]}^{f-s\langle f\rangle s(i)s[n]}\left(1-R_{\langle f+\frac{1}{2}\rangle[n-1]}^{f-s\langle f\rangle s(i)s[n]}\right)T_{\langle f\rangle[n-1]}^{f-s(i)s[n]} \quad (2.62)$$

$$-2\left(1-V_{D\langle f+\frac{1}{2}\rangle[n-1]}^{f-s\langle f\rangle s(i)s[n]}\right)T_{\langle f+\frac{1}{2}\rangle[n-1]}^{f-s(i)s[n]}-V_{D\langle f+\frac{1}{2}\rangle[n-1]}^{f-s\langle f\rangle s(i)s[n]}\left(1+R_{\langle f+\frac{1}{2}\rangle[n-1]}^{f-s\langle f\rangle s(i)s[n]}\right)T_{\langle 1\rangle[n-1]}^{g-s(i)s[n]}$$

$$-Q_{T\langle f+\frac{1}{2}\rangle[n-1]}^{f-s\langle f\rangle s(i)s[n]}-Q_{T\langle f+\frac{1}{2}\rangle[n]}^{f-s\langle f\rangle s(i)s[n]}$$

at radial sub-node $r_{\langle f+\frac{1}{2}\rangle\left[n-\frac{1}{2}\right]}^{f-s(i)s[n]}$

The others (arbitrary radial section $<j>$, $1 < j < f$)

$$V_{D\langle j\rangle[n]}^{f-s\langle j\rangle s(i)s[n]}\left(1-R_{\langle j\rangle[n]}^{f-s\langle j\rangle s(i)s[n]}\right)W_{[n]}^{f-s\langle j\rangle s(i)s[n]}T_{\langle j-1\rangle[n]}^{f-s(i)s[n]}$$

$$-4V_{D\langle j\rangle[n]}^{f-s\langle j\rangle s(i)s[n]}\left(1-R_{\langle j\rangle[n]}^{f-s\langle j\rangle s(i)s[n]}\right)W_{[n]}^{f-s\langle j\rangle s(i)s[n]}T_{\langle j-\frac{1}{2}\rangle[n]}^{f-s(i)s[n]}$$

$$+\left[3V_{D\langle j\rangle[n]}^{f-s\langle j\rangle s(i)s[n]}\left(1-R_{\langle j\rangle[n]}^{f-s\langle j\rangle s(i)s[n]}\right)W_{[n]}^{f-s\langle j\rangle s(i)s[n]}+2\left(1+V_{D\langle j\rangle[n]}^{f-s\langle j\rangle s(i)s[n]}\right)\right]T_{\langle j\rangle[n]}^{f-s(i)s[n]}$$

$$-2V_{D\langle j\rangle[n]}^{f-s\langle j\rangle s(i)s[n]}T_{\langle j+\frac{1}{2}\rangle[n]}^{f-s(i)s[n]}$$

$$=-V_{D\langle j\rangle[n-1]}^{f-s\langle j\rangle s(i)s[n]}\left(1-R_{\langle j\rangle[n-1]}^{f-s\langle j\rangle s(i)s[n]}\right)W_{[n-1]}^{f-s\langle j\rangle s(i)s[n]}T_{\langle j-1\rangle[n-1]}^{f-s(i)s[n]}$$

$$+4V_{D\langle j\rangle[n-1]}^{f-s\langle j\rangle s(i)s[n]}\left(1-R_{\langle j\rangle[n-1]}^{f-s\langle j\rangle s(i)s[n]}\right)W_{[n-1]}^{f-s\langle j\rangle s(i)s[n]}T_{\langle j-\frac{1}{2}\rangle[n-1]}^{f-s(i)s[n]}$$

$$-\left[3V_{D\langle j\rangle[n-1]}^{f-s\langle j\rangle s(i)s[n]}\left(1-R_{\langle j\rangle[n-1]}^{f-s\langle j\rangle s(i)s[n]}\right)W_{[n-1]}^{f-s\langle j\rangle s(i)s[n]}-2\left(1-V_{D\langle j\rangle[n-1]}^{f-s\langle j\rangle s(i)s[n]}\right)\right]T_{\langle j\rangle[n-1]}^{f-s(i)s[n]}$$

$$+2V_{D\langle j\rangle[n-1]}^{f-s\langle j\rangle s(i)s[n]}T_{\langle j+\frac{1}{2}\rangle[n-1]}^{f-s(i)s[n]}+Q_{T\langle j\rangle[n-1]}^{f-s\langle j\rangle s(i)s[n]}+Q_{T\langle j\rangle[n]}^{f-s\langle j\rangle s(i)s[n]} \quad (2.63)$$

at radial sub-node $r_{\langle j\rangle\left[n-\frac{1}{2}\right]}^{f-s(i)s[n]}$, and

$$V_{D\langle j+\frac{1}{2}\rangle[n]}^{f-s\langle j\rangle s(i)s[n]}\left(1-R_{\langle j+\frac{1}{2}\rangle[n]}^{f-s\langle j\rangle s(i)s[n]}\right)T_{\langle j\rangle[n]}^{f-s(i)s[n]}$$

$$-2\left(1+V_{D\langle j+\frac{1}{2}\rangle[n]}^{f-s\langle j\rangle s(i)s[n]}\right)T_{\langle j+\frac{1}{2}\rangle[n]}^{f-s(i)s[n]}+V_{D\langle j+\frac{1}{2}\rangle[n]}^{f-s\langle j\rangle s(i)s[n]}\left(1+R_{\langle j+\frac{1}{2}\rangle[n]}^{f-s\langle j\rangle s(i)s[n]}\right)T_{\langle j+1\rangle[n]}^{f-s(i)s[n]}$$

$$=-V_{D\langle j+\frac{1}{2}\rangle[n-1]}^{f-s\langle j\rangle s(i)s[n]}\left(1-R_{\langle j+\frac{1}{2}\rangle[n-1]}^{f-s\langle j\rangle s(i)s[n]}\right)T_{\langle j\rangle[n-1]}^{f-s(i)s[n]} \quad (2.64)$$

$$-2\left(1-V_{D\langle j+\frac{1}{2}\rangle[n-1]}^{f-s\langle j\rangle s(i)s[n]}\right)T_{\langle j+\frac{1}{2}\rangle[n-1]}^{f-s(i)s[n]}-V_{D\langle j+\frac{1}{2}\rangle[n-1]}^{f-s\langle j\rangle s(i)s[n]}\left(1+R_{\langle j+\frac{1}{2}\rangle[n-1]}^{f-s\langle j\rangle s(i)s[n]}\right)T_{\langle j+1\rangle[n-1]}^{f-s(i)s[n]}$$

$$-Q_{T\langle j+\frac{1}{2}\rangle[n-1]}^{f-s\langle j\rangle s(i)s[n]}-Q_{T\langle j+\frac{1}{2}\rangle[n]}^{f-s\langle j\rangle s(i)s[n]}$$

at radial sub-node $r_{\langle j+\frac{1}{2}\rangle\left[n-\frac{1}{2}\right]}^{f-s(i)s[n]}$

where $W_{[n-1]}^{f-s\langle j\rangle s(i)s[n]}$ = ratio of the conductive heat transfer coefficient of radial section $<j-$

1> to the conductive heat transfer coefficient of radial section $<j>$

in axial section *(i)* at time $t_{[n-1]}$ of time section *[n]*

$$= \left(\frac{k_{[n-1]}^{f-s\langle j-1 \rangle s(i)s[n]}}{\Delta r_{[n-1]}^{f-s\langle j-1 \rangle s(i)s[n]}} \right) \bigg/ \left(\frac{k_{[n-1]}^{f-s\langle j \rangle s(i)s[n]}}{\Delta r_{[n-1]}^{f-s\langle j \rangle s(i)s[n]}} \right)$$

$T_{\langle 1 \rangle [n-1]}^{g-s(i)s[n]}$ = gap temperature at radial sub-node $r_{\langle 1 \rangle [n-1]}^{g-s(i)s[n]}$ in axial section *(i)* at time

$t_{[n-1]}$ of time section *[n]* [K].

The number of equations contained in the simultaneous linear system is 2*f* where *f* is the number of radial sections of axial section *(i)*. These equations well accommodate the spatial variation and time dependence of the internal heat source, heat conduction, and materials properties. Also, the equations have the form of implicit functions which is unconditionally stable. However, the solutions of the equations derived by the modified Crank-Nicolson method may exhibit oscillations or overshoots[13] when the diffusion number has a very high value or a negative value. Thus, the value of the diffusion number needs to be between 0 and 1[14] by determining the size of the radial section properly according to the size of the time section. As mentioned in the calculation of the transient cladding temperature, to obtain the fuel temperature distribution in axial section *(i)* at time *t[n]* of time section *[n]*, the simultaneous linear system should be integrated with the simultaneous linear systems for the gap temperatures and the cladding temperatures in axial section *(i)* at time *t[n]* of time section *[n]*. The coefficient matrix of a merged simultaneous linear system can be treated with the Gaussian elimination method or the successive over-relaxation (SOR) method.

---

[13]The oscillations or overshoots originate not from the numerical instability but from the inherent characteristics of the original Crank-Nicolson method which are related to the diffusion number.
[14]The range of 0 to 1 also contributes to decreasing the numerical error.

2.2. Mechanical Response Models

Mechanical response models are concerned with the stress-strain analysis which determines the stress distribution in a fuel pin and the net strain of the fuel and cladding as functions of irradiation time. An accurate calculation of the mechanical behaviors is an important part of the fuel pin analysis in that the ultimate purpose of the fuel performance evaluation may be to predict the mechanical state of the cladding during irradiation. A fuel pin is considered to have failed when the cladding is breached. The mechanical response models are mutually connected not only with the adaptable mesh system and dynamic dimensioning but also with other major performance models such as the thermal response models and the fission gas induced swelling model.

2.2.1. Governing Relations for Mechanical Response Models

Three fundamental conditions are employed for the mechanical analysis: conditions for ① equilibrium of forces and moments, ② geometric compatibility, and ③ stress-strain relations. Each of the three conditions yields a set of equations whose solutions determine the state of stress and strain in a fuel pin.

In cylindrical coordinates, the equations derived from the condition for equilibrium of forces and moments are

$$\frac{1}{r}\frac{\partial}{\partial r}\left(r\sigma_r\right)+\frac{1}{r}\frac{\partial \tau_{\theta r}}{\partial \theta}+\frac{\partial \tau_{zr}}{\partial z}-\frac{1}{r}\sigma_\theta+R=0 \tag{2.65}$$

$$\frac{1}{r}\frac{\partial}{\partial r}\left(r\tau_{r\theta}\right)+\frac{1}{r}\frac{\partial \sigma_\theta}{\partial \theta}+\frac{\partial \tau_{z\theta}}{\partial z}+\frac{1}{r}\tau_{\theta r}+\Theta=0 \tag{2.66}$$

$$\frac{1}{r}\frac{\partial}{\partial r}\left(r\tau_{rz}\right)+\frac{1}{r}\frac{\partial \tau_{\theta z}}{\partial \theta}+\frac{\partial \sigma_z}{\partial z}+Z=0 \tag{2.67}$$

$$\tau_{r\theta}=\tau_{\theta r} \;\; ; \;\; \tau_{\theta z}=\tau_{z\theta} \;\; ; \;\; \tau_{zr}=\tau_{rz} \tag{2.68}$$

where R, Θ, and Z are body forces per unit volume acting in the radial direction, angular direction, and axial direction, respectively. All the components of the stress tensor are functions of r, θ, and z.

The equations derived from the condition for geometric compatibility are

$$\varepsilon_r=\frac{\partial u_r}{\partial r} \;\; ; \;\; \varepsilon_\theta=\frac{1}{r}u_r+\frac{1}{r}\frac{\partial u_\theta}{\partial \theta} \;\; ; \;\; \varepsilon_z=\frac{\partial u_z}{\partial z} \tag{2.69}$$

$$\gamma_{r\theta}=\frac{1}{r}\frac{\partial u_r}{\partial \theta}+\frac{\partial u_\theta}{\partial r}-\frac{1}{r}u_\theta \tag{2.70}$$

$$\gamma_{\theta z}=\frac{\partial u_\theta}{\partial z}+\frac{1}{r}\frac{\partial u_z}{\partial \theta} \tag{2.71}$$

$$\gamma_{zr}=\frac{\partial u_z}{\partial r}+\frac{\partial u_r}{\partial z} \tag{2.72}$$

$$\gamma_{r\theta}=\gamma_{\theta r} \;\; ; \;\; \gamma_{\theta z}=\gamma_{z\theta} \;\; ; \;\; \gamma_{zr}=\gamma_{rz} \tag{2.73}$$

where u_r, u_θ, and u_z are displacements of a point in the r-direction, θ-direction, and z-direction, respectively. The components of the displacement vector and strain tensor[15] are functions of r, θ, and z.

The equations derived from the condition for stress-strain relations are

$$\varepsilon_r=\frac{1}{E}\left[\sigma_r-v\left(\sigma_\theta+\sigma_z\right)\right]+\alpha\left(T-T_0\right)+\psi_r \tag{2.74}$$

---

[15]The stain tensor should be distinguished from the deformation tensor (also called the symmetric stain tensor) and the displacement derivative tensor. The shear components of the stain tensor have twice the values of the shear components of the deformation tensor, whereas the normal components of the stain tensor are equal to those of the deformation tensor. The displacement derivative tensor is the sum of the deformation tensor and the skew-symmetric rotation tensor.

$$\varepsilon_\theta = \frac{1}{E}\left[\sigma_\theta - \nu\left(\sigma_r + \sigma_z\right)\right] + \alpha\left(T - T_0\right) + \psi_\theta \tag{2.75}$$

$$\varepsilon_z = \frac{1}{E}\left[\sigma_z - \nu\left(\sigma_r + \sigma_\theta\right)\right] + \alpha\left(T - T_0\right) + \psi_z \tag{2.76}$$

$$\gamma_{r\theta} = \frac{\tau_{r\theta}}{G} \ ; \ \ \gamma_{\theta z} = \frac{\tau_{\theta z}}{G} \ ; \ \ \gamma_{zr} = \frac{\tau_{zr}}{G} \tag{2.77}$$

where ψ_k = permanent deformations due to swelling, creep, and plastic flow

[dimensionless] = $\varepsilon^{swelling} + \varepsilon_k^{creep} + \varepsilon_k^{plastic}$ ($k = r$, θ, or z)

E = Young's modulus (modulus of elasticity) [MPa]

G = shear modulus (modulus of rigidity) [MPa]

ν = Poisson's ratio [dimensionless]

α = coefficient of linear thermal-expansion [K^{-1}].

The swelling strain is isotropic in all directions, while the creep strain and plastic stain are distributed among the individual components of the three principal directions.

Governing Relations on the Assumption of Azimuthal Symmetry

As shown above, the three fundamental conditions produce 21 equations, which contain 21 unknown variables (9 components of the stress tensor, 9 components of the strain tensor, and 3 components of the displacement vector). These simultaneous linear equations can be simplified on the assumption of azimuthal symmetry:

$$\frac{1}{r}\frac{\partial}{\partial r}\left(r\sigma_r\right) + \frac{\partial \tau_{zr}}{\partial z} - \frac{1}{r}\sigma_\theta + R = 0 \tag{2.78}$$

$$\frac{1}{r}\frac{\partial \sigma_\theta}{\partial \theta} + \Theta = 0 \tag{2.79}$$

66

$$\frac{1}{r}\frac{\partial}{\partial r}\left(r\tau_{rz}\right)+\frac{\partial\sigma_z}{\partial z}+Z=0 \qquad (2.80)$$

$$\gamma_{zr}=\gamma_{rz} \qquad (2.81)$$

$$\varepsilon_r=\frac{\partial u_r}{\partial r}\ ;\ \ \varepsilon_\theta=\frac{1}{r}u_r\ ;\ \ \varepsilon_z=\frac{\partial u_z}{\partial z} \qquad (2.82)$$

$$0=\frac{1}{r}\frac{\partial u_r}{\partial\theta} \qquad (2.83)$$

$$0=\frac{1}{r}\frac{\partial u_z}{\partial\theta} \qquad (2.84)$$

$$\gamma_{zr}=\frac{\partial u_z}{\partial r}+\frac{\partial u_r}{\partial z} \qquad (2.85)$$

$$\gamma_{zr}=\gamma_{rz} \qquad (2.86)$$

$$\varepsilon_r=\frac{1}{E}\left[\sigma_r-\nu\left(\sigma_\theta+\sigma_z\right)\right]+\alpha\left(T-T_0\right)+\varepsilon^{swelling}+\varepsilon_r^{creep}+\varepsilon_r^{plastic} \qquad (2.87)$$

$$\varepsilon_\theta=\frac{1}{E}\left[\sigma_\theta-\nu\left(\sigma_r+\sigma_z\right)\right]+\alpha\left(T-T_0\right)+\varepsilon^{swelling}+\varepsilon_\theta^{creep}+\varepsilon_\theta^{plastic} \qquad (2.88)$$

$$\varepsilon_z=\frac{1}{E}\left[\sigma_z-\nu\left(\sigma_r+\sigma_\theta\right)\right]+\alpha\left(T-T_0\right)+\varepsilon^{swelling}+\varepsilon_z^{creep}+\varepsilon_z^{plastic} \qquad (2.89)$$

$$\gamma_{zr}=\frac{\tau_{zr}}{G} \qquad (2.90)$$

The number of equations becomes fifteen, and they contain twelve unknowns ($\tau_{r\theta}$, $\tau_{\theta r}$, $\tau_{\theta z}$, $\tau_{z\theta}$, $\gamma_{r\theta}$, $\gamma_{\theta r}$, $\gamma_{\theta z}$, $\gamma_{z\theta}$, and u_θ are zero with angular symmetry). Equation 2.79 simply represents σ_θ to be a function of r and z. Also, Equations 2.83 and 2.84 just represent that u_r and u_z are functions of r and z. Therefore, the three equations should be regarded as supplementary conditions for simultaneous solutions rather than independent equations,

which means that the simplified linear system satisfying azimuthal symmetry is not an overdetermined system.

Governing Relations on the Assumption of Azimuthal and Axial Symmetry

If axial symmetry is additionally assumed with azimuthal symmetry, considerable simplification is possible to the simultaneous linear equations and they can be reduced to seven equations with eight supplementary conditions.

$$\frac{1}{r}\frac{\partial}{\partial r}(r\sigma_r)-\frac{1}{r}\sigma_\theta=0 \tag{2.91}$$

$$\varepsilon_r=\frac{\partial u_r}{\partial r}\ ;\ \ \varepsilon_\theta=\frac{1}{r}u_r\ ;\ \ \varepsilon_z=\frac{\partial u_z}{\partial z} \tag{2.92}$$

$$\varepsilon_r=\frac{1}{E}\Big[\sigma_r-\nu\big(\sigma_\theta+\sigma_z\big)\Big]+\alpha\big(T-T_0\big)+\varepsilon^{swelling}+\varepsilon_r^{creep}+\varepsilon_r^{plastic} \tag{2.93}$$

$$\varepsilon_\theta=\frac{1}{E}\Big[\sigma_\theta-\nu\big(\sigma_r+\sigma_z\big)\Big]+\alpha\big(T-T_0\big)+\varepsilon^{swelling}+\varepsilon_\theta^{creep}+\varepsilon_\theta^{plastic} \tag{2.94}$$

$$\varepsilon_z=\frac{1}{E}\Big[\sigma_z-\nu\big(\sigma_r+\sigma_\theta\big)\Big]+\alpha\big(T-T_0\big)+\varepsilon^{swelling}+\varepsilon_z^{creep}+\varepsilon_z^{plastic} \tag{2.95}$$

supplementary conditions: ① ε_r is a function of r ② ε_θ is a function of r

           ③ ε_z is a constant   ④ u_r is a function of r

           ⑤ u_z is a function of z ⑥ σ_r is a function of r

           ⑦ σ_θ is a function of r ⑧ σ_z is a function of r.

   The shear stresses, shear strains, and angular displacement become zero on the assumption of azimuthal and axial symmetry, and the seven equations have only eight unknown variables. When the axial boundary condition is used with the third

supplementary condition, the axial strain ε_z is removed from the unknown variables. Therefore, the seven equations eventually form a determined system.

An assumption that the entire fuel pin is azimuthally and axially symmetric may be a controversial leap from the real phenomena. However, if the assumption of azimuthal and axial symmetry is applied to each small axial section of the fuel and cladding, it makes the mechanical analysis reasonably tractable. Thus, a set of seven equations should be established repeatedly for each small axial section. The time dependence is inherent in the mechanical analysis, especially due to the swelling and creep phenomena, and is handled by treating the system as a succession of equilibrium states [27].

2.2.2. Algebraic Solutions of Governing Relations

As mentioned previously, when azimuthal and axial symmetry are assumed in an axial section of the fuel or cladding, the axial strain ε_z becomes a constant within the axial section. Therefore, Equation 2.95 can be written as

$$C_z = \frac{1}{E}\left[\sigma_z - v\left(\sigma_r + \sigma_\theta\right)\right] + \alpha\left(T - T_0\right) + \varepsilon^{swelling} + \varepsilon_z^{creep} + \varepsilon_z^{plastic} \qquad (2.96)$$

where C_z is a constant that is calculated by using the axial boundary condition of each axial section. When Equations 2.93 and 2.94 are combined with Equations 2.92 and 2.96, the stresses in an axial section are expressed in terms of the radial displacement.

$$\sigma_r = \frac{E}{1+v}\left[\frac{du_r}{dr} + \frac{v}{1-2v}\left(\frac{du_r}{dr} + \frac{u_r}{r} + C_z - 3\alpha\left(T - T_0\right) - 3\varepsilon^s\right)\right]$$
$$- \frac{E}{1+v}\left[\alpha\left(T - T_0\right) + \varepsilon^s + \varepsilon_r^c\right] \qquad (2.97)$$

69

$$\sigma_\theta = \frac{E}{1+v}\left[\frac{u_r}{r} + \frac{v}{1-2v}\left(\frac{du_r}{dr} + \frac{u_r}{r} + C_z - 3\alpha(T-T_0) - 3\varepsilon^s\right)\right]$$

$$-\frac{E}{1+v}\left[\alpha(T-T_0) + \varepsilon^s + \varepsilon_\theta^c\right]$$

(2.98)

$$\sigma_z = \frac{E}{1+v}\left[C_z + \frac{v}{1-2v}\left(\frac{du_r}{dr} + \frac{u_r}{r} + C_z - 3\alpha(T-T_0) - 3\varepsilon^s\right)\right]$$

$$-\frac{E}{1+v}\left[\alpha(T-T_0) + \varepsilon^s + \varepsilon_z^c\right]$$

(2.99)

where ε^s = swelling strain [dimensionless] = $\varepsilon^{swelling}$

ε_k^c = creep and plastic strain [dimensionless] = $\varepsilon_k^{creep} + \varepsilon_k^{plastic}$ ($k = r$, θ, or z).

Equations 2.97 and 2.98 are substituted for σ_r and σ_θ in Equation 2.91, and finally, the following differential equation for the radial displacement is obtained as an algebraic solution of the seven governing equations:

$$r\frac{d}{dr}\left[\frac{E}{1+v}\left(\frac{du_r}{dr} + \frac{v}{1-2v}\left\{\frac{du_r}{dr} + \frac{u_r}{r} + C_z - 3\alpha(T-T_0) - 3\varepsilon^s\right\}\right)\right]$$

$$-r\frac{d}{dr}\left[\frac{E}{1+v}\left\{\alpha(T-T_0) + \varepsilon^s + \varepsilon_r^c\right\}\right] + \frac{E}{1+v}\left[\frac{du_r}{dr} - \frac{u_r}{r} - \varepsilon_r^c + \varepsilon_\theta^c\right] = 0$$

(2.100)

This solution is valid only within the axial section for which the seven equations were initially formulated.

Solution of Differential Equation

While the common form of algebraic solutions to a system of linear equations is that a variable is defined by a constant, the variable u_r has been given as an implicit function of r in the above solution (Equation 2.100). Moreover, the solution includes the second derivative of the radial displacement. Therefore, to make it have the common solution

70

form, Equation 2.100 should be arranged further, which is to solve the ordinary differential

equation of second order.

Applying Equation 2.100 to radial section <j> of axial section (i) yields

$$\frac{d}{dr}\left[\frac{1}{r}\frac{d}{dr}\left\{ru_r^{s\langle j\rangle s(i)}(r)\right\}\right]=$$

$$\frac{1-2v^{s\langle j\rangle s(i)}}{1-v^{s\langle j\rangle s(i)}}\left[\frac{d\varepsilon_r^{c-s\langle j\rangle s(i)}(r)}{dr}+\frac{\varepsilon_r^{c-s\langle j\rangle s(i)}(r)-\varepsilon_\theta^{c-s\langle j\rangle s(i)}(r)}{r}\right] \quad (2.101)$$

$$+\frac{1+v^{s\langle j\rangle s(i)}}{1-v^{s\langle j\rangle s(i)}}\frac{d}{dr}\left[\alpha^{s\langle j\rangle s(i)}T^{s\langle j\rangle s(i)}(r)+\varepsilon^{s-s\langle j\rangle s(i)}(r)\right]$$

where $r_{\langle j\rangle}^{s(i)}\leq r\leq r_{\langle j+1\rangle}^{s(i)}$ and $z_{(i)}\leq z\leq z_{(i+1)}$

$v^{s\langle j\rangle s(i)}$ = average Poisson's ratio in radial section <j> of axial section (i)

$\alpha^{s\langle j\rangle s(i)}$ = average linear thermal-expansion coefficient in radial section <j> of

axial section (i) [K^{-1}].

Equation 2.101 is based on the assumption that the mechanical properties E, v, and α are

constants in each radial section of an axial section. Thus, the size of radial sections should

be small enough for the mechanical properties to be reasonably represented by the

sectional averages, and the equation should be established separately for each radial

section. The indefinite integral of Equation 2.101 is

$$u_r^{s\langle j\rangle s(i)}(r)=C_1^*r+\frac{C_2^*}{r}+\frac{1}{r}\left(\frac{1+v^{s\langle j\rangle s(i)}}{1-v^{s\langle j\rangle s(i)}}\right)\int\left[\alpha^{s\langle j\rangle s(i)}T^{s\langle j\rangle s(i)}(r)+\varepsilon^{s-s\langle j\rangle s(i)}(r)\right]rdr$$

$$+\frac{1}{2r}\left(\frac{1-2v^{s\langle j\rangle s(i)}}{1-v^{s\langle j\rangle s(i)}}\right)\int\left[\varepsilon_r^{c-s\langle j\rangle s(i)}(r)+\varepsilon_\theta^{c-s\langle j\rangle s(i)}(r)\right]rdr \quad (2.102)$$

$$+\frac{r}{2}\left(\frac{1-2v^{s\langle j\rangle s(i)}}{1-v^{s\langle j\rangle s(i)}}\right)\int\frac{\varepsilon_r^{c-s\langle j\rangle s(i)}(r)-\varepsilon_\theta^{c-s\langle j\rangle s(i)}(r)}{r}dr$$

If the permanent deformations and temperature are additionally assumed to be constant within radial section *<j>* of axial section *(i)*, the radial displacement is given by

$$
\begin{aligned}
u_r^{s\langle j\rangle s(i)}(r) &= C_1^{s\langle j\rangle s(i)} r + \frac{C_2^{s\langle j\rangle s(i)}}{r} + \left(\frac{1+v^{s\langle j\rangle s(i)}}{1-v^{s\langle j\rangle s(i)}}\right)\left(\alpha^{s\langle j\rangle s(i)} T^{s\langle j\rangle s(i)} + \varepsilon^{s-s\langle j\rangle s(i)}\right)\frac{r}{2} \\
&+ \frac{1}{2}\left(\frac{1-2v^{s\langle j\rangle s(i)}}{1-v^{s\langle j\rangle s(i)}}\right)\left[\left(\varepsilon_r^{c-s\langle j\rangle s(i)} + \varepsilon_\theta^{c-s\langle j\rangle s(i)}\right)\frac{r}{2} + \left(\varepsilon_r^{c-s\langle j\rangle s(i)} - \varepsilon_\theta^{c-s\langle j\rangle s(i)}\right)r\ln r\right]
\end{aligned}
\tag{2.103}
$$

where $\varepsilon^{s-s\langle j\rangle s(i)}$ = swelling strain averaged over radial section *<j>* of axial section *(i)* [dimensionless]

$\varepsilon_r^{c-s\langle j\rangle s(i)}$ = creep and plastic strains in the radial direction averaged over radial section *<j>* of axial section *(i)* [dimensionless]

$\varepsilon_\theta^{c-s\langle j\rangle s(i)}$ = creep and plastic strains in the angular direction averaged over radial section *<j>* of axial section *(i)* [dimensionless]

$T^{s\langle j\rangle s(i)}$ = average temperature in radial section *<j>* of axial section *(i)* [K]

$C_1^{s\langle j\rangle s(i)}$ = constant of integration for radial section *<j>* of axial section *(i)* [dimensionless]

$C_2^{s\langle j\rangle s(i)}$ = constant of integration for radial section *<j>* of axial section *(i)* [cm²].

The step to solve the second order ordinary differential equation has generated two integration constants, which should be determined by two additional conditions. The radial boundary conditions for each radial section can be used as the additional conditions.

Equation 2.103 is one of the final solutions to the seven governing equations, and it is valid within radial section *<j>* of axial section *(i)*. The other final solutions for radial

section <j> of axial section (i) are derived from substituting Equation 2.103 into Equation 2.92 and Equations 2.97 to 2.99:

$$\sigma_r^{s\langle j\rangle s(i)}(r) = a^{s\langle j\rangle s(i)}\left[\left(1+2b^{s\langle j\rangle s(i)}\right)C_1^{s\langle j\rangle s(i)} - \frac{C_2^{s\langle j\rangle s(i)}}{r^2} + b^{s\langle j\rangle s(i)}C_z^{s(i)}\right]$$
$$+ a^{s\langle j\rangle s(i)}\left[\left(1+2b^{s\langle j\rangle s(i)}\right)X^{s\langle j\rangle s(i)}(r) - b^{s\langle j\rangle s(i)}m^{s\langle j\rangle s(i)}\right. \tag{2.104}$$
$$\left. + b^{s\langle j\rangle s(i)}c^{s\langle j\rangle s(i)} + d_r^{s\langle j\rangle s(i)}\right]$$

$$\sigma_\theta^{s\langle j\rangle s(i)}(r) = a^{s\langle j\rangle s(i)}\left[\left(1+2b^{s\langle j\rangle s(i)}\right)C_1^{s\langle j\rangle s(i)} + \frac{C_2^{s\langle j\rangle s(i)}}{r^2} + b^{s\langle j\rangle s(i)}C_z^{s(i)}\right]$$
$$+ a^{s\langle j\rangle s(i)}\left[\left(1+2b^{s\langle j\rangle s(i)}\right)X^{s\langle j\rangle s(i)}(r) - \left(1+b^{s\langle j\rangle s(i)}\right)m^{s\langle j\rangle s(i)}\right. \tag{2.105}$$
$$\left. + b^{s\langle j\rangle s(i)}c^{s\langle j\rangle s(i)} + d_\theta^{s\langle j\rangle s(i)}\right]$$

$$\sigma_z^{s\langle j\rangle s(i)}(r) = a^{s\langle j\rangle s(i)}\left[2b^{s\langle j\rangle s(i)}C_1^{s\langle j\rangle s(i)} + \left(1+b^{s\langle j\rangle s(i)}\right)C_z^{s(i)}\right]$$
$$+ a^{s\langle j\rangle s(i)}\left[2b^{s\langle j\rangle s(i)}X^{s\langle j\rangle s(i)}(r) - b^{s\langle j\rangle s(i)}m^{s\langle j\rangle s(i)} + b^{s\langle j\rangle s(i)}c^{s\langle j\rangle s(i)} + d_z^{s\langle j\rangle s(i)}\right] \tag{2.106}$$

$$\varepsilon_r^{s\langle j\rangle s(i)}(r) = C_1^{s\langle j\rangle s(i)} - \frac{C_2^{s\langle j\rangle s(i)}}{r^2} + X^{s\langle j\rangle s(i)}(r) \tag{2.107}$$

$$\varepsilon_\theta^{s\langle j\rangle s(i)}(r) = C_1^{s\langle j\rangle s(i)} + \frac{C_2^{s\langle j\rangle s(i)}}{r^2} + X^{s\langle j\rangle s(i)}(r) - m^{s\langle j\rangle s(i)} \tag{2.108}$$

$$u_z^{s(i)}(z) = u_{z(i)}^{s(i)} + C_z^{s(i)}\left(z - z_{(i)}\right) \tag{2.109}$$

where $a^{s\langle j\rangle s(i)} = \dfrac{E^{s\langle j\rangle s(i)}}{1+v^{s\langle j\rangle s(i)}}$ [MPa]

$$b^{s\langle j\rangle s(i)} = \frac{v^{s\langle j\rangle s(i)}}{1-2v^{s\langle j\rangle s(i)}}$$

$$c^{s\langle j\rangle s(i)} = -3\left[\alpha^{s\langle j\rangle s(i)}\left(T^{s\langle j\rangle s(i)} - T_0^{s\langle j\rangle s(i)}\right) + \varepsilon^{s-s\langle j\rangle s(i)}\right]$$

73

$$d_k^{s\langle j\rangle s(i)} = -\left[\alpha^{s\langle j\rangle s(i)}\left(T^{s\langle j\rangle s(i)} - T_0^{s\langle j\rangle s(i)}\right) + \varepsilon^{s-s\langle j\rangle s(i)} + \varepsilon_k^{c-s\langle j\rangle s(i)}\right]$$

$$= \frac{c^{s\langle j\rangle s(i)}}{3} - \varepsilon_k^{c-s\langle j\rangle s(i)} \qquad (k = r, \theta, \text{ or } z)$$

$$X^{s\langle j\rangle s(i)}(r) = \frac{1}{2}\left(\frac{1+v^{s\langle j\rangle s(i)}}{1-v^{s\langle j\rangle s(i)}}\right)\left(\alpha^{s\langle j\rangle s(i)}T^{s\langle j\rangle s(i)} + \varepsilon^{s-s\langle j\rangle s(i)}\right)$$

$$+ \frac{1}{2}\left(\frac{1-2v^{s\langle j\rangle s(i)}}{1-v^{s\langle j\rangle s(i)}}\right)\left[\frac{1}{2}\left(\varepsilon_r^{c-s\langle j\rangle s(i)} + \varepsilon_\theta^{c-s\langle j\rangle s(i)}\right) + \left(\varepsilon_r^{c-s\langle j\rangle s(i)} - \varepsilon_\theta^{c-s\langle j\rangle s(i)}\right)(\ln r + 1)\right]$$

$$m^{s\langle j\rangle s(i)} = \frac{1}{2}\left(\frac{1-2v^{s\langle j\rangle s(i)}}{1-v^{s\langle j\rangle s(i)}}\right)\left(\varepsilon_r^{c-s\langle j\rangle s(i)} - \varepsilon_\theta^{c-s\langle j\rangle s(i)}\right)$$

$u_{z(i)}^{s(i)}$ = axial displacement of axial node $z_{(i)}$ in axial section *(i)* [cm] ($u_{z(i)}^{s(i)}$ is given

from the calculation of the axial displacements in axial section *(i-1)*, and is

equal to $u_{z(i)}^{s(i-1)}$).

A set of these equations can be found, as the solutions of the seven governing equations,

for each radial section of each axial section in the same way.

Boundary Conditions

The seven solutions, Equations 2.103 to 2.109, include three unknown constants, which

are the axial strain and two integration constants. The integration constants are determined

by the following radial boundary conditions:

Radial boundary conditions for fuel slug

   o   Surface boundary

$$u_r^{f-s\langle 1\rangle s(i)}(r)\Big|_{r=r_{\langle 1\rangle}^{f-s(i)}} = 0 \qquad\qquad (2.110)$$

74

$$\left. \sigma_r^{f-s\langle f\rangle s(i)}\left(r\right)\right|_{r=r_{\langle f+1\rangle}^{f-s(i)}} = -P_{plenum} \tag{2.111}$$

o   Section boundary

$$\left. u_r^{f-s\langle j-1\rangle s(i)}\left(r\right)\right|_{r=r_{\langle j\rangle}^{f-s(i)}} = \left. u_r^{f-s\langle j\rangle s(i)}\left(r\right)\right|_{r=r_{\langle j\rangle}^{f-s(i)}} \tag{2.112}$$

$$\left. \sigma_r^{f-s\langle j\rangle s(i)}\left(r\right)\right|_{r=r_{\langle j+1\rangle}^{f-s(i)}} = \left. \sigma_r^{f-s\langle j+1\rangle s(i)}\left(r\right)\right|_{r=r_{\langle j+1\rangle}^{f-s(i)}} \tag{2.113}$$

Radial boundary conditions for cladding

o   Surface boundary

$$\left. \sigma_r^{c-s\langle 1\rangle s(i)}\left(r\right)\right|_{r=r_{\langle 1\rangle}^{c-s(i)}} = -P_{plenum} \tag{2.114}$$

$$\left. \sigma_r^{c-s\langle c\rangle s(i)}\left(r\right)\right|_{r=r_{\langle c+1\rangle}^{c-s(i)}} = -P_{cool} \tag{2.115}$$

o   Section boundary

$$\left. u_r^{c-s\langle j-1\rangle s(i)}\left(r\right)\right|_{r=r_{\langle j\rangle}^{c-s(i)}} = \left. u_r^{c-s\langle j\rangle s(i)}\left(r\right)\right|_{r=r_{\langle j\rangle}^{c-s(i)}} \tag{2.116}$$

$$\left. \sigma_r^{c-s\langle j\rangle s(i)}\left(r\right)\right|_{r=r_{\langle j+1\rangle}^{c-s(i)}} = \left. \sigma_r^{c-s\langle j+1\rangle s(i)}\left(r\right)\right|_{r=r_{\langle j+1\rangle}^{c-s(i)}} \tag{2.117}$$

where   radial section $<j>$ = an arbitrary radial section

axial section (i) = an arbitrary axial section

radial section $<f>$ = the outermost radial section of the fuel

radial section $<c>$ = the outermost radial section of the cladding

$\left. u_r^{f-s\langle 1\rangle s(i)}\left(r\right)\right|_{r=r_{\langle 1\rangle}^{f-s(i)}}$ = radial displacement of the first radial node $r_{\langle 1\rangle}^{f-s(i)}$ in axial

section (i) of the fuel [cm] = $u_{r-in}^{f-s(i)}$

75

$$\left. \sigma_r^{f-s\langle f\rangle s(i)}(r)\right|_{r=r_{\langle f+1\rangle}^{f-s(i)}} = \text{radial stress at the last radial node } r_{\langle f+1\rangle}^{f-s(i)} \text{ in axial section } (i)$$

$$\text{of the fuel [MPa]} = \sigma_{r-out}^{f-s(i)}$$

P_{plenum} = plenum pressure in the fuel pin of interest [MPa]

$$\left. u_r^{f-s\langle j-1\rangle s(i)}(r)\right|_{r=r_{\langle j\rangle}^{f-s(i)}} = \text{radial displacement of radial node } r_{\langle j\rangle}^{f-s(i)} \text{ of radial section}$$

$$\langle j\text{-}1\rangle \text{ in axial section } (i) \text{ of the fuel [cm]} = u_{r\langle j\rangle}^{f-s\langle j-1\rangle s(i)}$$

$$\left. \sigma_r^{f-s\langle j\rangle s(i)}(r)\right|_{r=r_{\langle j+1\rangle}^{f-s(i)}} = \text{radial stress at radial node } r_{\langle j+1\rangle}^{f-s(i)} \text{ of radial section } \langle j\rangle \text{ in}$$

$$\text{axial section } (i) \text{ of the fuel [MPa]} = \sigma_{r\langle j+1\rangle}^{f-s\langle j\rangle s(i)}$$

P_{cool} = coolant pressure acting on the outside of the cladding [MPa].

Equation 2.110 is based on the assumption that no central void is developed at the center of fuel[16]. The axial strain of an axial section is computed by using the axial boundary condition shown below:

Axial boundary condition for fuel slug

$$\int_{r_{\langle 1\rangle}^{f-s(i)}}^{r_{\langle f+1\rangle}^{f-s(i)}} \sigma_z^{f-s(i)}(r)\cdot 2\pi r dr = -\pi\left[\left(r_{\langle f+1\rangle}^{f-s(i)}\right)^2 - \left(r_{\langle 1\rangle}^{f-s(i)}\right)^2\right]P_{plenum} - \sum_{n=i+1}^{N} W_t^{f-s(n)} \quad (2.118)$$

Axial boundary condition for cladding

$$\int_{r_{\langle 1\rangle}^{c-s(i)}}^{r_{\langle c+1\rangle}^{c-s(i)}} \sigma_z^{c-s(i)}(r)\cdot 2\pi r dr = -\pi\left(r_{\langle c+1\rangle}^{c-s(i)}\right)^2 P_{cool} + \pi\left(r_{\langle 1\rangle}^{c-s(i)}\right)^2 P_{plenum} - \sum_{n=i+1}^{N} W_t^{c-s(n)} \quad (2.119)$$

---

[16]If the central void is developed, Equation 2.110 should be replaced with

$$\left. \sigma_r^{f-s\langle 1\rangle s(i)}(r)\right|_{r=r_{\langle 1\rangle}^{f-s(i)}} = -P_{plenum}$$

where $\sigma_z^{f-s(i)}(r)$ = axial stress at radial node r in axial section *(i)* of the fuel [MPa]

$W_t^{f-s(i+1)}$ = weight of axial section *(i+1)* of the fuel [MPa·cm²] or [10²·N]

N = number of axial sections.

The boundary conditions actually depend on whether the gap is open or closed, and the conditions described above are valid in an open-gap situation. If the gap is closed, the radial boundary conditions at the outer surface of the fuel and the inner surface of the cladding (Equations 2.111 and 2.114) should be replaced by the fuel-cladding-interfacial conditions:

$$\sigma_r^{f-s\langle f\rangle s(i)}(r)\Big|_{r=r_{\langle f+1\rangle}^{f-s(i)}} = -P_{contact}^{s(i)} \tag{2.120}$$

$$\sigma_r^{c-s\langle 1\rangle s(i)}(r)\Big|_{r=r_{\langle 1\rangle}^{c-s(i)}} = -P_{contact}^{s(i)} \tag{2.121}$$

where $P_{contact}^{s(i)}$ is a contact pressure at axial section *(i)*, which is yet to be determined. Also, the axial boundary conditions for the closed-gap situation must be

$$\int_{r_{\langle 1\rangle}^{f-s(i)}}^{r_{\langle f+1\rangle}^{f-s(i)}} \sigma_z^{f-s(i)}(r)\cdot 2\pi r dr =$$

$$-\pi\left[\left(r_{\langle f+1\rangle}^{f-s(i)}\right)^2 - \left(r_{\langle 1\rangle}^{f-s(i)}\right)^2\right]P_{plenum} - \sum_{n=i+1}^{N} W_t^{f-s(n)} - \sum_{n=i}^{N} F_f^{s(n)} \tag{2.122}$$

in axial section *(i)* of the fuel, and

$$\int_{r_{\langle 1\rangle}^{c-s(i)}}^{r_{\langle c+1\rangle}^{c-s(i)}} \sigma_z^{c-s(i)}(r)\cdot 2\pi r dr =$$

$$-\pi\left(r_{\langle c+1\rangle}^{c-s(i)}\right)^2 P_{cool} + \pi\left(r_{\langle 1\rangle}^{c-s(i)}\right)^2 P_{plenum} - \sum_{n=i+1}^{N} W_t^{c-s(n)} + \sum_{n=i}^{N} F_f^{s(n)} \tag{2.123}$$

in axial section *(i)* of the cladding. $F_f^{s(i)}$ is the friction force acting vertically on the outer surface of the fuel at axial section *(i)*. The friction force has a positive value in Equations 2.122 and 2.123 when it restricts axial growth of the fuel.

Equations 2.120 to 2.123 contain two unknowns, the fuel-cladding-interfacial pressure and the friction force, and they can be determined by the following contact conditions:

$$
u_r^{f-s\langle f\rangle s(i)}(r)\Big|_{r=r_{\langle f+1\rangle}^{f-s(i)}} - \left[u_r^{f-s\langle f\rangle s(i)}(r)\Big|_{r=r_{\langle f+1\rangle}^{f-s(i)}}\right]_{contact}
$$
$$
= u_r^{c-s\langle 1\rangle s(i)}(r)\Big|_{r=r_{\langle 1\rangle}^{c-s(i)}} - \left[u_r^{c-s\langle 1\rangle s(i)}(r)\Big|_{r=r_{\langle 1\rangle}^{c-s(i)}}\right]_{contact}
$$

(2.124)

$$
u_z^{f-s(i)}(z)\Big|_{z=z_{(i+1)}^f} - \left[u_z^{f-s(i)}(z)\Big|_{z=z_{(i+1)}^f}\right]_{contact}
$$
$$
= u_z^{c-s(i)}(z)\Big|_{z=z_{(i+1)}^c} - \left[u_z^{c-s(i)}(z)\Big|_{z=z_{(i+1)}^c}\right]_{contact}
$$

(2.125)

where $u_r^{f-s\langle f\rangle s(i)}(r)\Big|_{r=r_{\langle f+1\rangle}^{f-s(i)}}$ = radial displacement of the last radial node $r_{\langle f+1\rangle}^{f-s(i)}$ in axial

section *(i)* of the fuel [cm] = $u_{r-out}^{f-s(i)}$

$\left[u_r^{c-s\langle 1\rangle s(i)}(r)\Big|_{r=r_{\langle 1\rangle}^{c-s(i)}}\right]_{contact}$ = radial displacement of the first radial node $r_{\langle 1\rangle}^{c-s(i)}$ in

axial section *(i)* of the cladding until gap closure [cm]

$= \left[u_{r-in}^{c-s(i)}\right]_{contact}$

$$\left[u_z^{f-s(i)}(z) \Big|_{z=z_{(i+1)}^f} \right]_{contact} = \text{axial displacement of axial node } z_{(i+1)}^f \text{ in axial section } (i)$$

$$\text{of the fuel until gap closure [cm]} = \left[u_{z(i+1)}^{f-s(i)} \right]_{contact}.$$

Equation 2.125 assumes that the fuel and the cladding are so tightly wedged together that they move axially in unison after the fuel-cladding contact. This stick situation occurs only when

$$F_f^{s(i)} < \mu_{static} \left[2\pi r_{\langle f+1 \rangle}^{f-s(i)} \left(z_{(i+1)}^f - z_{(i)}^f \right) \right] P_{contact}^{s(i)} \tag{2.126}$$

where μ_{static} is the coefficient of static friction. Therefore, if the friction force computed from Equation 2.125 does not satisfy Equation 2.126 and is large enough to permit relative axial displacement, the value of the friction force should be recalculated by considering a slip situation:

$$F_f^{s(i)} = \mu_{sliding} \left[2\pi r_{\langle f+1 \rangle}^{f-s(i)} \left(z_{(i+1)}^f - z_{(i)}^f \right) \right] P_{contact}^{s(i)} \tag{2.127}$$

where $\mu_{sliding}$ is the coefficient of sliding friction.

2.2.3. Mechanical Response Models under Open-Gap Condition

The mechanical response models for the open-gap situation are obtained from determining the axial strain and integral constants by using the open-gap boundary conditions. Applying the radial boundary conditions in the open-gap situation to the solutions for the radial displacement and radial stress in axial section *(i)* of the fuel gives the following simultaneous linear system whose variables are the axial strain of axial section *(i)* and the integral constants of each radial section:

79

First radial section (radial section *<1>*)

$$a^{f-s\langle 1\rangle s(i)}\left(1+2b^{f-s\langle 1\rangle s(i)}\right)C_1^{f-s\langle 1\rangle s(i)}$$

$$-a^{f-s\langle 2\rangle s(i)}\left(1+2b^{f-s\langle 2\rangle s(i)}\right)C_1^{f-s\langle 2\rangle s(i)}+\frac{a^{f-s\langle 2\rangle s(i)}}{\left(r_{\langle 2\rangle}^{f-s(i)}\right)^2}C_2^{f-s\langle 2\rangle s(i)}$$

$$+\left(a^{f-s\langle 1\rangle s(i)}b^{f-s\langle 1\rangle s(i)}-a^{f-s\langle 2\rangle s(i)}b^{f-s\langle 2\rangle s(i)}\right)C_z^{f-s(i)}$$

$$=a^{f-s\langle 2\rangle s(i)}\left[\left(1+2b^{f-s\langle 2\rangle s(i)}\right)X_{\langle 2\rangle}^{f-s\langle 2\rangle s(i)}-b^{f-s\langle 2\rangle s(i)}m^{f-s\langle 2\rangle s(i)}\right] \qquad (2.128)$$

$$+a^{f-s\langle 2\rangle s(i)}\left[b^{f-s\langle 2\rangle s(i)}c^{f-s\langle 2\rangle s(i)}+d_r^{f-s\langle 2\rangle s(i)}\right]$$

$$-a^{f-s\langle 1\rangle s(i)}\left[\left(1+2b^{f-s\langle 1\rangle s(i)}\right)X_{\langle 2\rangle}^{f-s\langle 1\rangle s(i)}-b^{f-s\langle 1\rangle s(i)}m^{f-s\langle 1\rangle s(i)}\right]$$

$$-a^{f-s\langle 1\rangle s(i)}\left[b^{f-s\langle 1\rangle s(i)}c^{f-s\langle 1\rangle s(i)}+d_r^{f-s\langle 1\rangle s(i)}\right]$$

Second radial section (radial section *<2>*)

$$r_{\langle 2\rangle}^{f-s(i)}C_1^{f-s\langle 1\rangle s(i)}-r_{\langle 2\rangle}^{f-s(i)}C_1^{f-s\langle 2\rangle s(i)}-\frac{1}{r_{\langle 2\rangle}^{f-s(i)}}C_2^{f-s\langle 2\rangle s(i)}=W_{\langle 2\rangle}^{f-s\langle 2\rangle s(i)}-W_{\langle 2\rangle}^{f-s\langle 1\rangle s(i)} \qquad (2.129)$$

at radial node $r_{\langle 2\rangle}^{f-s(i)}$, and

$$a^{f-s\langle 2\rangle s(i)}\left(1+2b^{f-s\langle 2\rangle s(i)}\right)C_1^{f-s\langle 2\rangle s(i)}-\frac{a^{f-s\langle 2\rangle s(i)}}{\left(r_{\langle 3\rangle}^{f-s(i)}\right)^2}C_2^{f-s\langle 2\rangle s(i)}$$

$$-a^{f-s\langle 3\rangle s(i)}\left(1+2b^{f-s\langle 3\rangle s(i)}\right)C_1^{f-s\langle 3\rangle s(i)}+\frac{a^{f-s\langle 3\rangle s(i)}}{\left(r_{\langle 3\rangle}^{f-s(i)}\right)^2}C_2^{f-s\langle 3\rangle s(i)}$$

$$+\left(a^{f-s\langle 2\rangle s(i)}b^{f-s\langle 2\rangle s(i)}-a^{f-s\langle 3\rangle s(i)}b^{f-s\langle 3\rangle s(i)}\right)C_z^{f-s(i)}$$

$$=a^{f-s\langle 3\rangle s(i)}\left[\left(1+2b^{f-s\langle 3\rangle s(i)}\right)X_{\langle 3\rangle}^{f-s\langle 3\rangle s(i)}-b^{f-s\langle 3\rangle s(i)}m^{f-s\langle 3\rangle s(i)}\right] \qquad (2.130)$$

$$+a^{f-s\langle 3\rangle s(i)}\left[b^{f-s\langle 3\rangle s(i)}c^{f-s\langle 3\rangle s(i)}+d_r^{f-s\langle 3\rangle s(i)}\right]$$

$$-a^{f-s\langle 2\rangle s(i)}\left[\left(1+2b^{f-s\langle 2\rangle s(i)}\right)X_{\langle 3\rangle}^{f-s\langle 2\rangle s(i)}-b^{f-s\langle 2\rangle s(i)}m^{f-s\langle 2\rangle s(i)}\right]$$

$$-a^{f-s\langle 2\rangle s(i)}\left[b^{f-s\langle 2\rangle s(i)}c^{f-s\langle 2\rangle s(i)}+d_r^{f-s\langle 2\rangle s(i)}\right]$$

at radial node $r_{\langle 3\rangle}^{f-s(i)}$

Last radial section (radial section <f>)

$$r_{\langle f \rangle}^{f-s(i)} C_1^{f-s\langle f-1 \rangle s(i)} + \frac{1}{r_{\langle f \rangle}^{f-s(i)}} C_2^{f-s\langle f-1 \rangle s(i)} - r_{\langle f \rangle}^{f-s(i)} C_1^{f-s\langle f \rangle s(i)} - \frac{1}{r_{\langle f \rangle}^{f-s(i)}} C_2^{f-s\langle f \rangle s(i)}$$
$$= W_{\langle f \rangle}^{f-s\langle f \rangle s(i)} - W_{\langle f \rangle}^{f-s\langle f-1 \rangle s(i)} \quad (2.131)$$

at radial node $r_{\langle f \rangle}^{f-s(i)}$, and

$$a^{f-s\langle f \rangle s(i)} \left(1 + 2b^{f-s\langle f \rangle s(i)}\right) C_1^{f-s\langle f \rangle s(i)} - \frac{a^{f-s\langle f \rangle s(i)}}{\left(r_{\langle f+1 \rangle}^{f-s(i)}\right)^2} C_2^{f-s\langle f \rangle s(i)}$$
$$+ a^{f-s\langle f \rangle s(i)} b^{f-s\langle f \rangle s(i)} C_z^{f-s(i)} \quad (2.132)$$
$$= -P_{plenum} - a^{f-s\langle f \rangle s(i)} \left[\left(1 + 2b^{f-s\langle f \rangle s(i)}\right) X_{\langle f+1 \rangle}^{f-s\langle f \rangle s(i)} - b^{f-s\langle f \rangle s(i)} m^{f-s\langle f \rangle s(i)}\right]$$
$$- a^{f-s\langle f \rangle s(i)} \left[b^{f-s\langle f \rangle s(i)} c^{f-s\langle f \rangle s(i)} + d_r^{f-s\langle f \rangle s(i)}\right]$$

at radial node $r_{\langle f+1 \rangle}^{f-s(i)}$

The others (arbitrary radial section <j>, 2 < j < f)

$$r_{\langle j \rangle}^{f-s(i)} C_1^{f-s\langle j-1 \rangle s(i)} + \frac{1}{r_{\langle j \rangle}^{f-s(i)}} C_2^{f-s\langle j-1 \rangle s(i)} - r_{\langle j \rangle}^{f-s(i)} C_1^{f-s\langle j \rangle s(i)} - \frac{1}{r_{\langle j \rangle}^{f-s(i)}} C_2^{f-s\langle j \rangle s(i)}$$
$$= W_{\langle j \rangle}^{f-s\langle j \rangle s(i)} - W_{\langle j \rangle}^{f-s\langle j-1 \rangle s(i)} \quad (2.133)$$

at radial node $r_{\langle j \rangle}^{f-s(i)}$, and

$$a^{f-s\langle j\rangle s(i)}\left(1+2b^{f-s\langle j\rangle s(i)}\right)C_1^{f-s\langle j\rangle s(i)} - \frac{a^{f-s\langle j\rangle s(i)}}{\left(r_{\langle j+1\rangle}^{f-s(i)}\right)^2}C_2^{f-s\langle j\rangle s(i)}$$

$$-a^{f-s\langle j+1\rangle s(i)}\left(1+2b^{f-s\langle j+1\rangle s(i)}\right)C_1^{f-s\langle j+1\rangle s(i)} + \frac{a^{f-s\langle j+1\rangle s(i)}}{\left(r_{\langle j+1\rangle}^{f-s(i)}\right)^2}C_2^{f-s\langle j+1\rangle s(i)}$$

$$+\left(a^{f-s\langle j\rangle s(i)}b^{f-s\langle j\rangle s(i)} - a^{f-s\langle j+1\rangle s(i)}b^{f-s\langle j+1\rangle s(i)}\right)C_z^{f-s(i)}$$

$$= a^{f-s\langle j+1\rangle s(i)}\left[\left(1+2b^{f-s\langle j+1\rangle s(i)}\right)X_{\langle j+1\rangle}^{f-s\langle j+1\rangle s(i)} - b^{f-s\langle j+1\rangle s(i)}m^{f-s\langle j+1\rangle s(i)}\right] \qquad (2.134)$$

$$+a^{f-s\langle j+1\rangle s(i)}\left[b^{f-s\langle j+1\rangle s(i)}c^{f-s\langle j+1\rangle s(i)} + d_r^{f-s\langle j+1\rangle s(i)}\right]$$

$$-a^{f-s\langle j\rangle s(i)}\left[\left(1+2b^{f-s\langle j\rangle s(i)}\right)X_{\langle j+1\rangle}^{f-s\langle j\rangle s(i)} - b^{f-s\langle j\rangle s(i)}m^{f-s\langle j\rangle s(i)}\right]$$

$$-a^{f-s\langle j\rangle s(i)}\left[b^{f-s\langle j\rangle s(i)}c^{f-s\langle j\rangle s(i)} + d_r^{f-s\langle j\rangle s(i)}\right]$$

at radial node $r_{\langle j+1\rangle}^{f-s(i)}$

where $X_{\langle j+1\rangle}^{f-s\langle j\rangle s(i)} = \frac{1}{2}\left(\frac{1+v^{f-s\langle j\rangle s(i)}}{1-v^{f-s\langle j\rangle s(i)}}\right)\left(\alpha^{f-s\langle j\rangle s(i)}T^{f-s\langle j\rangle s(i)} + \varepsilon^{s-f-s\langle j\rangle s(i)}\right)$

$$+\frac{1}{2}\left(\frac{1-2v^{f-s\langle j\rangle s(i)}}{1-v^{f-s\langle j\rangle s(i)}}\right)\left[\frac{1}{2}\left(\varepsilon_r^{c-f-s\langle j\rangle s(i)} + \varepsilon_\theta^{c-f-s\langle j\rangle s(i)}\right)\right.$$

$$\left.+\left(\varepsilon_r^{c-f-s\langle j\rangle s(i)} - \varepsilon_\theta^{c-f-s\langle j\rangle s(i)}\right)\left(\ln r_{\langle j+1\rangle}^{f-s(i)} +1\right)\right]$$

$$W_{\langle j\rangle}^{f-s\langle j-1\rangle s(i)} = \left(\frac{1+v^{f-s\langle j-1\rangle s(i)}}{1-v^{f-s\langle j-1\rangle s(i)}}\right)\left(\alpha^{f-s\langle j-1\rangle s(i)}T^{f-s\langle j-1\rangle s(i)} + \varepsilon^{s-f-s\langle j-1\rangle s(i)}\right)\frac{r_{\langle j\rangle}^{f-s(i)}}{2}$$

$$+\frac{1}{2}\left(\frac{1-2v^{f-s\langle j-1\rangle s(i)}}{1-v^{f-s\langle j-1\rangle s(i)}}\right)\left[\left(\varepsilon_r^{c-f-s\langle j-1\rangle s(i)} + \varepsilon_\theta^{c-f-s\langle j-1\rangle s(i)}\right)\frac{r_{\langle j\rangle}^{f-s(i)}}{2}\right.$$

$$\left.+\left(\varepsilon_r^{c-f-s\langle j-1\rangle s(i)} - \varepsilon_\theta^{c-f-s\langle j-1\rangle s(i)}\right)\left(r_{\langle j\rangle}^{f-s(i)}\ln r_{\langle j\rangle}^{f-s(i)}\right)\right].$$

The number of equations contained in the simultaneous linear system is $2f-1$ where f is the number of radial sections in axial section *(i)* of the fuel. The integral constant C_2 of the first radial section becomes zero from the radial boundary condition at the center of the fuel (Equation 2.110), and the simultaneous linear equations have only $2f-1$ integral

82

constants[17]. However, the axial strain of axial section *(i)* of the fuel is yet an unknown variable, which requires an additional equation for a determined system.

The additional equation can be obtained from the axial boundary condition at axial section *(i)* of the fuel (Equation 2.118). Applying the axial boundary condition to the solution for the axial stress in axial section *(i)* yields

$$
\sum_{j=1}^{f}\left[F_{\delta r}^{f-s\langle j\rangle s(i)}C_{1}^{f-s\langle j\rangle s(i)}\right]+\sum_{j=1}^{f}\left[G_{\delta r}^{f-s\langle j\rangle s(i)}\right]C_{z}^{f-s(i)}=
$$

$$
-\frac{1}{2}\left[\left(r_{\langle f+1\rangle}^{f-s(i)}\right)^{2}-\left(r_{\langle 1\rangle}^{f-s(i)}\right)^{2}\right]P_{plenum}-\frac{1}{2\pi}\sum_{n=i+1}^{N}W_{t}^{f-s(n)}-\sum_{j=1}^{f}\left[H_{\delta r}^{f-s\langle j\rangle s(i)}\right] \tag{2.135}
$$

$$
-\sum_{j=1}^{f}\left[a^{f-s\langle j\rangle s(i)}b^{f-s\langle j\rangle s(i)}\left(r_{\langle j+1\rangle}^{f-s(i)}W_{\langle j+1\rangle}^{f-s\langle j\rangle s(i)}-r_{\langle j\rangle}^{f-s(i)}W_{\langle j\rangle}^{f-s\langle j\rangle s(i)}\right)\right]
$$

where $\quad F_{\delta r}^{f-s\langle j\rangle s(i)}=a^{f-s\langle j\rangle s(i)}b^{f-s\langle j\rangle s(i)}\left[\left(r_{\langle j+1\rangle}^{f-s(i)}\right)^{2}-\left(r_{\langle j\rangle}^{f-s(i)}\right)^{2}\right]$

---

[17]The solution for the radial displacement has a singularity at radial node $r_{\langle 1\rangle}^{f-s(i)}$, so the application of the radial boundary condition at the center of the fuel to the solution is written as

$$
\lim_{r\to 0}\left[C_{1}^{f-s\langle 1\rangle s(i)}r+\frac{C_{2}^{f-s\langle 1\rangle s(i)}}{r}\right.
$$

$$
+\frac{1}{2}\left(\frac{1-2\nu^{f-s\langle 1\rangle s(i)}}{1-\nu^{f-s\langle 1\rangle s(i)}}\right)\left\{\left(\varepsilon_{r}^{c-f-s\langle 1\rangle s(i)}+\varepsilon_{\theta}^{c-f-s\langle 1\rangle s(i)}\right)\frac{r}{2}+\left(\varepsilon_{r}^{c-f-s\langle 1\rangle s(i)}-\varepsilon_{\theta}^{c-f-s\langle 1\rangle s(i)}\right)(r\ln r)\right\}
$$

$$
\left.+\left(\frac{1+\nu^{f-s\langle 1\rangle s(i)}}{1-\nu^{f-s\langle 1\rangle s(i)}}\right)\left(\alpha^{f-s\langle 1\rangle s(i)}T^{f-s\langle 1\rangle s(i)}+\varepsilon^{s-f-s\langle 1\rangle s(i)}\right)\frac{r}{2}\right]=0
$$

The above equation is arranged further to

$$
\lim_{r\to 0}\left[\frac{C_{2}^{f-s\langle 1\rangle s(i)}}{r}+\frac{1}{2}\left(\frac{1-2\nu^{f-s\langle 1\rangle s(i)}}{1-\nu^{f-s\langle 1\rangle s(i)}}\right)\left(\varepsilon_{r}^{c-f-s\langle 1\rangle s(i)}-\varepsilon_{\theta}^{c-f-s\langle 1\rangle s(i)}\right)\frac{\ln r}{\frac{1}{r}}\right]=0
$$

and, finally becomes

$$
C_{2}^{f-s\langle 1\rangle s(i)}=0
$$

by L'Hospital's rule.

83

$$G_{\delta r}^{f-s\langle j\rangle s(i)} = a^{f-s\langle j\rangle s(i)}\left(1+b^{f-s\langle j\rangle s(i)}\right)\left[\frac{\left(r_{\langle j+1\rangle}^{f-s(i)}\right)^2 - \left(r_{\langle j\rangle}^{f-s(i)}\right)^2}{2}\right]$$

$$H_{\delta r}^{f-s\langle j\rangle s(i)} = a^{f-s\langle j\rangle s(i)}\left(b^{f-s\langle j\rangle s(i)}c^{f-s\langle j\rangle s(i)} + d_z^{f-s\langle j\rangle s(i)}\right)\left[\frac{\left(r_{\langle j+1\rangle}^{f-s(i)}\right)^2 - \left(r_{\langle j\rangle}^{f-s(i)}\right)^2}{2}\right].$$

When no central void is developed, $r_{\langle 1\rangle}^{f-s(i)}W_{\langle 1\rangle}^{f-s\langle 1\rangle s(i)}$ has an indeterminate form, which goes

to zero. Equation 2.135 should be included into the simultaneous linear system for the

calculation of the axial strain and integral constants. The coefficient matrix can be treated

with the Gaussian elimination method or the successive over-relaxation (SOR) method.

In the cladding, applying the radial boundary conditions of the open-gap situation

to the solutions for the radial displacement and radial stress in axial section *(i)* gives the

following simultaneous linear system:

First radial section (radial section *<1>*)

$$a^{c-s\langle 1\rangle s(i)}\left(1+2b^{c-s\langle 1\rangle s(i)}\right)C_1^{c-s\langle 1\rangle s(i)} - \frac{a^{c-s\langle 1\rangle s(i)}}{\left(r_{\langle 1\rangle}^{c-s(i)}\right)^2}C_2^{c-s\langle 1\rangle s(i)}$$

$$+ a^{c-s\langle 1\rangle s(i)}b^{c-s\langle 1\rangle s(i)}C_z^{c-s(i)} \qquad (2.136)$$

$$= -P_{plenum} - a^{c-s\langle 1\rangle s(i)}\left[\left(1+2b^{c-s\langle 1\rangle s(i)}\right)X_{\langle 1\rangle}^{c-s\langle 1\rangle s(i)} - b^{c-s\langle 1\rangle s(i)}m^{c-s\langle 1\rangle s(i)}\right]$$

$$- a^{c-s\langle 1\rangle s(i)}\left[b^{c-s\langle 1\rangle s(i)}c^{c-s\langle 1\rangle s(i)} + d_r^{c-s\langle 1\rangle s(i)}\right]$$

at radial node $r_{\langle 1\rangle}^{c-s(i)}$, and

$$a^{c-s\langle 1\rangle s(i)}\left(1+2b^{c-s\langle 1\rangle s(i)}\right)C_1^{c-s\langle 1\rangle s(i)} - \frac{a^{c-s\langle 1\rangle s(i)}}{\left(r_{\langle 2\rangle}^{c-s(i)}\right)^2}C_2^{c-s\langle 1\rangle s(i)}$$

$$-a^{c-s\langle 2\rangle s(i)}\left(1+2b^{c-s\langle 2\rangle s(i)}\right)C_1^{c-s\langle 2\rangle s(i)} + \frac{a^{c-s\langle 2\rangle s(i)}}{\left(r_{\langle 2\rangle}^{c-s(i)}\right)^2}C_2^{c-s\langle 2\rangle s(i)}$$

$$+\left(a^{c-s\langle 1\rangle s(i)}b^{c-s\langle 1\rangle s(i)} - a^{c-s\langle 2\rangle s(i)}b^{c-s\langle 2\rangle s(i)}\right)C_z^{c-s(i)}$$

$$= a^{c-s\langle 2\rangle s(i)}\left[\left(1+2b^{c-s\langle 2\rangle s(i)}\right)X_{\langle 2\rangle}^{c-s\langle 2\rangle s(i)} - b^{c-s\langle 2\rangle s(i)}m^{c-s\langle 2\rangle s(i)}\right] \tag{2.137}$$

$$+a^{c-s\langle 2\rangle s(i)}\left[b^{c-s\langle 2\rangle s(i)}c^{c-s\langle 2\rangle s(i)} + d_r^{c-s\langle 2\rangle s(i)}\right]$$

$$-a^{c-s\langle 1\rangle s(i)}\left[\left(1+2b^{c-s\langle 1\rangle s(i)}\right)X_{\langle 2\rangle}^{c-s\langle 1\rangle s(i)} - b^{c-s\langle 1\rangle s(i)}m^{c-s\langle 1\rangle s(i)}\right]$$

$$-a^{c-s\langle 1\rangle s(i)}\left[b^{c-s\langle 1\rangle s(i)}c^{c-s\langle 1\rangle s(i)} + d_r^{c-s\langle 1\rangle s(i)}\right]$$

at radial node $r_{\langle 2\rangle}^{c-s(i)}$

Last radial section (radial section <c>)

$$r_{\langle c\rangle}^{c-s(i)}C_1^{c-s\langle c-1\rangle s(i)} + \frac{1}{r_{\langle c\rangle}^{c-s(i)}}C_2^{c-s\langle c-1\rangle s(i)} - r_{\langle c\rangle}^{c-s(i)}C_1^{c-s\langle c\rangle s(i)} - \frac{1}{r_{\langle c\rangle}^{c-s(i)}}C_2^{c-s\langle c\rangle s(i)}$$

$$= W_{\langle c\rangle}^{c-s\langle c\rangle s(i)} - W_{\langle c\rangle}^{c-s\langle c-1\rangle s(i)} \tag{2.138}$$

at radial node $r_{\langle c\rangle}^{c-s(i)}$, and

$$a^{c-s\langle c\rangle s(i)}\left(1+2b^{c-s\langle c\rangle s(i)}\right)C_1^{c-s\langle c\rangle s(i)} - \frac{a^{c-s\langle c\rangle s(i)}}{\left(r_{\langle c+1\rangle}^{c-s(i)}\right)^2}C_2^{c-s\langle c\rangle s(i)}$$

$$+a^{c-s\langle c\rangle s(i)}b^{c-s\langle c\rangle s(i)}C_z^{c-s(i)} \tag{2.139}$$

$$= -P_{cool} - a^{c-s\langle c\rangle s(i)}\left[\left(1+2b^{c-s\langle c\rangle s(i)}\right)X_{\langle c+1\rangle}^{c-s\langle c\rangle s(i)} - b^{c-s\langle c\rangle s(i)}m^{c-s\langle c\rangle s(i)}\right]$$

$$-a^{c-s\langle c\rangle s(i)}\left[b^{c-s\langle c\rangle s(i)}c^{c-s\langle c\rangle s(i)} + d_r^{c-s\langle c\rangle s(i)}\right]$$

at radial node $r_{\langle c+1\rangle}^{c-s(i)}$

The others (arbitrary radial section <j>, 1 < j < c)

$$r_{\langle j \rangle}^{c-s(i)} C_1^{c-s\langle j-1 \rangle s(i)} + \frac{1}{r_{\langle j \rangle}^{c-s(i)}} C_2^{c-s\langle j-1 \rangle s(i)} - r_{\langle j \rangle}^{c-s(i)} C_1^{c-s\langle j \rangle s(i)} - \frac{1}{r_{\langle j \rangle}^{c-s(i)}} C_2^{c-s\langle j \rangle s(i)} \tag{2.140}$$

$$= W_{\langle j \rangle}^{c-s\langle j \rangle s(i)} - W_{\langle j \rangle}^{c-s\langle j-1 \rangle s(i)}$$

at radial node $r_{\langle j \rangle}^{c-s(i)}$, and

$$a^{c-s\langle j \rangle s(i)}\left(1+2b^{c-s\langle j \rangle s(i)}\right)C_1^{c-s\langle j \rangle s(i)} - \frac{a^{c-s\langle j \rangle s(i)}}{\left(r_{\langle j+1 \rangle}^{c-s(i)}\right)^2}C_2^{c-s\langle j \rangle s(i)}$$

$$- a^{c-s\langle j+1 \rangle s(i)}\left(1+2b^{c-s\langle j+1 \rangle s(i)}\right)C_1^{c-s\langle j+1 \rangle s(i)} + \frac{a^{c-s\langle j+1 \rangle s(i)}}{\left(r_{\langle j+1 \rangle}^{c-s(i)}\right)^2}C_2^{c-s\langle j+1 \rangle s(i)}$$

$$+ \left(a^{c-s\langle j \rangle s(i)}b^{c-s\langle j \rangle s(i)} - a^{c-s\langle j+1 \rangle s(i)}b^{c-s\langle j+1 \rangle s(i)}\right)C_z^{c-s(i)}$$

$$= a^{c-s\langle j+1 \rangle s(i)}\left[\left(1+2b^{c-s\langle j+1 \rangle s(i)}\right)X_{\langle j+1 \rangle}^{c-s\langle j+1 \rangle s(i)} - b^{c-s\langle j+1 \rangle s(i)}m^{c-s\langle j+1 \rangle s(i)}\right] \tag{2.141}$$

$$+ a^{c-s\langle j+1 \rangle s(i)}\left[b^{c-s\langle j+1 \rangle s(i)}c^{c-s\langle j+1 \rangle s(i)} + d_r^{c-s\langle j+1 \rangle s(i)}\right]$$

$$- a^{c-s\langle j \rangle s(i)}\left[\left(1+2b^{c-s\langle j \rangle s(i)}\right)X_{\langle j+1 \rangle}^{c-s\langle j \rangle s(i)} - b^{c-s\langle j \rangle s(i)}m^{c-s\langle j \rangle s(i)}\right]$$

$$- a^{c-s\langle j \rangle s(i)}\left[b^{c-s\langle j \rangle s(i)}c^{c-s\langle j \rangle s(i)} + d_r^{c-s\langle j \rangle s(i)}\right]$$

at radial node $r_{\langle j+1 \rangle}^{c-s(i)}$.

The number of equations contained in the simultaneous linear system is $2c$ where c is the number of radial sections in axial section *(i)* of the cladding. These equations have $2c+1$ unknown variables ($2c$ integral constants and one axial strain), so an additional equation is needed for a determined system. Similarly to the fuel model, the additional equation can be obtained from the axial boundary condition at axial section *(i)* of the cladding (Equation 2.119). Applying the axial boundary condition to the solution for the axial stress in axial section *(i)* yields

$$\sum_{j=1}^{c}\left[F_{\delta r}^{c-s\langle j\rangle s(i)}C_{1}^{c-s\langle j\rangle s(i)}\right]+\sum_{j=1}^{c}\left[G_{\delta r}^{c-s\langle j\rangle s(i)}\right]C_{z}^{c-s(i)}=$$

$$-\frac{1}{2}\left(r_{\langle c+1\rangle}^{c-s(i)}\right)^{2}P_{cool}+\frac{1}{2}\left(r_{\langle 1\rangle}^{c-s(i)}\right)^{2}P_{plenum}-\frac{1}{2\pi}\sum_{n=i+1}^{N}W_{t}^{c-s(n)}-\sum_{j=1}^{c}\left[H_{\delta r}^{c-s\langle j\rangle s(i)}\right] \quad (2.142)$$

$$-\sum_{j=1}^{c}\left[a^{c-s\langle j\rangle s(i)}b^{c-s\langle j\rangle s(i)}\left(r_{\langle j+1\rangle}^{c-s(i)}W_{\langle j+1\rangle}^{c-s\langle j\rangle s(i)}-r_{\langle j\rangle}^{c-s(i)}W_{\langle j\rangle}^{c-s\langle j\rangle s(i)}\right)\right]$$

When Equation 2.142 is added to the simultaneous linear system, it eventually forms a determined system which contains $2c+1$ equations and $2c+1$ unknown variables. The system can be treated with the Gaussian elimination method or the successive over-relaxation (SOR) method.

2.2.4. Mechanical Response Models under Closed-Gap Condition

The mechanical response models for the closed-gap situation are obtained from determining the axial strain and integral constants by using the closed-gap boundary conditions. Applying the radial boundary conditions in the closed-gap situation to the solutions for the radial displacement and radial stress in axial section *(i)* of the fuel and cladding gives simultaneous linear systems comparable with those in the application of the open-gap boundary conditions. However, in the closed-gap situation, the fuel-cladding-interfacial conditions (Equation 2.120 and 2.121) are employed instead of the radial boundary conditions at the outer surface of fuel and the inner surface of cladding (Equations 2.111 and 2.114). Thus, the equation derived at the last radial node in axial section *(i)* of the fuel (Equation 2.132) should be replaced with

87

$$a^{f-s\langle f\rangle s(i)}\left(1+2b^{f-s\langle f\rangle s(i)}\right)C_1^{f-s\langle f\rangle s(i)} - \frac{a^{f-s\langle f\rangle s(i)}}{\left(r_{\langle f+1\rangle}^{f-s(i)}\right)^2}C_2^{f-s\langle f\rangle s(i)}$$

$$+\, a^{f-s\langle f\rangle s(i)}b^{f-s\langle f\rangle s(i)}C_z^{f-s(i)} \qquad (2.143)$$

$$= -P_{contact}^{s(i)} - a^{f-s\langle f\rangle s(i)}\left[\left(1+2b^{f-s\langle f\rangle s(i)}\right)X_{\langle f+1\rangle}^{f-s\langle f\rangle s(i)} - b^{f-s\langle f\rangle s(i)}m^{f-s\langle f\rangle s(i)}\right]$$

$$-\, a^{f-s\langle f\rangle s(i)}\left[b^{f-s\langle f\rangle s(i)}c^{f-s\langle f\rangle s(i)} + d_r^{f-s\langle f\rangle s(i)}\right]$$

in the simultaneous linear system of the fuel region. Also, the equation derived at the first radial node in axial section *(i)* of the cladding (Equation 2.136) must be changed to

$$a^{c-s\langle 1\rangle s(i)}\left(1+2b^{c-s\langle 1\rangle s(i)}\right)C_1^{c-s\langle 1\rangle s(i)} - \frac{a^{c-s\langle 1\rangle s(i)}}{\left(r_{\langle 1\rangle}^{c-s(i)}\right)^2}C_2^{c-s\langle 1\rangle s(i)}$$

$$+\, a^{c-s\langle 1\rangle s(i)}b^{c-s\langle 1\rangle s(i)}C_z^{c-s(i)} \qquad (2.144)$$

$$= -P_{contact}^{s(i)} - a^{c-s\langle 1\rangle s(i)}\left[\left(1+2b^{c-s\langle 1\rangle s(i)}\right)X_{\langle 1\rangle}^{c-s\langle 1\rangle s(i)} - b^{c-s\langle 1\rangle s(i)}m^{c-s\langle 1\rangle s(i)}\right]$$

$$-\, a^{c-s\langle 1\rangle s(i)}\left[b^{c-s\langle 1\rangle s(i)}c^{c-s\langle 1\rangle s(i)} + d_r^{c-s\langle 1\rangle s(i)}\right]$$

in the simultaneous linear system of the cladding region.

In the case of the closed gap, the simultaneous linear equations of the fuel and the cladding are merged into an integrated system for the calculation of the integral constants and axial strains. The merged simultaneous linear system consists of $2(f+c)-1$ equations ($2f-1$ equations from the fuel region and $2c$ equations from the cladding region), which contain $2(f+c)+1$ unknown variables ($2f$ variables in the fuel equations and $2c+1$ variables in the cladding equations). Like the simultaneous linear systems of the open-gap situation, additional equations are given from the axial boundary conditions at axial section *(i)* of the fuel and cladding (Equation 2.122 and 2.123):

$$\sum_{j=1}^{f}\left[F_{\delta r}^{f-s\langle j\rangle s(i)}C_1^{f-s\langle j\rangle s(i)}\right]+\sum_{j=1}^{f}\left[G_{\delta r}^{f-s\langle j\rangle s(i)}\right]C_z^{f-s(i)}=$$

$$-\frac{1}{2}\left[\left(r_{\langle f+1\rangle}^{f-s(i)}\right)^2-\left(r_{\langle 1\rangle}^{f-s(i)}\right)^2\right]P_{plenum}-\frac{1}{2\pi}\sum_{n=i+1}^{N}W_t^{f-s(n)}-\frac{1}{2\pi}\sum_{n=i}^{N}F_f^{s(n)} \qquad (2.145)$$

$$-\sum_{j=1}^{f}\left[H_{\delta r}^{f-s\langle j\rangle s(i)}\right]-\sum_{j=1}^{f}\left[a^{f-s\langle j\rangle s(i)}b^{f-s\langle j\rangle s(i)}\left(r_{\langle j+1\rangle}^{f-s(i)}W_{\langle j+1\rangle}^{f-s\langle j\rangle s(i)}-r_{\langle j\rangle}^{f-s(i)}W_{\langle j\rangle}^{f-s\langle j\rangle s(i)}\right)\right]$$

by the application of the axial boundary condition to the solution for the axial stress in axial section *(i)* of the fuel, and

$$\sum_{j=1}^{c}\left[F_{\delta r}^{c-s\langle j\rangle s(i)}C_1^{c-s\langle j\rangle s(i)}\right]+\sum_{j=1}^{c}\left[G_{\delta r}^{c-s\langle j\rangle s(i)}\right]C_z^{c-s(i)}=$$

$$-\frac{1}{2}\left(r_{\langle c+1\rangle}^{c-s(i)}\right)^2P_{cool}+\frac{1}{2}\left(r_{\langle 1\rangle}^{c-s(i)}\right)^2P_{plenum}-\frac{1}{2\pi}\sum_{n=i+1}^{N}W_t^{c-s(n)}+\frac{1}{2\pi}\sum_{n=i}^{N}F_f^{s(n)} \qquad (2.146)$$

$$-\sum_{j=1}^{c}\left[H_{\delta r}^{c-s\langle j\rangle s(i)}\right]-\sum_{j=1}^{c}\left[a^{c-s\langle j\rangle s(i)}b^{c-s\langle j\rangle s(i)}\left(r_{\langle j+1\rangle}^{c-s(i)}W_{\langle j+1\rangle}^{c-s\langle j\rangle s(i)}-r_{\langle j\rangle}^{c-s(i)}W_{\langle j\rangle}^{c-s\langle j\rangle s(i)}\right)\right]$$

by the application of the axial boundary condition to the solution for the axial stress in axial section *(i)* of the cladding.

When Equation 2.145 and 2.146 are added into the merged simultaneous linear system, it can be a determined system. However, the contact pressure and the friction force are still unknowns in the simultaneous equations. As explained in SECTION 2.2.2, the fuel-cladding-interfacial pressure and the friction force can be determined by the contact conditions of axial section *(i)* (Equation 2.124 and 2.125). Applying the contact conditions to the solutions for the radial displacement in axial section *(i)* yields

$$r_{\langle f+1\rangle}^{f-s(i)}C_1^{f-s\langle f\rangle s(i)}+\frac{1}{r_{\langle f+1\rangle}^{f-s(i)}}C_2^{f-s\langle f\rangle s(i)}-r_{\langle 1\rangle}^{c-s(i)}C_1^{c-s\langle 1\rangle s(i)}-\frac{1}{r_{\langle 1\rangle}^{c-s(i)}}C_2^{c-s\langle 1\rangle s(i)}$$

$$(2.147)$$

$$=W_{\langle 1\rangle}^{c-s\langle 1\rangle s(i)}-\left[u_{r-in}^{c-s(i)}\right]_{contact}-W_{\langle f+1\rangle}^{f-s\langle f\rangle s(i)}+\left[u_{r-out}^{f-s(i)}\right]_{contact}$$

Also, applying the contact conditions to the solutions for the axial displacement in axial

section *(i)* gives

$$
\begin{aligned}
C_z^{f-s(i)} \left(z_{(i+1)}^f - z_{(i)}^f \right) &- C_z^{c-s(i)} \left(z_{(i+1)}^c - z_{(i)}^c \right) \\
&= u_{z(i)}^{c-s(i-1)} - \left[u_{z(i+1)}^{c-s(i)} \right]_{contact} - u_{z(i)}^{f-s(i-1)} + \left[u_{z(i+1)}^{f-s(i)} \right]_{contact}
\end{aligned}
\tag{2.148}
$$

Equation 2.147 and 2.148 are included into the simultaneous linear system, and it finally

has $2(f+c)+3$ equations and $2(f+c)+3$ unknown variables. The coefficient matrix

can be treated with the Gaussian elimination method or the successive over-relaxation

(SOR) method for computing the integral constants, axial strains, contact pressure, and

friction force.

3. DEVELOPMENT OF TAMU-ZFP

Thermo-mechanical behaviors of metallic fuels are closely connected with one another under a wide variety of irradiation histories. In most cases, each individual behavior cannot be evaluated by considering its own physical phenomena in isolation. Due to the high degree of interconnection among the fuel behaviors, the models that predict and quantify the fuel behaviors contain nonlinear mathematical expressions, and the coefficients and boundary conditions of each model are dependent on the calculations of other models. These complex relations generally require an integrated platform which has high-performance computing capabilities to handle the fuel behavior models simultaneously. The TAMU-ZFP code that has been developed in this research was designed to provide an optimized platform where each model can communicate with other models to calculate the synergistic effects of the fuel behaviors. This section summarizes the structure of TAMU-ZFP and its solution schemes.

3.1. Code Structure

TAMU-ZFP consists of five major packages: code operation package, thermal analysis package, mechanical analysis package, materials data package, loop operation package. A package is basically a collection of correlated code-modules, and hence each package includes several modules as shown in Table 3.1. A module also contains stand-alone functions that execute specific computations for the module.

Table 3.1. Major packages and their modules in the TAMU-ZFP code.

Package	Module	Module description
Code operation package	TAMU-ZFP_main: main driver module	Includes functions for initiation of programs, case setup, declaration of code variables, control of basal loops, and termination of programs.
	In_TOOL: internal tools module	Includes functions for allocating and returning heap memories and copying user-defined data-type variables.
	Read_IN: input-processing module	Includes functions for reading user-specified input.
	Print_OUT: output-processing module	Includes functions for printing code output.
	Nu_TOOL: numerical tools module	Includes functions for numerical tools related to average, integration, augmented matrix, etc.
	Glob_INFO: global information module	Includes functions for initialization of code variables, dynamic dimensioning, and calculations of global data such as time, burnup, and local LHGR and VHGR.
Thermal analysis package	Therm_ST: steady-state thermal analysis module for fuel regions	Includes functions for calculations of steady-state temperature distributions in fuel regions and associated coolant channel.
	Therm_ST_BK: steady-state thermal analysis module for blanket regions	Includes functions for calculations of steady-state temperature distributions in upper/lower blanket regions and associated coolant channel.
	Therm_TR: transient thermal analysis module for fuel regions	Includes functions for calculations of transient temperature distributions in fuel regions and associated coolant channel.
	Therm_TR_BK: transient thermal analysis module for blanket regions	Includes functions for calculations of transient temperature distributions in upper/lower blanket regions and associated coolant channel.
Mechanical analysis package	Mech_OG: mechanical analysis module for fuel regions in open-gap situation	Includes functions for calculations of stress-strain distributions in fuel regions under open-gap condition.
	Mech_OG_BK: mechanical analysis module for blanket regions in open-gap situation	Includes functions for calculations of stress-strain distributions in upper/lower blanket regions under open-gap condition.
	Mech_PC: mechanical analysis module for fuel regions in partial-contact situation	Includes functions for calculations of stress-strain distributions in fuel regions under partial-contact condition.

Table 3.1. Continued.

Package	Module	Module description
	Mech_PC_BK: mechanical analysis module for blanket regions in partial-contact situation	Includes functions for calculations of stress-strain distributions in upper/lower blanket regions under partial-contact condition.
	Mech_CC: mechanical analysis module for fuel regions in complete-contact situation	Includes functions for calculations of stress-strain distributions in fuel regions under complete-contact condition.
	Mech_CC_BK: mechanical analysis module for blanket regions in complete-contact situation	Includes functions for calculations of stress-strain distributions in upper/lower blanket regions under complete-contact condition.
Materials data package	Mat_PRO: materials properties module	Includes functions providing thermal, mechanical, and physical properties data.
	Swell_FGR: swelling and FGR module	Includes function for calculations of fission gas release, gas swelling, void swelling, and swelling strain.
	Creep: creep module	Includes functions for calculations of thermal creep rates, irradiation creep rate, and creep strain in three principal directions
Loop operation package	Gas_PRESS: gas pressure module	Includes functions embodying gas-pressure convergence loop
	Opn_GAP: open-gap algorithm module	Includes functions constituting iterative loops used in open-gap algorithm
	Ser_CON: serial-contact algorithm module	Includes functions constituting iterative loops used in serial-contact algorithm
	Ran_CON: random-contact algorithm module	Includes functions constituting iterative loops used in random-contact algorithm

3.1.1. Packages and Modules

The code operation package performs the initiation and termination of programs, case setup, input/output processing, declaration and initialization of code-variables, and control of basal loops. It also carries out dynamic dimensioning and calculations of global data which are commonly utilized for various modules in the TAMU-ZFP code. The thermal

93

analysis package computes the temperature distributions in a fuel pin and single coolant channel. The package includes modules for transient temperature calculations.

The mechanical analysis package conducts stress-strain simulations which predict the stress distributions in the fuel pin of interest and the net strains of the fuel and cladding by irradiation time. The simulations selectively use three kinds of modules, depending on the state of gap: open-gap modules (Mech_OG/Mech_OG_BK), partial-contact modules (Mech_PC/Mech_PC_BK), and complete-contact modules (Mech_CC/Mech_CC_BK). The complete contact indicates a situation where the outer surface of the fuel is in contact with the inner surface of the cladding at all the axial sections. In the partial-contact situation, some axial sections have the closed gap, and the other axial sections have the open gap. While the mechanical models in the open-gap modules exploit open-gap boundary conditions (Equation 2.110 to 2.119), the models in the partial-contact modules adopt the following equations as the radial boundary conditions at the outer surface of the fuel and the inner surface of the cladding:

Radial boundary conditions for axial sections having open gap ($i < k$)

$$\sigma_r^{f-s\langle f\rangle s(i)}\left(r\right)\Big|_{r=r_{\langle f+1\rangle}^{f-s(i)}}=-P_{plenum} \tag{3.1}$$

$$\sigma_r^{c-s\langle 1\rangle s(i)}\left(r\right)\Big|_{r=r_{\langle 1\rangle}^{c-s(i)}}=-P_{plenum} \tag{3.2}$$

Radial boundary conditions for axial sections having closed gap ($i \geq k$)

$$\sigma_r^{f-s\langle f\rangle s(i)}\left(r\right)\Big|_{r=r_{\langle f+1\rangle}^{f-s(i)}}=-P_{contact}^{s(i)} \tag{3.3}$$

$$\sigma_r^{c-s\langle 1\rangle s(i)}\left(r\right)\Big|_{r=r_{\langle 1\rangle}^{c-s(i)}}=-P_{contact}^{s(i)} \tag{3.4}$$

where axial section *(i)* is an arbitrary axial section, and axial section *(k)* is the lowest axial section among the axial sections having the closed gap. The axial boundary conditions for the partial-contact modules are

Axial boundary conditions for axial sections having open gap $(i < k)$

$$\int_{r^{f-s(i)}_{\langle 1 \rangle}}^{r^{f-s(i)}_{\langle f+1 \rangle}} \sigma_z^{f-s(i)}(r) \cdot 2\pi r dr =$$
$$-\pi \left[\left(r^{f-s(i)}_{\langle f+1 \rangle} \right)^2 - \left(r^{f-s(i)}_{\langle 1 \rangle} \right)^2 \right] P_{plenum} - \sum_{n=i+1}^{N} W_t^{f-s(n)} - \sum_{n=k}^{N} F_f^{s(n)} - F_{f-open} \tag{3.5}$$

$$\int_{r^{c-s(i)}_{\langle 1 \rangle}}^{r^{c-s(i)}_{\langle c+1 \rangle}} \sigma_z^{c-s(i)}(r) \cdot 2\pi r dr =$$
$$-\pi \left(r^{c-s(i)}_{\langle c+1 \rangle} \right)^2 P_{cool} + \pi \left(r^{c-s(i)}_{\langle 1 \rangle} \right)^2 P_{plenum} - \sum_{n=i+1}^{N} W_t^{c-s(n)} + \sum_{n=k}^{N} F_f^{s(n)} + F_{f-open} \tag{3.6}$$

Axial boundary conditions for axial section *(k)*

$$\int_{r^{f-s(k)}_{\langle 1 \rangle}}^{r^{f-s(k)}_{\langle f+1 \rangle}} \sigma_z^{f-s(k)}(r) \cdot 2\pi r dr =$$
$$-\pi \left[\left(r^{f-s(k)}_{\langle f+1 \rangle} \right)^2 - \left(r^{f-s(k)}_{\langle 1 \rangle} \right)^2 \right] P_{plenum} - \sum_{n=k+1}^{N} W_t^{f-s(n)} - \sum_{n=k}^{N} F_f^{s(n)} - F_{f-open} \tag{3.7}$$

$$\int_{r^{c-s(k)}_{\langle 1 \rangle}}^{r^{c-s(k)}_{\langle c+1 \rangle}} \sigma_z^{c-s(k)}(r) \cdot 2\pi r dr =$$
$$-\pi \left(r^{c-s(k)}_{\langle c+1 \rangle} \right)^2 P_{cool} + \pi \left(r^{c-s(k)}_{\langle 1 \rangle} \right)^2 P_{plenum} - \sum_{n=k+1}^{N} W_t^{c-s(n)} + \sum_{n=k}^{N} F_f^{s(n)} + F_{f-open} \tag{3.8}$$

Axial boundary conditions for axial sections having closed gap $(i > k)$

$$\int_{r^{f-s(i)}_{\langle 1 \rangle}}^{r^{f-s(i)}_{\langle f+1 \rangle}} \sigma_z^{f-s(i)}(r) \cdot 2\pi r dr =$$
$$-\pi \left[\left(r^{f-s(i)}_{\langle f+1 \rangle} \right)^2 - \left(r^{f-s(i)}_{\langle 1 \rangle} \right)^2 \right] P_{plenum} - \sum_{n=i+1}^{N} W_t^{f-s(n)} - \sum_{n=i}^{N} F_f^{s(n)} \tag{3.9}$$

95

$$\int_{r_{\langle 1\rangle}^{c-s(i)}}^{r_{\langle c+1\rangle}^{c-s(i)}} \sigma_z^{c-s(i)}(r) \cdot 2\pi r dr =$$

$$-\pi \left(r_{\langle c+1\rangle}^{c-s(i)} \right)^2 P_{cool} + \pi \left(r_{\langle 1\rangle}^{c-s(i)} \right)^2 P_{plenum} - \sum_{n=i+1}^{N} W_t^{c-s(n)} + \sum_{n=i}^{N} F_f^{s(n)}$$

(3.10)

where F_{f-open} is the friction force induced by the deformation of the axial sections having the open gap, and it acts vertically on axial section *(k)* and all of the axial sections having the open gap. F_{f-open} has a positive value in Equations 3.5 to 3.8 when it restricts axial growth of the fuel. The contact pressure and friction forces are yet to be determined. The friction force F_{f-open} is obtained from the following contact condition:

$$u_z^{f-s(k-1)}(z)\Big|_{z=z_{(k)}^f} - \left[u_z^{f-s(k-1)}(z)\Big|_{z=z_{(k)}^f} \right]_{contact}$$

$$= u_z^{c-s(k-1)}(z)\Big|_{z=z_{(k)}^c} - \left[u_z^{c-s(k-1)}(z)\Big|_{z=z_{(k)}^c} \right]_{contact}$$

(3.11)

where axial section *(k-1)* is the top axial section among the axial sections having the open gap. The contact pressure $P_{contact}^{s(i)}$ and the friction force F_f can be calculated by using Equation 2.124 and 2.125. The boundary conditions for the partial-contact modules take account of only the serial-contact case, which will be discussed in section 3.2. The mechanical models in the complete-contact modules employ the fuel-cladding-interfacial conditions which are represented in Equation 2.120 to 2.123.

The materials data package deals with the variables whose values are dependent on the types of materials. The package consists partly of simple data on thermal, mechanical, and physical properties. The other parts of the package involve behavior models which compute the rates of particular processes (e.g., fission-gas-induced swelling

and creep). The scope of this research does not include the implementation of the behavior models, and hence the package was structured to deliver code default data for the variables requiring the behavior models. The loop operation package runs and controls iterative loops included in three main algorithms of the TAMU-ZFP code: open-gap algorithm, serial-contact algorithm, and random-contact algorithm. The details of these algorithms will be explained in section 3.2.

3.1.2. Input and Output

The TAMU-ZFP code predicts thermo-mechanical responses of a metallic fuel pin according to the fuel pin designs and reactor-operation history which are given in a user-specified input. The input variables of TAMU-ZFP are divided into three groups: case control integers, fuel pin designs, and reactor operation data. Table 3.2 lists the input variables in each group.

Table 3.2. Input variables of the TAMU-ZFP code.

Input variable group	Input variable	Variable description
Case control integers	timestep	Number of time steps
	transient	Time step when the transient starts; transient = 0 means steady-state only.
	tdependency_cool	Time-dependency indicator of thermal-hydraulic parameters
	axsection_fuel	Number of axial sections in the fuel slug region
	axsection_upb	Number of axial sections in the upper blanket region
	axsection_lob	Number of axial sections in the lower blanket region
	axpshape	Indicator for axial power shape
	num_axprofiles	Number of user-supplied axial power profiles
	cladtype	Indicator for the type of cladding

Table 3.2. Continued.

Input variable group	Input variable	Variable description
Fuel pin designs	wtpct_pu	Weight percent of plutonium in alloy fuel (wt% Pu)
	wtpct_zr	Weight percent of zirconium in alloy fuel (wt% Zr)
	smearden	Smeared density of fuel (%TD)
	fradi	Radius of fuel slug
	cladthi	Thickness of cladding
	gapthi	Thickness of gap
	fuelen	Length of fuel slug (or length of a stack of fuel pellets)
	upblen	Length of upper blanket
	loblen	Length of lower blanket
	plenmlen	Length of gas plenum
	plenm_ipress	Initial pressure of helium in gas plenum
	sod_level	Upper sodium level
	pin_pitch	Fuel pin pitch (center-to-center distance between pins in a triangular coolant channel)
Reactor operation data	time	Array for cumulative time at the end of each time step
	lhgr	Array for average linear heat generation rate at each time
	inlet_temp	Array for coolant inlet temperature at each time step
	cmflow	Array for coolant mass flow rate at each time step
	cool_press	Array for coolant pressure at each time step
	hist_axpro	Array for index of axial power profile used for each time step
	axpro	Array for the ratios of the linear power at each axial node to the axially-averaged value

Basically, the fuel pin design parameters such as dimensions of the fuel slug and cladding, fuel composition, and smeared density are provided in the input by the code user. The fuel smeared density is used in the following equation to calculate the as-cast fuel density:

$$\rho_A = \frac{SD}{100} \left(\frac{r_g}{r_f} \right)^2 \rho_T \qquad (3.12)$$

where ρ_A = as-cast fuel density [g/cm^3]

SD = smeared density [%TD]

r_f = radius of the as-fabricated fuel [cm]

r_g = radius up to the inner surface of the as-fabricated cladding [cm]

ρ_T = theoretical density of the fuel at room temperature [g/cm^3] (in the case of U-

10 wt% Zr, ρ_T is 16.31 [28,29]).

The computed as-fabricated density is also used in the following equation to obtain the

initial porosity of the fuel:

$$p_0 = 100\left(1 - \frac{\rho_A}{\rho_T}\right) \tag{3.13}$$

where p_0 = porosity of the as-fabricated fuel [%].

In the input, the code user can specify the linear heat generation rates as a

piecewise-linear function of z and a piecewise-constant function of t for the steady-state

case. For the transient case, the user-supplied linear heat generation rates are given as a

piecewise-bilinear function of z and t in the input. The code also provides a default axial

power profile which is based on a chopped cosine function. The thermal-hydraulic

parameters such as coolant inlet temperature, mass flow rate, and coolant pressure are

given in the input as a piecewise-constant function of t for both of the steady-state and

transient. More details of the input instructions of the TAMU-ZFP code is represented in

APPENDIX C.

(a)
```
===============================================================================


               Tool for Analyzing Metallic U-Zr Fuel Performance

                              (TAMU-ZFP)


          Developed by :  Hyocheol Lee and Pavel V. Tsvetkov
                          Department of Nuclear Engineering
                          Texas A&M University
          Version       :  1.0
          Date          :  October 2018



===============================================================================



Input File :  user_tdc.inp
Current Date and Time :  Tue Aug 27 21:52:01 2019




[Summary of Input]


***** Case Control Integers ************************

timestep        20                     transient        0              tdependency_cool 1
axsection_fuel  6                      axsection_upb    2              axsection_lob    2
axpshape        2                      num_axprofiles   3              cladtype         4


***** Fuel Pin Designs ****************************

fradi[cm]       0.245745               cladthi[cm]      0.038100       gapthi[cm]       0.008255
fuelen[cm]      91.440000              upblen[cm]       35.560000      loblen[cm]       35.560000
plenmlen[cm]    121.920000             sodlevel[cm]     2.000000       pin_pitch[cm]    0.736600
wtpct_zr[wt%]   10.000000              wtpct_pu[wt%]    0.000000       smearden[%TD]    75.000000


***** Reactor Operation Data ***********************

time[day]
        0.100000          0.200000          0.300000          1.000000          2.000000
        3.000000         10.000000         20.000000         50.000000         60.000000
       80.000000        100.000000        150.000000        200.000000        250.000000
      300.000000        350.000000        400.000000        450.000000        500.000000
lhgr[W/cm]
      117.093107        117.093107        117.093107        117.093107        117.093107
      117.093107        117.093107        117.093107        117.093107        117.093107
      117.093107        117.093107        117.093107        117.093107        117.093107
      117.093107        117.093107        117.093107        117.093107        117.093107
inlet_temp[C]
      388.000000        388.000000        388.000000        388.000000        388.000000
      388.000000        388.000000        388.000000        388.000000        388.000000
      388.000000        388.000000        388.000000        388.000000        388.000000
      388.000000        388.000000        388.000000        388.000000        388.000000
cmflow[g/s]
       48.679493         48.679493         48.679493         48.679493         48.679493
```

Figure 3.1. An example of TAMU-ZFP output. (a) Output starts with a summary of the input. (b) Output shows calculation results by the axial section of a time-step.

(b) [Time Step 1]

```
----------------------- Axial Section  1 -----------------------

average LHGR of entire fuel-pin [W/cm]         117.093107        height of bottom of axial section, z1  [cm]       0.000000
local average-LHGR at axial section [W/cm]      71.723272        height of top of axial section, z2  [cm]         17.918931
average LHGR at peak axial-section [W/cm]      149.445437        length of axial section [cm]                     17.918931

average VHGRs at axial section [W/cm^3]        372.203263        state of local gap at axial section (open/closed):   open
local fuel-pin-surface heat flux [W/(cm^2]      38.902626        gap conductance at axial section [W/(cm^2)-K]   89.459526
convective heat transfer coeff. [W/(cm^2)-K]    37.336326

time at beginning of time-step [days] (sec)   0.000 (0.000E+00)   burnup at beginning of time-step [MWd/MTU]        0.000000
time increment [days] (sec)                   0.100 (8.640E+03)   burnup increment [MWd/MTU]                        0.000000
time at end of time-step [days] (sec)         0.100 (8.640E+03)   burnup at end of time-step [MWd/MTU]              0.000000


                    radial distributions of temperature, power, and radial displacement

          radial node                       radius [cm]      temperature [K]      power ratio      radial displ. [cm]

          rf1    fuel    center               0.000000         690.232552          1.000000          0.000000
          rf2    fuel                         0.030962         690.034327          1.000000          0.000244
          rf3    fuel                         0.061923         689.439662          1.000000          0.000487
          rf4    fuel                         0.092884         688.448582          1.000000          0.000729
          rf5    fuel                         0.123843         687.061131          1.000000          0.000971
          rf6    fuel                         0.154802         685.277370          1.000000          0.001211
          rf7    fuel                         0.185758         683.097376          1.000000          0.001450
          rf8    fuel                         0.216713         680.521246          1.000000          0.001686
          rf9    fuel    outer surface        0.247665         677.549092          1.000000          0.001920

          rc1    cladding  inner surface      0.255155         677.041514                            0.001155
          rc2    cladding                     0.264724         674.495618                            0.001199
          rc3    cladding                     0.274292         672.040247                            0.001242
          rc4    cladding                     0.283860         669.669181                            0.001285
          rc5    cladding  outer surface      0.293428         667.376820                            0.001328

                 coolant                                       666.334868

axial node zf1  before axial displacement [cm]  0.000000        axial displacement of axial node zf1  [cm]        0.000000
axial node zf2  before axial displacement [cm] 17.780000        axial displacement of axial node zf2  [cm]        0.138931
axial node zc1  before axial displacement [cm]  0.000000        axial displacement of axial node zc1  [cm]        0.000000
axial node zc2  before axial displacement [cm] 17.837843        axial displacement of axial node zc2  [cm]        0.081088


                        radial distributions of solid-mechanics components

          radial section      radial stress [MPa]   hoop stress [MPa]   axial stress [MPa]   radial strain    angular strain

          fuel       1          -13.479364          -13.479364          -26.857402          0.007930          0.007930
          fuel       2          -13.022403          -12.237277          -25.158355          0.007919          0.007926
          fuel       3          -12.170834           -9.690827          -21.760336          0.007897          0.007918
          fuel       4          -10.896040           -5.868779          -16.663494          0.007864          0.007907
          fuel       5           -9.196889           -0.772487           -9.868052          0.007820          0.007893
          fuel       6           -7.073215            5.597583           -1.374307          0.007764          0.007874
          fuel       7           -4.525015           13.241057            8.817367          0.007698          0.007852
          fuel       8           -1.552338           22.157539           20.706525          0.007621          0.007826

          cladding   1           -0.295506          -10.587482          -10.781663          0.004625          0.004547
          cladding   2           -0.530184           -3.269222           -3.698081          0.004570          0.004549
          cladding   3           -0.506631            3.543287            3.137981          0.004518          0.004549
          cladding   4           -0.266313            9.908238            9.743251          0.004470          0.004547

axial strain of axial section in fuel        0.007814        axial strain of axial section in cladding        0.004546


                        ----------------------- Axial Section  2 -----------------------

average LHGR of entire fuel-pin [W/cm]         117.093107        height of bottom of axial section, z2  [cm]      17.918931
```

Figure 3.1. Continued.

TAMU-ZFP repeatedly prints out its calculation results by the axial section of a time-step as shown in Figure 3.1. This sectional information includes radial temperature distribution, coolant temperature, local power and burnup, radial stress distribution, and net strains of fuel and cladding. At the end of each time-step, the output shows information pertaining the entire fuel pin such as internal pressure and accumulated fraction of fission gas release. The output also provides a final summary of critical irradiation behaviors at the end of the last time-step. The TAMU-ZFP code is equipped with a 3D graphical tool for the visualization of the output. The tool was built on the MATLAB platform. Once the code generates raw data files, based on its calculation results, the graphical tool processes the raw data files for basic post-processing and visualization.

3.2. Calculation Schemes

Three new advanced algorithms were developed in this study: open-gap algorithm, serial-contact algorithm, and random-contact algorithm. TAMU-ZFP executes its computations by selectively following the three algorithms according to the state of the fuel-cladding gap. The open-gap algorithm contains two sub-algorithms: initial serial-contact time (ISCT) algorithm and completely-random-contact time (CRCT) algorithm. The serial-contact algorithm also has two sub-algorithms: continuous serial-contact time (CSCT) algorithm and partly-random-contact time (PRCT) algorithm. Figure 3.2 to 3.8 shows the three main algorithms and four sub-algorithms of the TAMU-ZFP code.
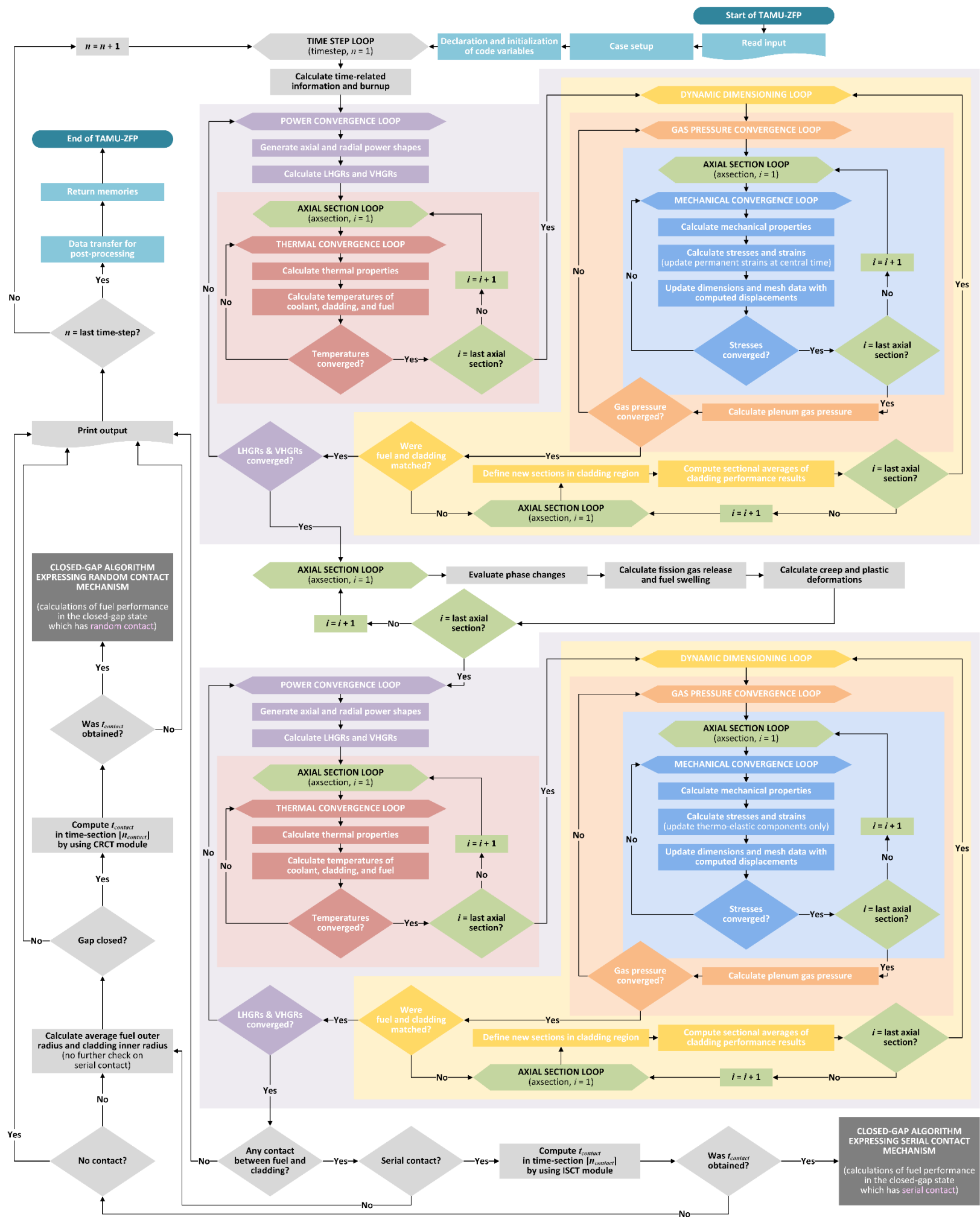
Figure 3.2. Flowchart of the open-gap algorithm.

Figure 3.3. Flowchart of the closed-gap algorithm expressing serial-contact mechanism (serial-contact algorithm).

TIME STEP LOOP
(timestep, $n = n_{contact}$)

Receive information on $t_{contact}$ and performance data at $t_{contact}$

OPEN-GAP ALGORITHM WITHOUT FURTHER CHECK ON SERIAL CONTACT

(calculations of fuel performance in open-gap state, no serial contact when gap is closed again)

Calculate time-related information and burnup

Calculate average fuel outer radius and cladding inner radius with open-gap algorithm

Gap opened?

Yes

No

GAS PRESSURE CONVERGENCE LOOP

FRICTION FORCE CONVERGENCE LOOP

POWER CONVERGENCE LOOP

Generate axial and radial power shapes

Calculate LHGRs and VHGRs

AXIAL SECTION LOOP
(axsection, $i = 1$)

MECHANICAL CONVERGENCE LOOP

Calculate mechanical properties

AXIAL SECTION LOOP
(axsection, $i = 1$)

THERMAL CONVERGENCE LOOP

Calculate thermal properties

Calculate temperatures of coolant, cladding, and fuel with closed-gap boundary conditions

Friction forces converged?

No

Yes

$i = i + 1$

Calculate stresses and strains with closed-gap boundary conditions (update permanent strains at central time)

Update dimensions and mesh data with computed displacements

$i = i + 1$

No

Temperatures converged?

No

Yes

i = last axial section?

Yes

i = last axial section?

No

Yes

Stresses converged?

No

Yes

Calculate plenum gas pressure

Gas pressure converged?

No

Yes

LHGRs & VHGRs converged?

No

Yes

AXIAL SECTION LOOP
(axsection, $i = 1$)

Evaluate phase changes

Calculate fission gas release and fuel swelling

Calculate creep and plastic deformations

$i = i + 1$

No

i = last axial section?

Yes

GAS PRESSURE CONVERGENCE LOOP

FRICTION FORCE CONVERGENCE LOOP

POWER CONVERGENCE LOOP

Generate axial and radial power shapes

Calculate LHGRs and VHGRs

AXIAL SECTION LOOP
(axsection, $i = 1$)

MECHANICAL CONVERGENCE LOOP

Calculate mechanical properties

AXIAL SECTION LOOP
(axsection, $i = 1$)

THERMAL CONVERGENCE LOOP

Calculate thermal properties

Calculate temperatures of coolant, cladding, and fuel with closed-gap boundary conditions

Friction forces converged?

No

Yes

$i = i + 1$

Calculate stresses and strains with closed-gap boundary conditions (update thermo-elastic components only)

Update dimensions and mesh data with computed displacements

$i = i + 1$

No

Temperatures converged?

No

Yes

i = last axial section?

Yes

i = last axial section?

No

Yes

Stresses converged?

No

Yes

Calculate plenum gas pressure

Gas pressure converged?

No

Yes

LHGRs & VHGRs converged?

No

Yes

$n = n + 1$

Print output

n = last time-step?

Yes

No

Data transfer for post-processing
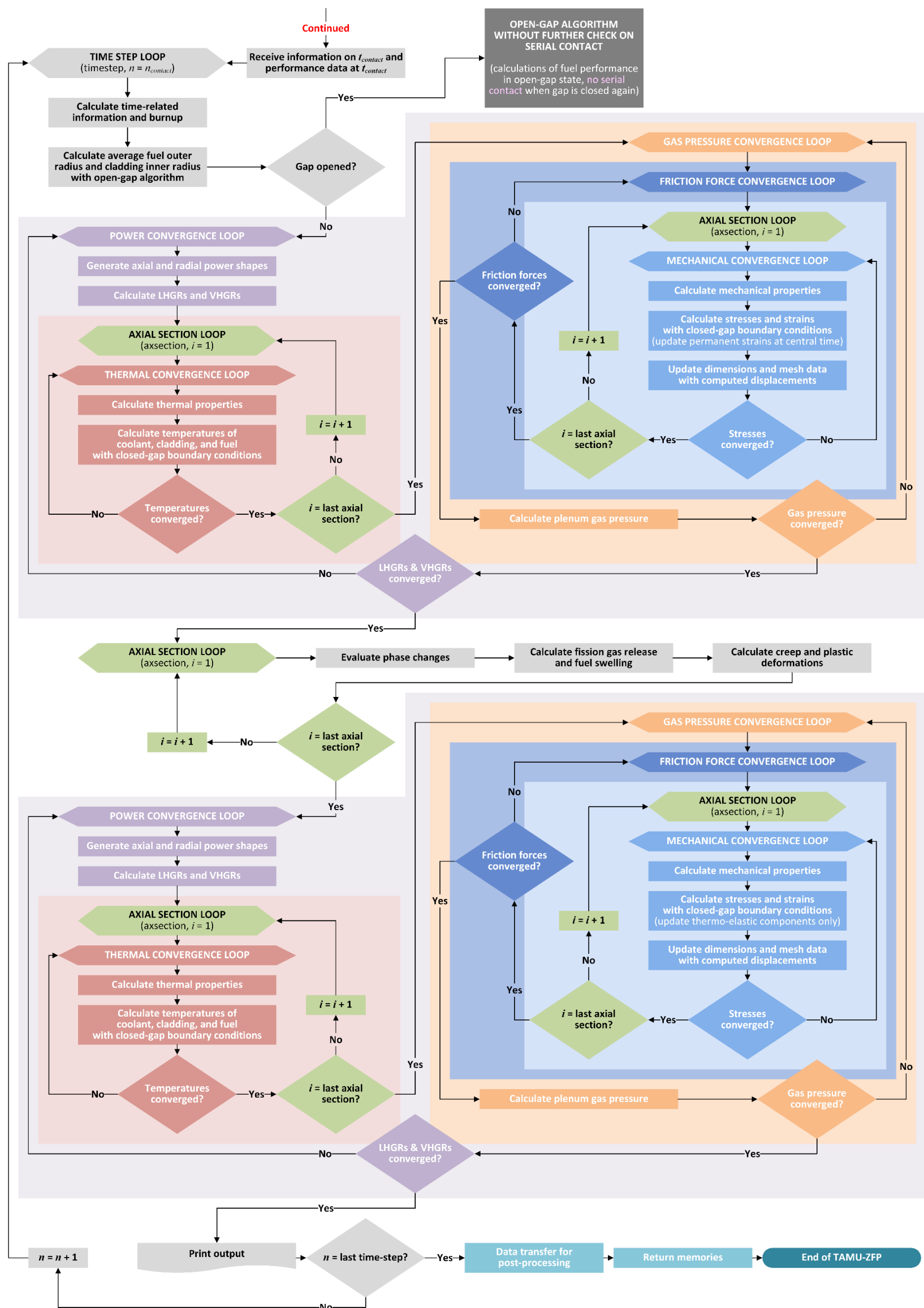
Return memories

End of TAMU-ZFP

Figure 3.4. Flowchart of the closed-gap algorithm expressing random-contact mechanism (random-contact algorithm).
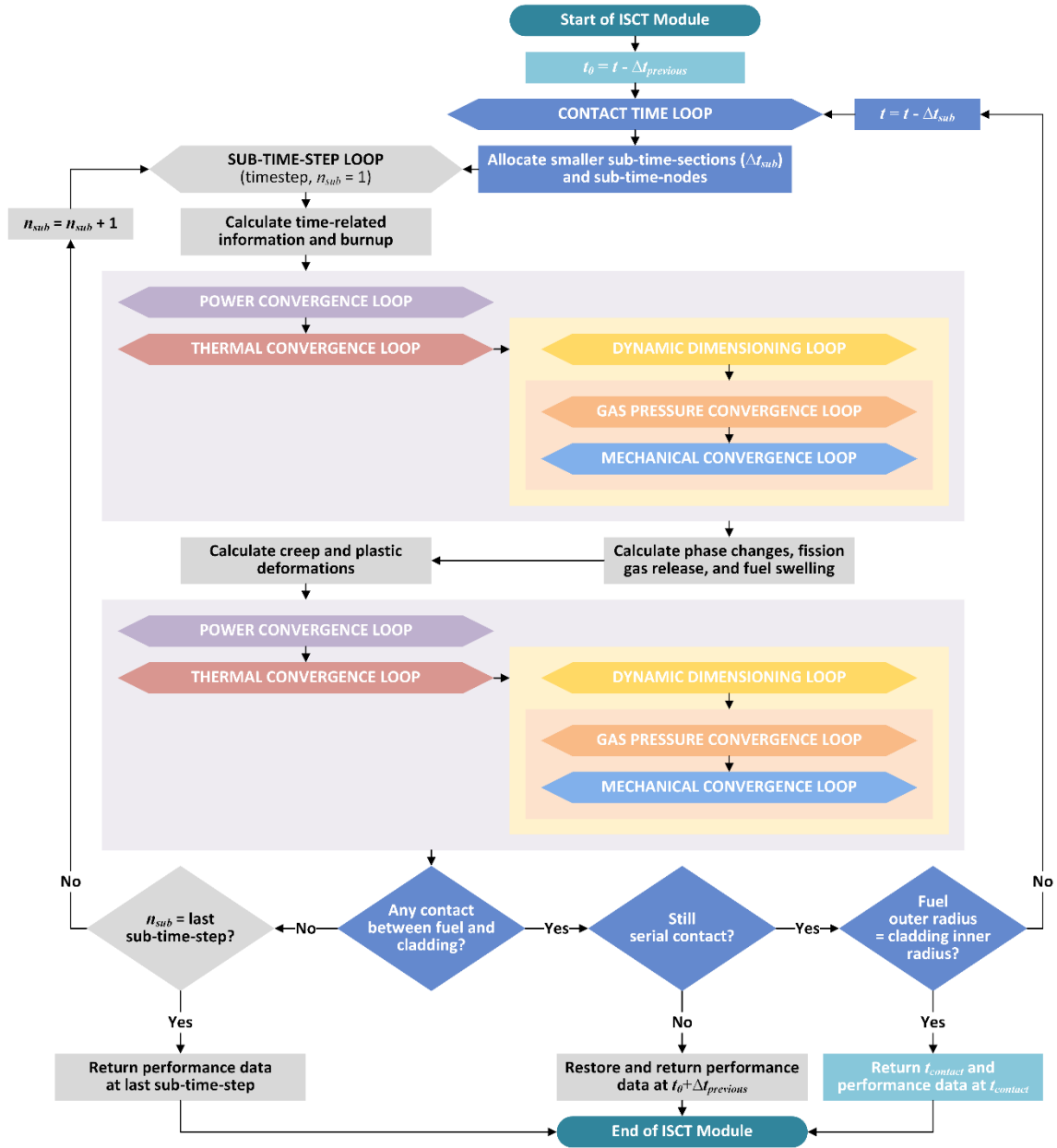
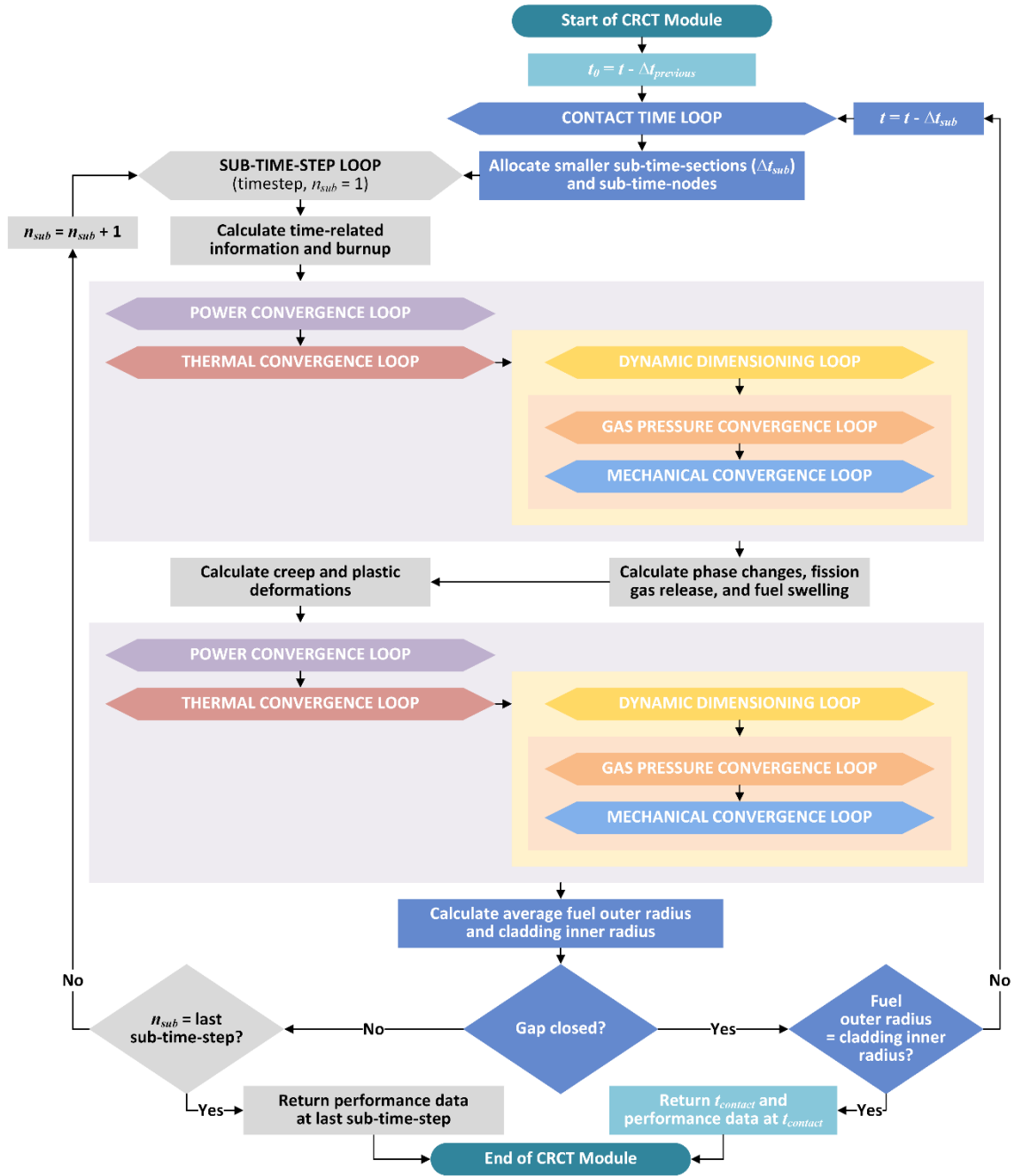Figure 3.5. Flowchart of the initial serial-contact time (ISCT) algorithm.

106

Figure 3.6. Flowchart of the completely-random-contact time (CRCT) algorithm.

Figure 3.7. Flowchart of the continuous serial-contact time (CSCT) algorithm.

Figure 3.8. Flowchart of the partly-random-contact time (PRCT) algorithm.

3.2.1. Main Algorithms and Sub-Algorithms

The programs starts with the open-gap algorithm. The open gap algorithm expresses a situation where all the axial sections have the open gap. The mechanical analysis of the open-gap algorithm is conducted by using the models in the open-gap modules (Mech_OG/Mech_OG_BK) as explained in section 3.1. Based on the results of the mechanical analysis, the code investigates a contact case that occurs when the fuel radius is larger than the radius up to the inner surface of the cladding. If the contact case happens to the top axial section, the code call the ISCT sub-algorithm. All the sub-algorithms of TAMU-ZFP are operated basically to calculate the exact time of the contact and the contact displacements in the radial and axial directions which are used in Equation 2.147 and 2.148. While the code is repeating its computations in the contact time loop of the sub-algorithms shown in Figure 3.5 to 3.8, the size of sub-time-step keeps being reduced to find out the exact contact-time. Once the time of the first serial-contact is obtained from the ISCT sub-algorithm, TAMU-ZFP follows the serial-contact algorithm for further calculations. If the contact case happens to any axial section other than the top axial section and the average radius of the fuel axial-sections is larger than the average radius of the inner surfaces of the cladding axial-sections, the code call the CRCT sub-algorithm. Once the contact time and the radial and axial contact-displacements are obtained from the CRCT sub-algorithm, the code follows the random-contact algorithm for further calculations.

The serial-contact algorithm describes a situation where the fuel-cladding contact happens serially from the top axial section to the bottom axial section. Before the contact

occurs in all the axial sections, some axial sections have the open gap and the other axial section have the closed gap. Therefore, the mechanical models in the partial-contact modules (Mech_PC/Mech_PC_BK) are employed for the stress-strain analysis. The code searches for a new contact at the end of each time-step, based on the stress-strain analysis. If a new contact is found at the axial section right below the axial sections having the closed gap, the code call the CSCT sub-algorithm to calculate the contact time and contact displacements of the axial section. If the additional contact is found at any axial section other than the continuous axial section and the average radius of the open fuel-axial-sections is larger than the average radius of the inner surfaces of the open cladding-axial-sections, the code call the PRCT sub-algorithm. Once the contact time and the radial and axial contact-displacements are obtained from the PRCT sub-algorithm, the code follows the random-contact algorithm for further calculations. The random-contact algorithm uses the mechanical models in the complete-contact modules (Mech_CC/Mech_CC_BK) because all the axial sections have the closed gap.

3.2.2. Iterative Loops

When the numerical equations of a fuel performance model are formulated implicitly[18], a variable at a node is influenced by the variables at the other nodes in the same computation-domain. Thus, the variables of the equations need to be determined by using

---

[18]The implementation of implicit methods is not limited to the realistic time-dependent behavior. It can be applied to a time-like process which is actually in steady state. As a matter of fact, the implementation of implicit methods for steady-state computations is more attractive because the number of iterations required for a solution is often much smaller than the number of time-steps needed for an accurate transient simulation that asymptotically approaches steady conditions.

a matrix (direct method) as explained in SECTION 2. The implicitly formulated numerical equations also entail nonlinearity which is induced by interrelation between fuel performance models or information propagation. The nonlinearity is typically represented as parameters in the equations. The estimation of the parameters should be coupled with the calculations in other fuel performance models or the calculations in other computation-domains. One of the most common and efficient way to handle the coupling is iterative techniques (iterative method). As shown in Figure 3.2 to 3.8, the algorithms of the TAMU-ZFP code contain eight kinds of iterative loops: time-step loop, power convergence loop, thermal convergence loop, dynamic dimensioning loop, gas-pressure convergence loop, friction-force convergence loop, mechanical convergence loop, and axial section loop.

In the thermal analysis, a temperature at a mesh-point is influenced by thermal properties at the mesh-point, but at the same time the thermal property models are functions of temperature. This nonlinearity is processed by the thermal convergence loop. Average stresses in a mesh-cell are calculated with accumulated permanent strains of the mesh-cell. However, the creep strain rate and swelling rate in the mesh-cell are reversely functions of the average stresses in the mesh-cell (i.e., average equivalent stress and average hydrostatic stress, respectively). The nonlinearity in the mechanical analysis is handled by the mechanical convergence loop.

The average stresses and average strains in a mesh-cell are obtained from the following equations:

$$
\sigma_r^{s\langle j\rangle s(i)} = \frac{\int_{r_{\langle j\rangle}^{s(i)}}^{r_{\langle j+1\rangle}^{s(i)}} \sigma_r^{s\langle j\rangle s(i)}(r)\cdot 2\pi r H^{s(i)} dr}{\pi\left(r_{\langle j+1\rangle}^{s(i)}\right)^2 H^{s(i)} - \pi\left(r_{\langle j\rangle}^{s(i)}\right)^2 H^{s(i)}} = \frac{2\int_{r_{\langle j\rangle}^{s(i)}}^{r_{\langle j+1\rangle}^{s(i)}} \sigma_r^{s\langle j\rangle s(i)}(r)\cdot r dr}{\left(r_{\langle j+1\rangle}^{s(i)}\right)^2 - \left(r_{\langle j\rangle}^{s(i)}\right)^2} \qquad (3.14)
$$

112

$$= a^{s\langle j\rangle s(i)}\left(1+2b^{s\langle j\rangle s(i)}\right)C_1^{s\langle j\rangle s(i)} - \frac{2a^{s\langle j\rangle s(i)}\ln\left(r_{\langle j+1\rangle}^{s(i)}\big/ r_{\langle j\rangle}^{s(i)}\right)}{\left(r_{\langle j+1\rangle}^{s(i)}\right)^2 - \left(r_{\langle j\rangle}^{s(i)}\right)^2}C_2^{s\langle j\rangle s(i)} + a^{s\langle j\rangle s(i)}b^{s\langle j\rangle s(i)}C_z^{s(i)}$$

$$+ a^{s\langle j\rangle s(i)}\left(1+2b^{s\langle j\rangle s(i)}\right)\frac{r_{\langle j+1\rangle}^{s(i)}W_{\langle j+1\rangle}^{s\langle j\rangle s(i)} - r_{\langle j\rangle}^{s(i)}W_{\langle j\rangle}^{s\langle j\rangle s(i)}}{\left(r_{\langle j+1\rangle}^{s(i)}\right)^2 - \left(r_{\langle j\rangle}^{s(i)}\right)^2} + \frac{1}{2}a^{s\langle j\rangle s(i)}m^{s\langle j\rangle s(i)}$$

$$+ a^{s\langle j\rangle s(i)}\left(b^{s\langle j\rangle s(i)}c^{s\langle j\rangle s(i)} + d_r^{s\langle j\rangle s(i)}\right)$$

$$\sigma_\theta^{s\langle j\rangle s(i)} = \frac{\int_{r_{\langle j\rangle}^{s(i)}}^{r_{\langle j+1\rangle}^{s(i)}} \sigma_\theta^{s\langle j\rangle s(i)}(r)\cdot 2\pi r H^{s(i)}dr}{\pi\left(r_{\langle j+1\rangle}^{s(i)}\right)^2 H^{s(i)} - \pi\left(r_{\langle j\rangle}^{s(i)}\right)^2 H^{s(i)}} = \frac{2\int_{r_{\langle j\rangle}^{s(i)}}^{r_{\langle j+1\rangle}^{s(i)}} \sigma_\theta^{s\langle j\rangle s(i)}(r)\cdot r dr}{\left(r_{\langle j+1\rangle}^{s(i)}\right)^2 - \left(r_{\langle j\rangle}^{s(i)}\right)^2}$$

$$= a^{s\langle j\rangle s(i)}\left(1+2b^{s\langle j\rangle s(i)}\right)C_1^{s\langle j\rangle s(i)} + \frac{2a^{s\langle j\rangle s(i)}\ln\left(r_{\langle j+1\rangle}^{s(i)}\big/ r_{\langle j\rangle}^{s(i)}\right)}{\left(r_{\langle j+1\rangle}^{s(i)}\right)^2 - \left(r_{\langle j\rangle}^{s(i)}\right)^2}C_2^{s\langle j\rangle s(i)} + a^{s\langle j\rangle s(i)}b^{s\langle j\rangle s(i)}C_z^{s(i)} \quad (3.15)$$

$$+ a^{s\langle j\rangle s(i)}\left(1+2b^{s\langle j\rangle s(i)}\right)\frac{r_{\langle j+1\rangle}^{s(i)}W_{\langle j+1\rangle}^{s\langle j\rangle s(i)} - r_{\langle j\rangle}^{s(i)}W_{\langle j\rangle}^{s\langle j\rangle s(i)}}{\left(r_{\langle j+1\rangle}^{s(i)}\right)^2 - \left(r_{\langle j\rangle}^{s(i)}\right)^2} - \frac{1}{2}a^{s\langle j\rangle s(i)}m^{s\langle j\rangle s(i)}$$

$$+ a^{s\langle j\rangle s(i)}\left(b^{s\langle j\rangle s(i)}c^{s\langle j\rangle s(i)} + d_\theta^{s\langle j\rangle s(i)}\right)$$

$$\sigma_z^{s\langle j\rangle s(i)} = \frac{\int_{r_{\langle j\rangle}^{s(i)}}^{r_{\langle j+1\rangle}^{s(i)}} \sigma_z^{s\langle j\rangle s(i)}(r)\cdot 2\pi r H^{s(i)}dr}{\pi\left(r_{\langle j+1\rangle}^{s(i)}\right)^2 H^{s(i)} - \pi\left(r_{\langle j\rangle}^{s(i)}\right)^2 H^{s(i)}} = \frac{2\int_{r_{\langle j\rangle}^{s(i)}}^{r_{\langle j+1\rangle}^{s(i)}} \sigma_z^{s\langle j\rangle s(i)}(r)\cdot r dr}{\left(r_{\langle j+1\rangle}^{s(i)}\right)^2 - \left(r_{\langle j\rangle}^{s(i)}\right)^2}$$

$$= 2a^{s\langle j\rangle s(i)}b^{s\langle j\rangle s(i)}C_1^{s\langle j\rangle s(i)} + a^{s\langle j\rangle s(i)}\left(1+b^{s\langle j\rangle s(i)}\right)C_z^{s(i)} \quad (3.16)$$

$$+ 2a^{s\langle j\rangle s(i)}b^{s\langle j\rangle s(i)}\frac{r_{\langle j+1\rangle}^{s(i)}W_{\langle j+1\rangle}^{s\langle j\rangle s(i)} - r_{\langle j\rangle}^{s(i)}W_{\langle j\rangle}^{s\langle j\rangle s(i)}}{\left(r_{\langle j+1\rangle}^{s(i)}\right)^2 - \left(r_{\langle j\rangle}^{s(i)}\right)^2} + a^{s\langle j\rangle s(i)}\left(b^{s\langle j\rangle s(i)}c^{s\langle j\rangle s(i)} + d_z^{s\langle j\rangle s(i)}\right)$$

$$\varepsilon_r^{s\langle j\rangle s(i)} = \frac{\int_{r_{\langle j\rangle}^{s(i)}}^{r_{\langle j+1\rangle}^{s(i)}} \varepsilon_r^{s\langle j\rangle s(i)}(r)\cdot 2\pi r H^{s(i)}dr}{\pi\left(r_{\langle j+1\rangle}^{s(i)}\right)^2 H^{s(i)} - \pi\left(r_{\langle j\rangle}^{s(i)}\right)^2 H^{s(i)}} = \frac{2\int_{r_{\langle j\rangle}^{s(i)}}^{r_{\langle j+1\rangle}^{s(i)}} \varepsilon_r^{s\langle j\rangle s(i)}(r)\cdot r dr}{\left(r_{\langle j+1\rangle}^{s(i)}\right)^2 - \left(r_{\langle j\rangle}^{s(i)}\right)^2}$$

$$\quad (3.17)$$

$$= C_1^{s\langle j\rangle s(i)} - \frac{2\ln\left(r_{\langle j+1\rangle}^{s(i)}\big/ r_{\langle j\rangle}^{s(i)}\right)}{\left(r_{\langle j+1\rangle}^{s(i)}\right)^2 - \left(r_{\langle j\rangle}^{s(i)}\right)^2}C_2^{s\langle j\rangle s(i)} + \frac{r_{\langle j+1\rangle}^{s(i)}W_{\langle j+1\rangle}^{s\langle j\rangle s(i)} - r_{\langle j\rangle}^{s(i)}W_{\langle j\rangle}^{s\langle j\rangle s(i)}}{\left(r_{\langle j+1\rangle}^{s(i)}\right)^2 - \left(r_{\langle j\rangle}^{s(i)}\right)^2} + \frac{1}{2}m^{s\langle j\rangle s(i)}$$

$$\varepsilon_\theta^{s\langle j\rangle s(i)} = \frac{\int_{r_{\langle j\rangle}^{s(i)}}^{r_{\langle j+1\rangle}^{s(i)}} \varepsilon_\theta^{s\langle j\rangle s(i)}(r) \cdot 2\pi r H^{s(i)} dr}{\pi\left(r_{\langle j+1\rangle}^{s(i)}\right)^2 H^{s(i)} - \pi\left(r_{\langle j\rangle}^{s(i)}\right)^2 H^{s(i)}} = \frac{2\int_{r_{\langle j\rangle}^{s(i)}}^{r_{\langle j+1\rangle}^{s(i)}} \varepsilon_\theta^{s\langle j\rangle s(i)}(r) \cdot r dr}{\left(r_{\langle j+1\rangle}^{s(i)}\right)^2 - \left(r_{\langle j\rangle}^{s(i)}\right)^2}$$

$$= C_1^{s\langle j\rangle s(i)} + \frac{2\ln\left(r_{\langle j+1\rangle}^{s(i)}/r_{\langle j\rangle}^{s(i)}\right)}{\left(r_{\langle j+1\rangle}^{s(i)}\right)^2 - \left(r_{\langle j\rangle}^{s(i)}\right)^2} C_2^{s\langle j\rangle s(i)} + \frac{r_{\langle j+1\rangle}^{s(i)} W_{\langle j+1\rangle}^{s\langle j\rangle s(i)} - r_{\langle j\rangle}^{s(i)} W_{\langle j\rangle}^{s\langle j\rangle s(i)}}{\left(r_{\langle j+1\rangle}^{s(i)}\right)^2 - \left(r_{\langle j\rangle}^{s(i)}\right)^2} - \frac{1}{2} m^{s\langle j\rangle s(i)}$$

(3.18)

where $H^{s(i)}$ = length of axial section *(i)* [cm].

When no central void is developed, the solutions for stresses and strains have a singularity at the center of fuel, and hence the TAMU-ZFP code computes the average stresses and average strains in each mesh-cell instead of the stresses and strains at mesh-points[19]. If the stresses and strains at mesh-points are required, the solutions explained in APPENDIX B can be used to replace Equation 2.104 to 2.108.

The calculations of the average stresses are also affected by gas pressure within the fuel pin, but at the same time the calculations of the internal gas pressure are dependent on the results of the stress-strain analysis. This nonlinearity is processed by the gas-pressure convergence loop. The gas pressure within the fuel pin is given from the ideal gas law for a closed system consisting of multi-thermal-zones that have different temperatures under a single system-pressure:

$$P^{plenum} = \frac{(M_0 + M_{FGR})R}{\dfrac{V^{plenum}}{T^{plenum}} + \sum_{i=1}^{N} \dfrac{V^{p-s(i)}}{T^{p-s(i)}}}$$

(3.19)

where P^{plenum} = gas pressure within the fuel pin [MPa]

---

[19]When $r_{\langle 1\rangle}^{f-s(i)}$ is zero, $r_{\langle 1\rangle}^{f-s(i)} W_{\langle 1\rangle}^{f-s\langle 1\rangle s(i)}$ has an indeterminate form which goes to zero. Thus, the solutions for the average stresses and average strains do not involve any singularity.

M_0 = initial mole of gas in the fuel pin [mol] = $\dfrac{P_0^{plenum}}{R}\left(\dfrac{V_0^{plenum}}{T_0^{plenum}}+\displaystyle\sum_{i=1}^{N}\dfrac{V_0^{p-s(i)}}{T_0^{p-s(i)}}\right)$

M_{FGR} = mole of the fission gas released to the gap and plenum [mol]

R = gas constant = 8.314 [J/mol-K]

V_0^{plenum} = initial volume of the plenum region [cm^3]

T_0^{plenum} = initial average temperature of the plenum region [K]

N = number of axial sections

$V^{p-s(i)}$ = volume of the pores in axial section *(i)* [cm^3]

$T^{p-s(i)}$ = average temperature of the pores in axial section *(i)* [K].

The mechanical computations proceed from the bottom axial section to the top axial section because the axial deformation occurs upward with an axial boundary

Axial Section
for Non-
Mechanical
Analysis

Intact Mesh Cells   Mesh Cells after Displacements
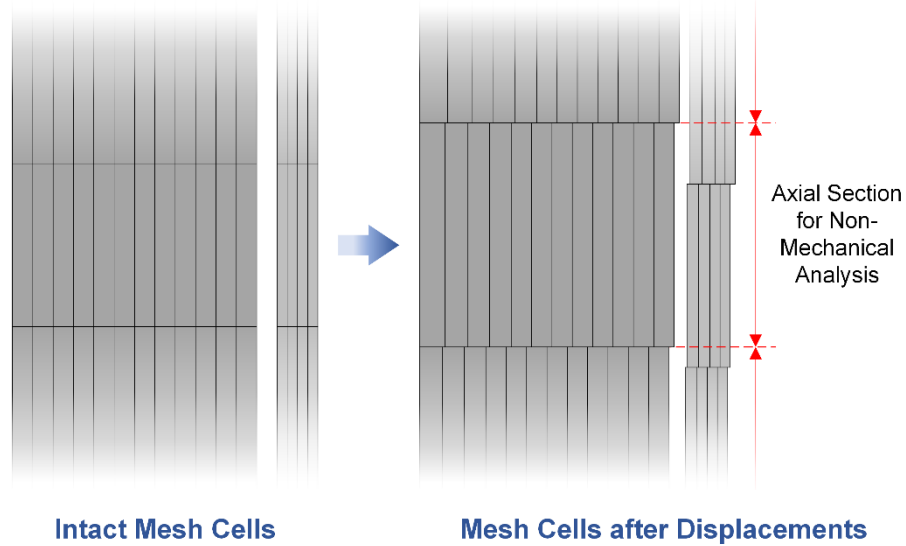
Figure 3.9. Mesh cells created with static dimensioning.

condition at the bottom of the fuel pin. Information on the friction forces is, meanwhile, propagated from the top axial section to the bottom axial section. The friction-force convergence loop deals with the nonlinearity which is caused by the discrepancy between computation direction and information-propagation direction.

The fuel performance calculations in a fuel pin require fuel axial-sections and cladding axial-sections to be matched for coupled evaluations. In this research, two dimensioning methods were studied for the fuel-cladding matching: static dimensioning and dynamic dimensioning. As shown in Figure 3.9, the static dimensioning uses two
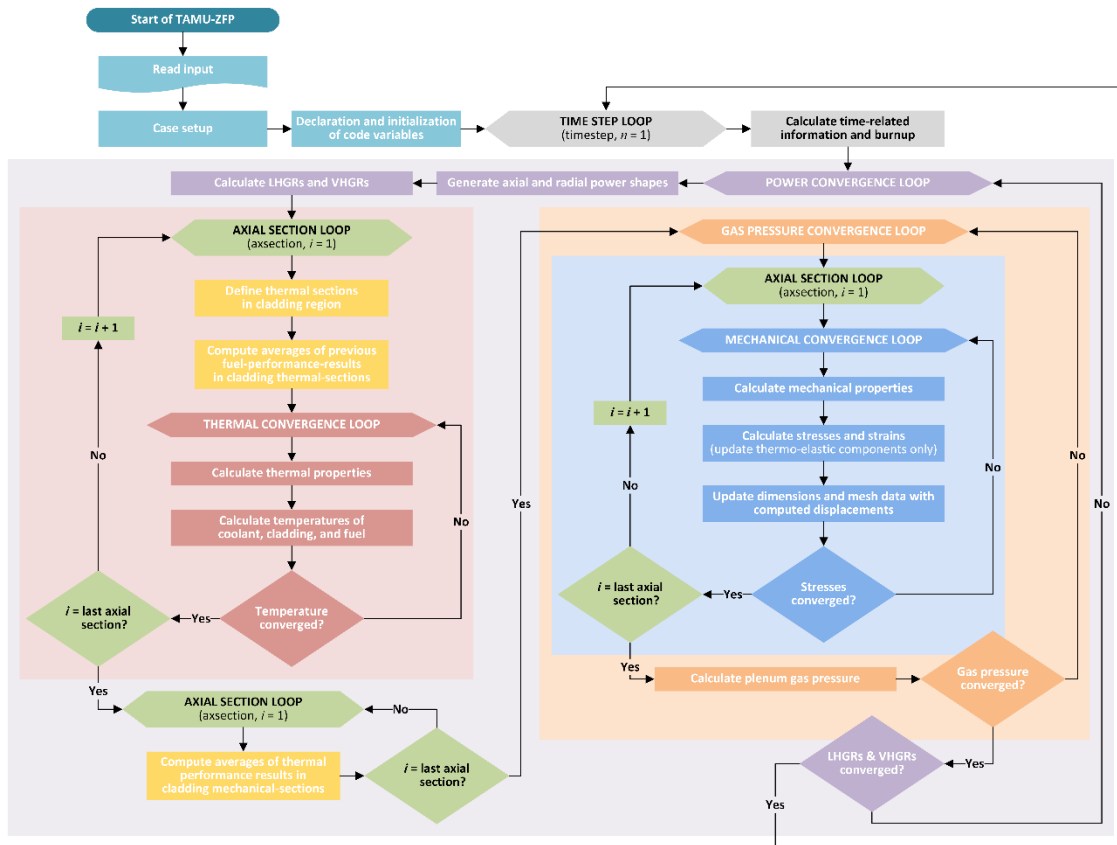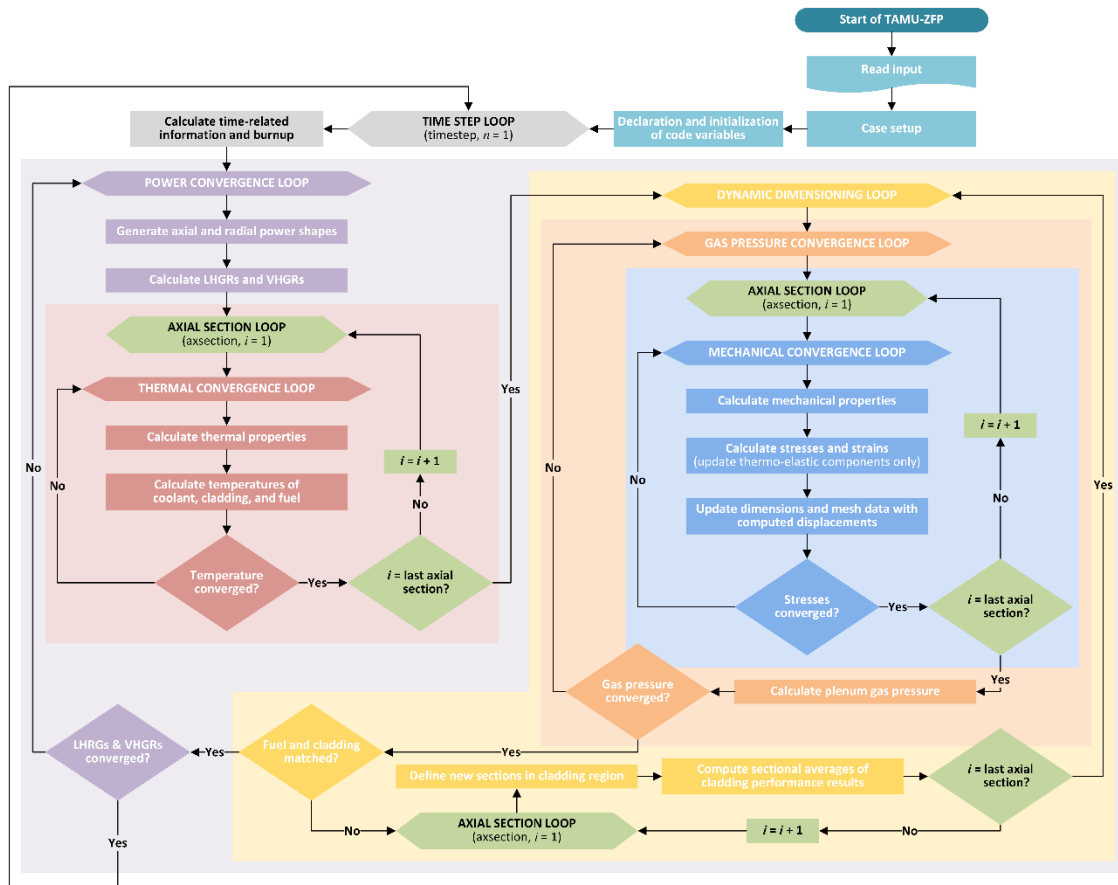

Figure 3.10. Flowchart containing the algorithm of the static dimensioning. The yellow rectangles represent the static dimensioning processes.

different configurations of the cladding axial-sections: cladding axial-sections for mechanical behavior calculations and cladding axial-sections for non-mechanical behavior calculations. The two separate configurations allow the non-mechanical computations to be executed in the matched axial sections even after the changes of the mechanical state. The static dimensioning has a relatively simple algorithm (Figure 3.10), and does not demand any convergence loop for the dimensioning process. However, it is not effective in conducting contact analysis, and generates additional errors related to the averages for radial sections. The dynamic dimensioning employs a convergence loop where the cladding axial-sections are repeatedly matched to the fuel axial-sections after fuel pin deformation as shown in Figure 3.11. Figure 3.12 describes the dynamic dimensioning loop. Although the dynamic dimensioning requires more computations than

Intact Mesh Cells Determined from Dynamic Dimensioning

Mesh Cells after Displacements
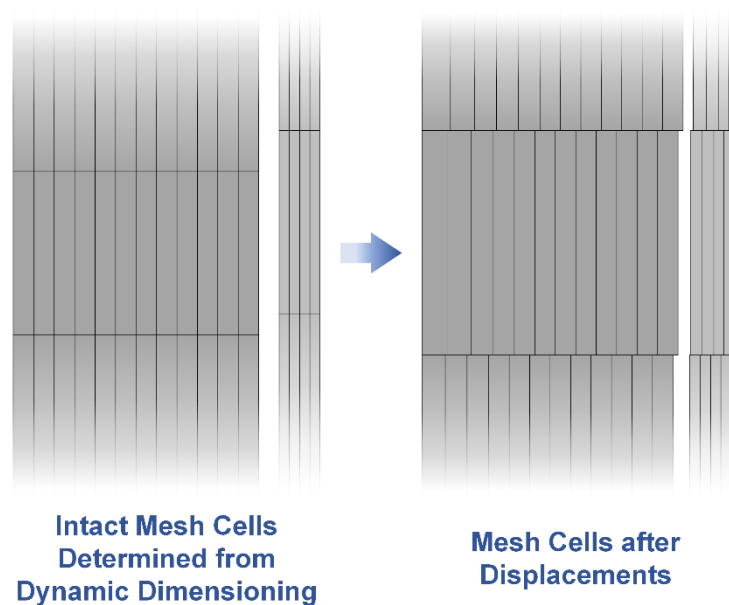
Figure 3.11. Mesh cells created with dynamic dimensioning.

117

Figure 3.12. Flowchart containing the algorithm of the dynamic dimensioning. The yellow rectangles represent the dynamic dimensioning processes.

the static dimensioning, it provides an optimized environment for contact analysis. The TAMU-ZFP code adopted the dynamic dimensioning for the fuel-cladding matching.

Linear heat generation rates and volumetric heat generation rates are changed according to the results of fuel performance calculations. The fuel performance calculations, meanwhile, utilize inform on the linear power and the volumetric power. This nonlinearity is handled by the power convergence loop. The loop also processes a comprehensive coupling of all the fuel performance calculations. The time-step loop and

118

axial section loop operate in order to repeat the code calculations for all of the time-steps and all of the axial sections.

As shown in Figure 3.2 to 3.8, each of the code algorithms, which contains the eight kinds of iterative loops, was structured with three parts to separately simulate two types of fuel behaviors: fuel behaviors described by a total accumulated amount as a function of time (e.g., creep strain, swelling strain, and fission gas release) and fuel behaviors characterized by state function, reversibility, and/or instant equilibrium (e.g., temperature, thermal stress, and gas pressure). The first part determines the values of the parameters used in the accumulated permanent strain models and the accumulated FGR model at the central time of a time-step. The second part calculates the accumulated permanent strains and the accumulated FGR at the end of a time-step. The third part updates all the fuel performance calculation results with the computed permanent strains and FGR at the end of a time-step.

4. ASSESSMENT OF TAMU-ZFP

To assess the prediction ability of the TAMU-ZFP code, its calculation results were compared with experimental data available in the open literature. The irradiation data of the metal fuels are very limited and mostly based on the experiments in EBR-II. In this study, the data of the EBR-II test assemblies designated as X447 and X425 were used for assessment.

Table 4.1. Fuel pin design data of X447 subassembly.

Parameter	Value
Fuel composition	U-10Zr (wt%)
Cladding material	HT9
Radius of fuel slug	0.21997 [cm]
Thickness of cladding	0.038 [cm]
Thickness of gap	0.03403 [cm]
Length of fuel slug	34.3 [cm]
Length of gas plenum	48.02 [cm]
Sodium level above fuel	0.635 [cm]
Initial pressure of helium in gas plenum	0.084 [MPa]
As-cast fuel density [30,31,32]	15.7 [g/cm^3]
Fuel smeared densiy	75 [%]
Fuel pin pitch	0.655 [cm]

4.1. Assessment with X447 Data

The EBR-II subassembly X447 used U-10Zr metal as the fuel material, and the smeared density of the fuel was 75%. Details about the fuel pin design [24,33,34] are represented

in Table 4.1. The X447 test was performed to determine the burnup capability of HT9 cladding at extremely high cladding temperature approaching 660 ℃ [34]. As shown in Figure 4.1 [24], the subassembly was irradiated with high coolant-temperatures that were much higher than normal operating conditions.
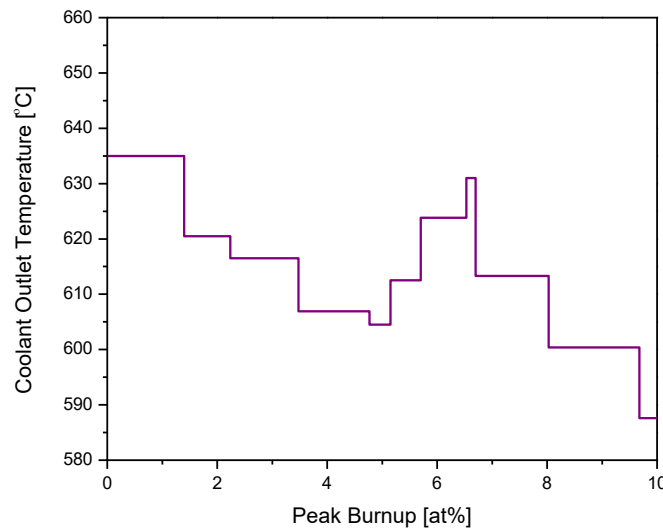
Figure 4.1. History of the coolant outlet temperature of X447 subassembly. Modified from reference [24].

Figure 4.2 and 4.3 show the power history and axial power distribution of X447 subassembly [24], which were used to making the input of TAMU-ZFP for the code assessment. The power history, axial power distribution, and coolant outlet temperature history were obtained from interpreting the input of the FEAST-METAL code [24]. The TAMU-ZFP input requires information on coolant pressure and coolant inlet temperature,

and 0.1 MPa and 370.85 °C were used in the input for the X447 case, respectively. The

fuel pin design data in Table 4.1 were also included in the TAMU-ZFP input.
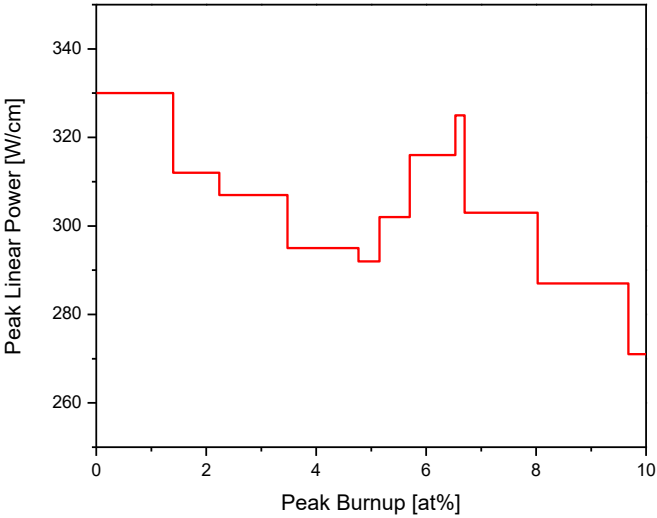
Figure 4.2. Power history of X447 subassembly. Modified from reference [24].
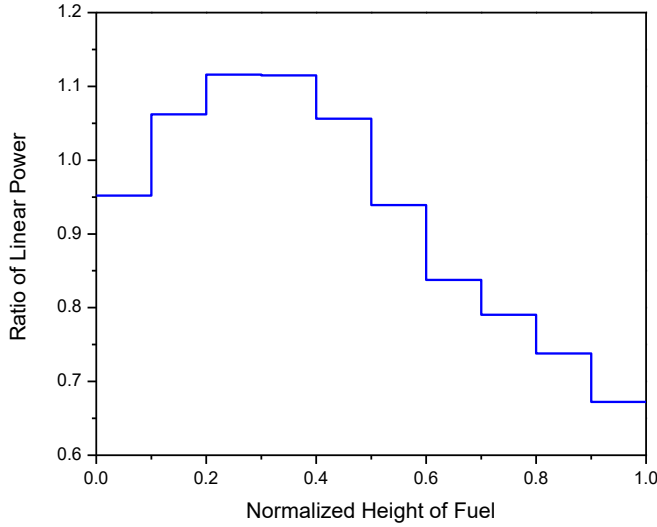
Figure 4.3. Axial power distribution of X447 subassembly. Modified from reference [24].

While the data on the coolant outlet temperatures were given for the X447 case, TAMU-ZFP requires coolant mass flow rates to be specified in the input instead. In this study, the mass flow rate for a single coolant channel (Figure 2.2) was assumed to be 16.2 g/s for the X447 case. As shown in Figure 4.4, the code predicted the coolant outlet temperatures very accurately with the assumed mass flow rate.
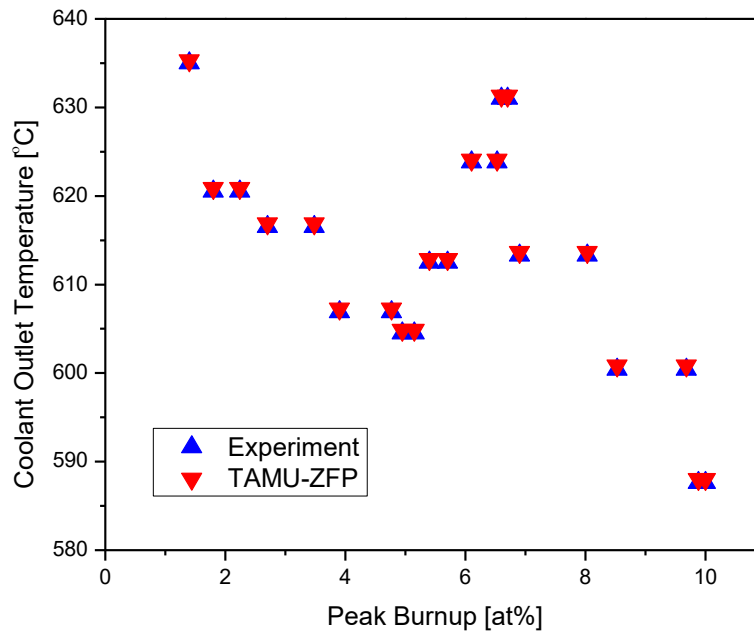
Figure 4.4. TAMU-ZFP calculation results about coolant outlet temperatures.

Temperature distributions computed with the X447 data are represented in Figure 4.5. The temperatures were calculated in axial section *(10)* which was the top axial section located at 31.226 cm to 34.702 cm from the bottom of the fuel slug. The temperatures of axial section *(9)*, having a height of 27.750 cm to 31.226 cm, are also represented in Figure

4.5. The TAMU-ZFP calculation results were compared with the experimental data measured at the inner side of the cladding at the beginning of life (BOL) [33]. The measurement was conducted for four fuel pins designated by the pin IDs: DP70, DP75, DP04, and DP11, respectively. The data from R.G. Pahl [35] is also displayed in Figure 4.5. The peak cladding temperatures in the range of 630 to 660 ℃ were observed in the X447 experiments [34], and they are well matched with the TAMU_ZFP predictions.
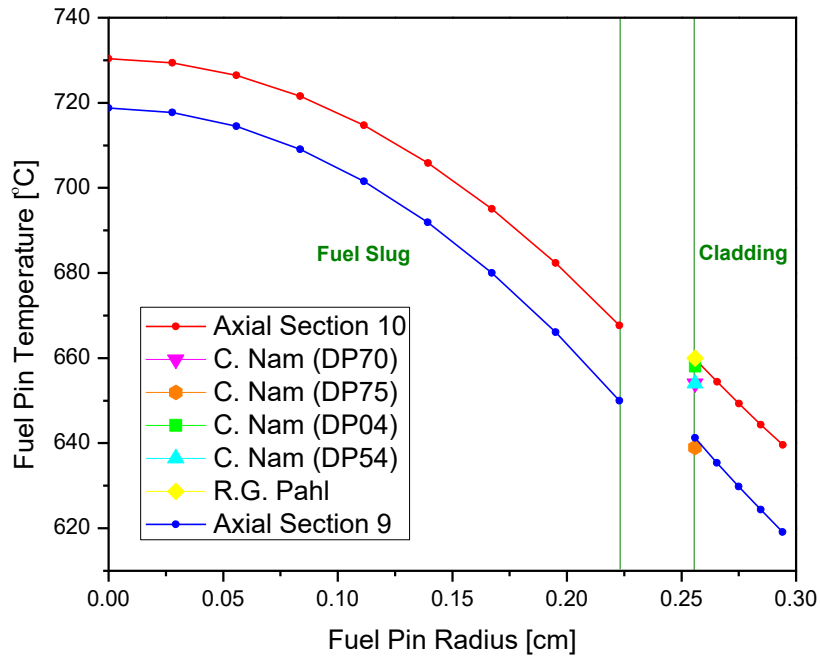

Figure 4.5. TAMU-ZFP calculation results about fuel pin temperature distributions. The BOL linear power used in the calculations was 330 W/cm.

Figure 4.6, 4.7, and 4.8 show radial stress distributions, angular stress distributions, and axial stress distributions in a fuel pin at the BOL, respectively. The stresses in the

principal directions of a cylindrical coordinate were computed at three different axial

locations: 5.193 cm, 19.067 cm, and 32.964 cm from the bottom of the fuel slug,

respectively. The calculation results show that the upper axial sections are under smaller

compressive radial stresses than the lower axial sections in both of the fuel and cladding,

although the upper axial sections are in higher temperatures. It is related to a steeper

temperature-gradient at the lower axial section induced by higher local power. In the

azimuthal direction and the axial direction, the upper axial sections are in smaller

compression than the lower axial sections in the inner regions of the fuel and cladding. In

the outer regions of the fuel and cladding, the lower axial sections are under larger tensile

stresses than the upper axial sections.
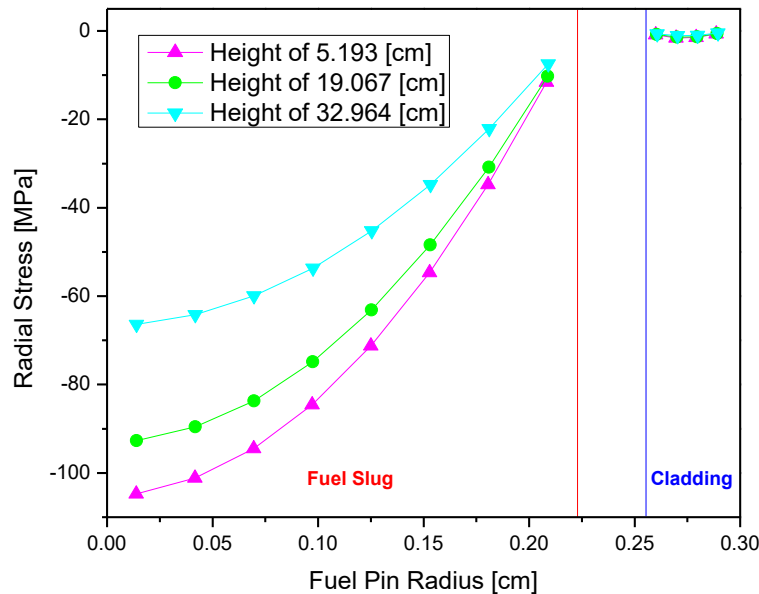
Figure 4.6. TAMU-ZFP calculation results about radial stress distributions.

125
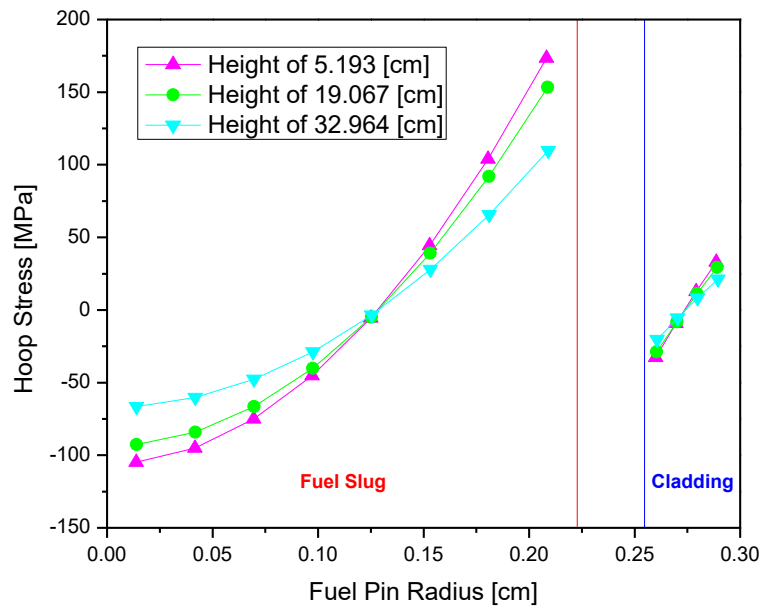
Figure 4.7. TAMU-ZFP calculation results about angular stress distributions.
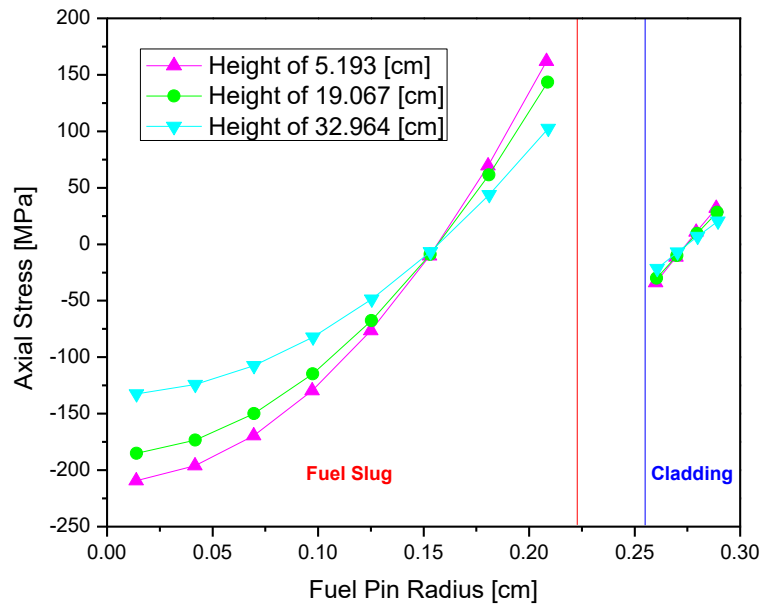

Figure 4.8. TAMU-ZFP calculation results about axial stress distributions.

Figure 4.9 shows a comparison of the stress distributions in the three principal directions. The comparison utilized the stresses calculated at axial section *(10)* which was the top axial section located at 31.226 cm to 34.702 cm from the bottom of the fuel slug. The results indicates that the greatest compressive stress is at the center of the fuel in the axial direction. In the cladding region, the largest compression occurs on the inner side of the cladding in the axial direction. The largest tension occurs on the outer sides of the fuel and cladding in the angular direction. The tensile hoop stress contributes to tearing the outer surface, which is a mechanism of the crack formation in the fuel and cladding.
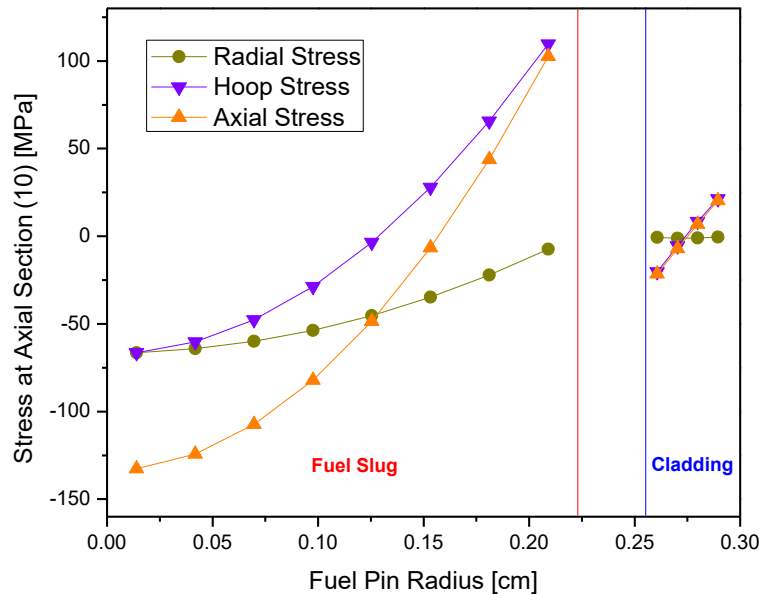

Figure 4.9. Comparison of the calculated stress distributions in three principal directions.

The diametral strains of the cladding axial sections computed with the X447 data are represented in Figure 4.10. The peak linear power, which was 330 W/cm, was used for

the calculations of the diametral strain. The results were compared with the experimental

data measured at 30 cm to 38 cm from the bottom of the fuel slug [34]. The post-irradiation

examination (PIE) was conducted for three fuel pins: breached elements DP70 and DP75

and intact element DP04. The breached elements were excluded from the comparison

because the code version developed in this research did not have any module that evaluates

the cladding breach. The average value of the DP04 data is also display in Figure 4.10.

The code predictions show some differences form the PIE results, but they are still in a

reasonable range in that the current version of the TAMU-ZFP code contains limited fuel
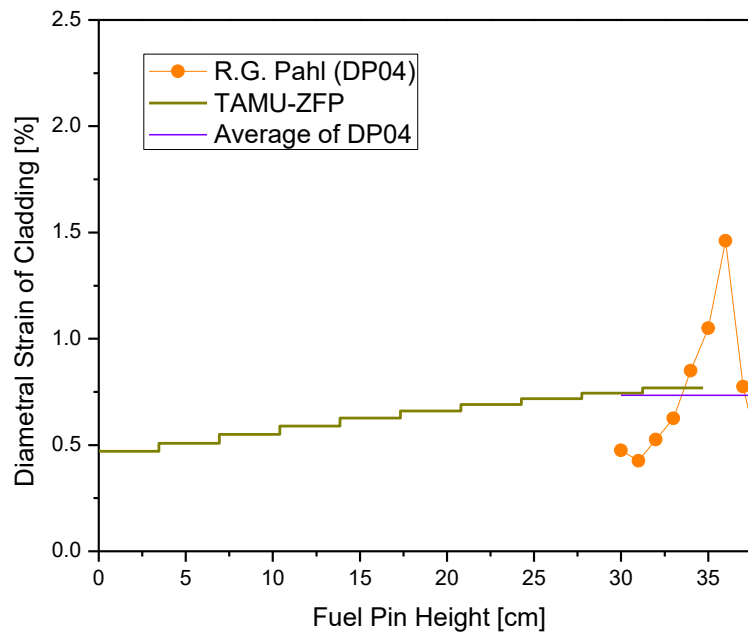
performance models.

Figure 4.10. TAMU-ZFP calculation results about cladding diametral strains.

4.2. Assessment with X425 Data

The metallic U-19Pu-10Zr fuel which had a smeared density of 72.4% was irradiated in X425 subassembly of EBR-II reactor. Table 4.2 shows fuel pin design data of X425 subassembly [18,35,37,38], which were used to making the input of TAMU-ZFP for the code assessment. The TAMU-ZFP input also requires information on coolant pressure and coolant inlet temperature, and 0.1 MPa and 370 °C were used in the input for the X425 case, respectively. The coolant outlet temperature is given in Figure 4.11 [24] as a function of burnup.

Table 4.2. Fuel pin design data of X425 subassembly.

Parameter	Value
Fuel composition	U-19Pu-10Zr (wt%)
Cladding material	HT9
Radius of fuel slug	0.216 [cm]
Thickness of cladding	0.0381 [cm]
Thickness of gap	0.0379 [cm]
Length of fuel slug	34.3 [cm]
Length of gas plenum	34.3 [cm]
Sodium level above fuel	0.635 [cm]
Initial pressure of helium in gas plenum	0.084 [MPa]
As-cast fuel density [36]	15.51469 [g/cm^3]
Fuel smeared densiy	72.4 [%]
Fuel pin pitch	0.655 [cm]

The power history and axial power distribution of X425 subassembly are given in Figure 4.12 and 4.13 [24], and they were used in the input as the reactor operation

parameters. As in the X447 case, the power history, axial power distribution, and coolant

outlet temperature history were obtained from interpreting the FEAST code input [24].
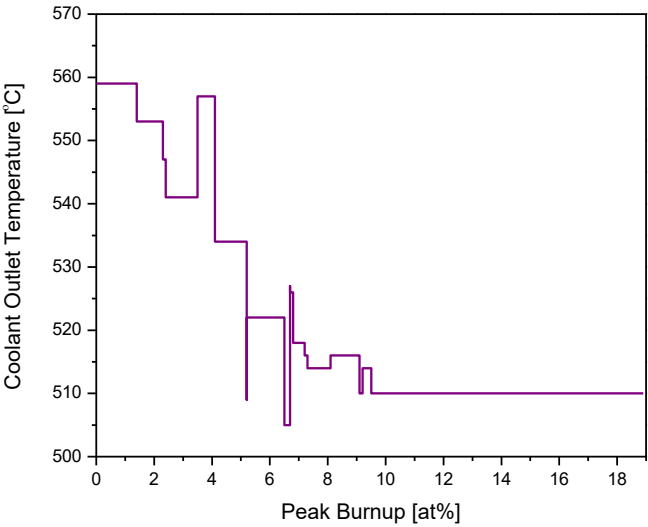

Figure 4.11. History of the coolant outlet temperature of X425 subassembly. Modified from reference [24].
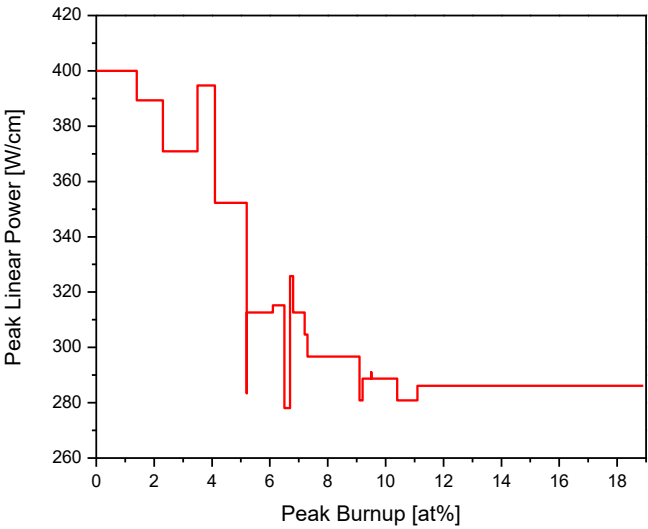

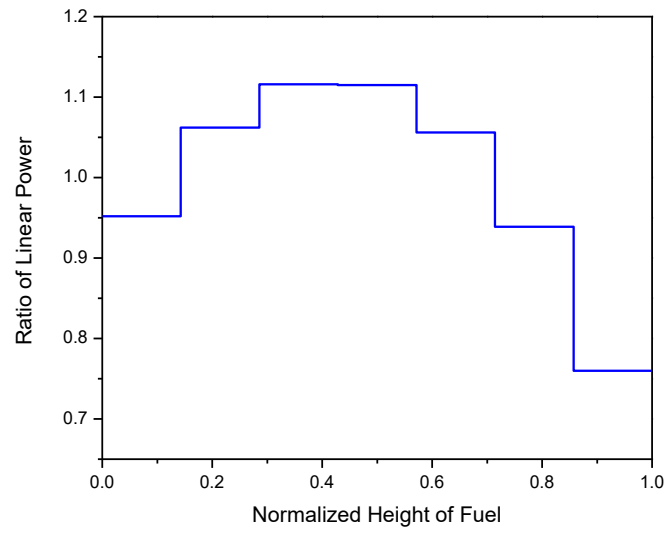Figure 4.12. Power history of X425 subassembly. Modified from reference [24].

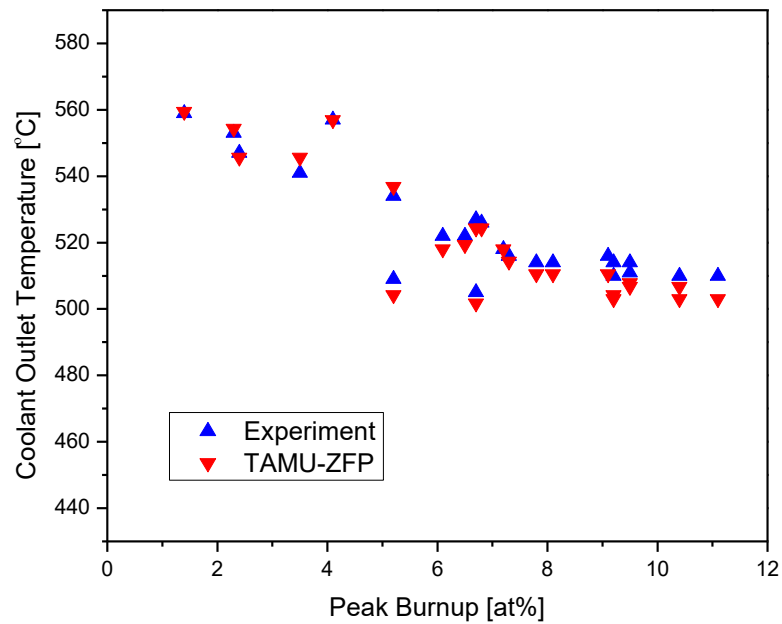Figure 4.13. Axial power distribution of X425 subassembly. Modified from reference [24].

Figure 4.14. TAMU-ZFP calculation results about coolant outlet temperatures.

131

While the data on the coolant outlet temperatures were given for the X425 case, TAMU-ZFP requires coolant mass flow rates to be specified in the input instead. The mass flow rate for a single coolant channel was assumed to be 26.9 g/s for the X425 case. As shown in Figure 4.14, the code reasonably predicted the coolant outlet temperatures with the assumed mass flow rate.
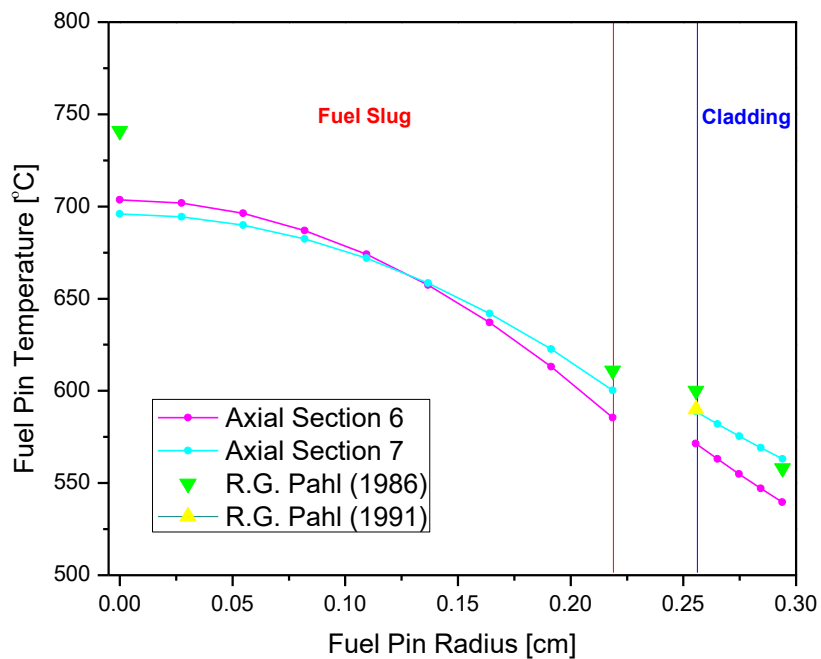

Figure 4.15. TAMU-ZFP calculation results about fuel pin temperature distributions.

Temperature distributions computed with the X425 data are represented in Figure 4.15. The temperatures were calculated in axial section *(7)* which was the top axial section

located at 29.729 cm to 34.691 cm from the bottom of the fuel slug. The temperatures of axial section *(6)*, having a height of 24.768 cm to 29.729 cm, are also represented in Figure 4.15. The average linear power used in the calculations was 400 W/cm. The code results were compared with the fuel element design data provided by R.G. Pahl [36,38]. The computed temperatures show some differences from the design data, especially at the center of the fuel, but they are still in a reasonable range. The discrepancy would be generated by using different local LHGRs in the calculations. Therefore, if more specific information on the fuel element design and its operating conditions is given for making the input, more accurate assessment is possible.
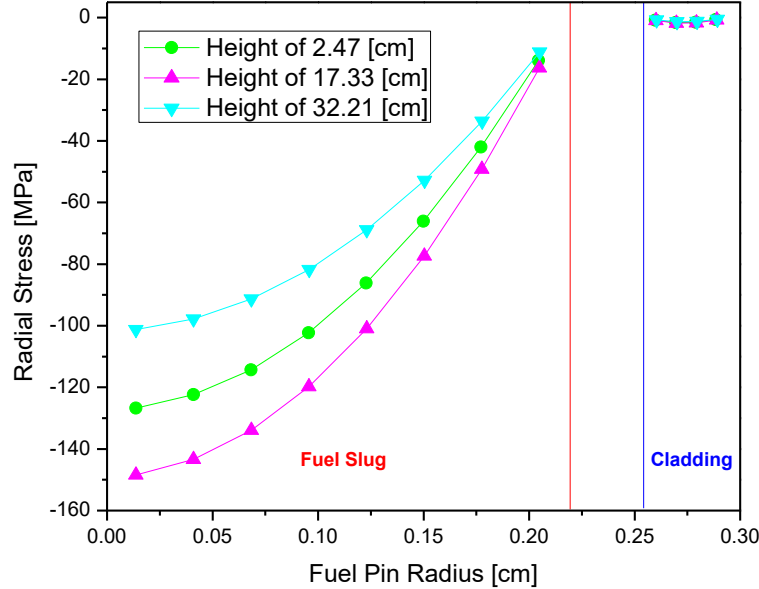

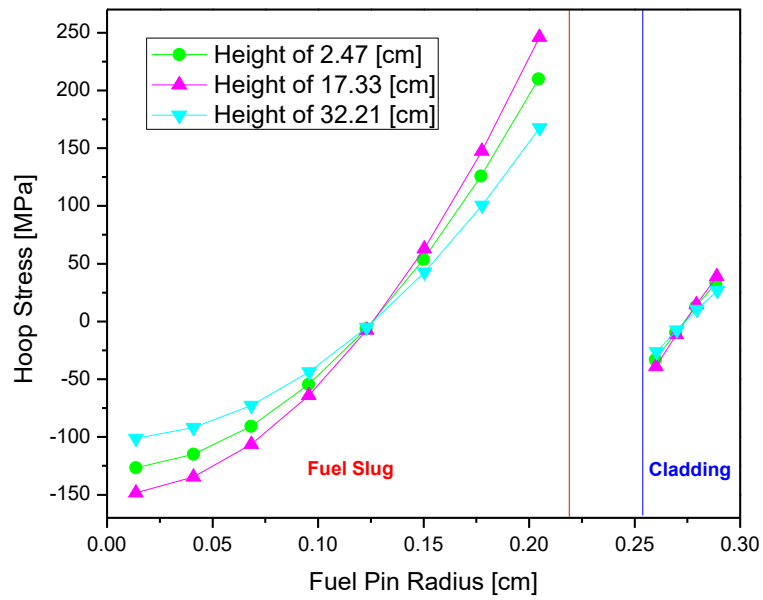Figure 4.16. TAMU-ZFP calculation results about radial stress distributions.

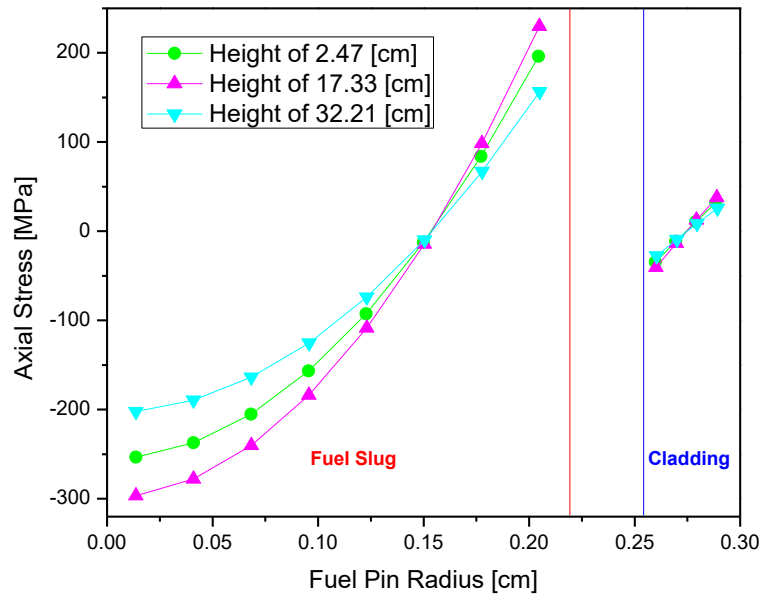Figure 4.17. TAMU-ZFP calculation results about angular stress distributions.

Figure 4.18. TAMU-ZFP calculation results about axial stress distributions.

134

Figure 4.16, 4.17, and 4.18 show radial stress distributions, angular stress distributions, and axial stress distributions in a fuel pin at the BOL, respectively. The stresses in the principal directions of a cylindrical coordinate were computed at three different axial locations: 2.47 cm, 17.33 cm, and 32.21 cm from the bottom of the fuel slug, respectively. The calculation results show that an axial section which has a steeper temperature-gradient induced by higher local power is under larger compressive radial stresses. In the azimuthal direction and the axial direction, the axial section with higher local power is in larger compression in the inner regions of the fuel and cladding. In the outer regions of the fuel and cladding, the axial section with higher local power is under larger tensile stresses regardless of temperature.
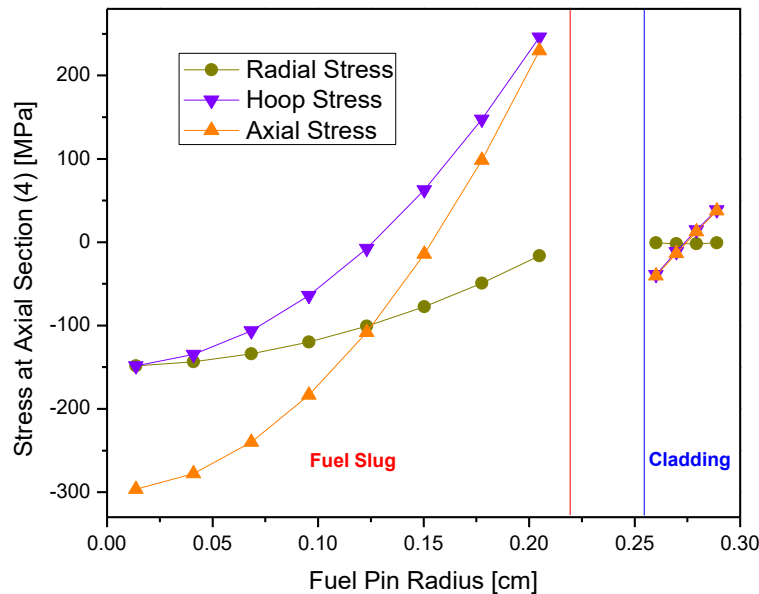

Figure 4.19. Comparison of the calculated stress distributions in three principal directions.

135

Figure 4.19 shows a comparison of the stress distributions in the three principal directions. The comparison utilized the stresses calculated at axial section *(4)* which was located at 14.851 cm to 19.809 cm from the bottom of the fuel slug. The results indicates that the greatest compressive stress is at the center of the fuel in the axial direction. In the cladding region, the largest compression occurs on the inner side of the cladding in the axial direction. The largest tension occurs on the outer sides of the fuel and cladding in the angular direction. The tensile hoop stress contributes to tearing the outer surface, which is a mechanism of the crack formation in the fuel and cladding. Although X425 subassembly is under lower irradiation temperatures than X447 subassembly, it shows much larger stresses in all the principal directions. It is attributed to the higher linear power of X425 subassembly.
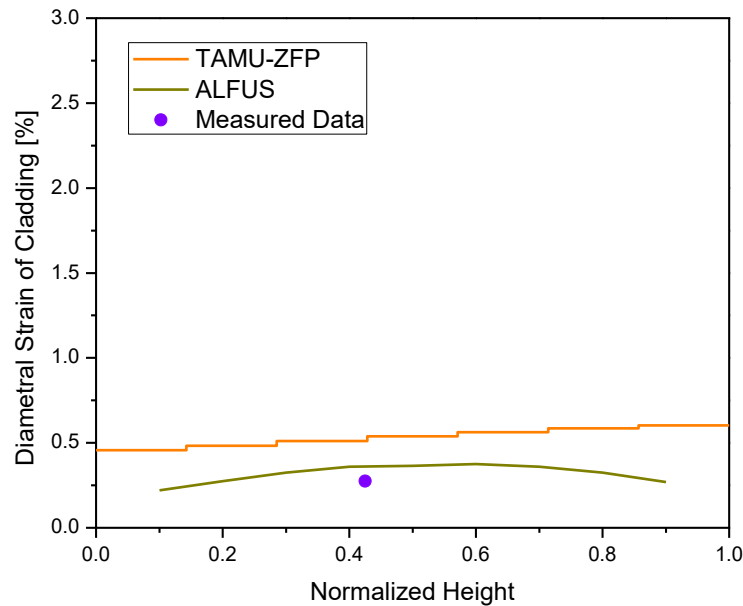
Figure 4.20. TAMU-ZFP calculation results about cladding diametral strains.

The diametral strains of the cladding axial sections computed with the X425 data are represented in Figure 4.20. The diametral strains were calculated at 10.4 at% peak burnup. The predictions of the TAMU-ZFP code were compared with the experimental data measured at 10.4 at% peak burnup [18]. The calculation results of the ALFUS code are also displayed in Figure 4.20 [18]. The diametral strains computed by TAMU-ZFP are slightly higher than the other data, but they are still in a reasonable range.

5. CONCLUSIONS

Accurate evaluations of fuel behavior is a crucial part in the determination of fuel operation limits and in the verification of burnup capabilities and reliability characteristics. In-pile behaviors of metallic fuels are closely connected with one another under a wide variety of irradiation histories. In most cases, each individual behavior cannot be evaluated by considering its own physical phenomena in isolation. Due to the high degree of interconnection among the fuel behaviors, the models that predict and quantify the fuel behaviors contain nonlinear mathematical expressions, and the coefficients and boundary conditions of each model are dependent on the calculations of other models. These complex relations generally require an integrated platform which has high-performance computing capabilities to handle the fuel behavior models simultaneously. In this research, a comprehensive computational tool has been developed to provide an optimized platform where each model can communicate with other models to calculate the synergistic effects of the fuel behaviors. The tool was named Tool for Analyzing Metallic U-Zr Fuel Performance (TAMU-ZFP).

The fuel behavior models involve thermo-mechanical parameters in their mathematical functions, and hence the framework of a fuel performance code that holds the fuel behavior models should provide accurate information on those parameters. The framework of the TAMU-ZFP code was erected by implementing improved thermo-mechanical models in the code with new advanced algorithms. The governing equations (GEs) of the thermo-mechanical models were established for each individual cell of the

spatial and temporal mesh employed in the code, and the GEs of a cell were solved with the boundary conditions pertaining to the specific cell. These cell-based models inherently and effectively describe the spatial variation and time dependence of thermo-mechanical behaviors with minimized unrealistic assumptions and simplifications. Also, the cell-based models are fully compatible with the adaptable mesh system and dynamic dimensioning which were introduced into TAMU-ZFP. The adaptable mesh system means that the size and number of mesh cells are variable and non-uniform in order to accommodate the spatial and temporal dependence of the fuel pin deformation. The dynamic dimensioning was implemented to readjust the marred or mismatched mesh after the fuel pin deformation. The model features mentioned above ultimately allow an approach where the code can track the thermo-mechanical evolution of each cell with less restriction. Thus, based on the specific behavioral history of each cell, the framework developed with the new thermo-mechanical models provides optimized environments for the coupling of fuel performance models.

In the case of thermal analysis, the coolant temperature associated with the fuel pin of interest was calculated by a single channel coolant enthalpy rise model. The Lax-Wendroff one step method was applied to the GE of the single channel model for the transient coolant temperature. The temperature distributions in the fuel pin were obtained from an energy balance equation in which the net current of heat was defined by Fourier's law. The transient temperature distributions used a modified Crank-Nicolson scheme to take account of the time dependence of material properties in addition to their spatial variation. Mechanical analysis models employed three fundamental conditions: conditions

for equilibrium of forces and moments, geometric compatibility, and stress-strain relations. Each of the three conditions yields a set of equations whose solutions determine the state of stress and strain in a fuel pin. The simultaneous equations from the three conditions were repeatedly established for each small axial section on the assumption of azimuthal and axial symmetry within an axial section. They were solved in each radial section of an axial section with specific section boundary conditions. The surface boundary conditions and axial boundary conditions are divided into open-gap conditions and closed-gap conditions according to the existence of the fuel-cladding contact.

TAMU-ZFP adopted new advanced algorithms to implicitly calculate the synergic effects of the irradiation behaviors. Radial and axial interlocking in a fuel performance calculation, couplings of fuel performance models, contact analysis, and dynamic dimensioning and power adjustments after fuel pin deformation are executed in three main algorithms: open-gap algorithm, serial-contact algorithm, and random-contact algorithm. The open-gap algorithm can call two sub-algorithms which computes initial serial-contact time and completely-random-contact time, respectively. Also, the serial-contact algorithm can call two sub-algorithms which computes continuous serial-contact time and partly-random-contact time, respectively. The calculation scheme in each of the three main algorithms was constructed with three parts to separately simulate two types of fuel behaviors: fuel behaviors described by a total accumulated amount as a function of time and fuel behaviors characterized by state function, reversibility, and/or instant equilibrium. The three parts contain eight kinds of iterative loops: time-step loop, power convergence loop, thermal convergence loop, dynamic dimensioning loop, gas-pressure

convergence loop, friction-force convergence loop, mechanical convergence loop, and axial section loop. The time-step loop and axial section loop operate in order to repeat the code calculations for all the time-steps and all the axial sections. The other loops was designed for the implicit determination of converged values of parameters and variables in fuel performance models.

Also, various convenient features were implemented in the TAMU-ZFP code. An example is transient modules that allow one job step for the simulations of design-based off-normal fuel behaviors. It is not needed in TAMU-ZFP to generate the initial conditions for the transient simulation, store interim results, and separately run a transient code with its own input. Another convenient feature is a 3D graphical tool included in the code. TAMU-ZFP (written in the C language) generates raw data files for the visualization of the code output, and a program built on the MATLAB platform processes the raw data files for basic post-processing and visualization.

To assess the prediction ability of the TAMU-ZFP code, its calculation results were compared with experimental data available in the open literature. The irradiation data of the metal fuels are very limited and mostly based on the experiments in EBR-II. In this study, the data of the EBR-II test assemblies designated as X447 and X425 were used for assessment. TAMU-ZFP successfully predicted most of the thermo-mechancal behaviors of metallic fuels with high accuracy. However, the code version developed in this research contained limited fuel performance models, so the code showed discrepancies in simulating some mechanical behaviors. Therefore, further implementation of reliable fuel performance models is required for the future research. For these updates of the TAMU-

ZFP code, new physics-based fuel performance models should be studied in company with investigating up-to-date materials properties models. Another important part of the updates is the validation and verification work which entails a procedure known as calibrating or fine code-tuning. To do this, more accurate PIE data and in-pile data should be obtained with establishing a benchmark for the TAMU-ZFP simulation.

REFERENCES

[1] K. Aoto et al., A summary of sodium-cooled fast reactor development, Progress in Nuclear Energy 77 (2014) 247–265.

[2] B. Merk, A. Stanculescu, P. Chellapandi, R. Hill, Progress in reliability of fast reactor operation and new trends to increased inherent safety, Applied Energy 147 (2015) 104–116.

[3] F. Delage et al., Status of advanced fuel candidates for sodium fast reactor within the Generation IV International Forum, Journal of Nuclear Materials Vol. 441 (2013) 515–519.

[4] J. Yoo et al., Overall system description and safety characteristics of prototype Gen IV sodium cooled fast reactor in Korea, Nuclear Engineering and Technology 48 (2016) 1059–1070.

[5] C.B. Lee et al., Metal fuel development and verification for prototype generation IV sodium-cooled fast reactor, Nuclear Engineering and Technology 48 (2016) 1096–1108.

[6] Y.I. Chang, The Integral Fast Reactor, Nuclear Technology 88 (1989) 129–138.

[7] B.R. Seidel, L.C. Walters, Y.I. Chang, Advances in metallic nuclear fuel, Journal of Metals 39 (1987) 10–13.

[8] Y.I. Chang, Technical rationale for metal fuel in fast reactors, Nuclear Engineering and Technology 39 (2007) 161–170.

[9] D.C. Crawford, D.L. Porter, S.L. Hayes, Fuels for sodium-cooled fast reactors: US perspective, Journal of Nuclear Materials 371 (2007) 202–231.

[10] T. Sofu, A review of inherent safety characteristics of metal alloy sodium-cooled fast reactor fuel against postulated accidents, Nuclear Engineering and Technology 47 (2015) 227–239.

[11] D.E. Burkes et al., A US perspective on fast reactor fuel fabrication technology and experience part I: metal fuels and assembly design, Journal of Nuclear Materials 389 (2009) 458–469.

[12] G.L. Hofman, L.C. Walters, T.H. Bauer, Metallic fast reactor fuels, Progress in Nuclear Energy 31 (1997) 83–110.

[13] T. Ogata, Y.S. Kim, A.M. Yacout, Metal fuel performance modeling and simulation, in: Comprehensive Nuclear Materials, Volume 3, Elsevier, Amsterdam, The Netherlands, 2012.

[14] T. Ogata, Metal fuel, in: Comprehensive Nuclear Materials, Volume 3, Elsevier, Amsterdam, The Netherlands, 2012.

[15] A. Karahan, J. Buongiorno, A new code for predicting the thermo-mechanical and irradiation behavior of metallic fuels in sodium fast reactors, Journal of Nuclear Materials 396 (2010) 283–293.

[16] M.C. Billone et al., Status of fuel element modeling codes for metallic fuels, in: Proceedings of the International Conference on Reliable Fuels for Liquid Metal Reactors, American Nuclear Society, Tucson, Arizona, 1986.

[17] T. Kobayashi et al., Development of the SESAME metallic fuel performance code, Nuclear Technology 89 (1990) 183–193.

[18] T. Ogata, T. Yokoo, Development and validation of ALFUS: an irradiation behavior analysis code for metallic fast reactor fuels, Nuclear Technology 128 (1999) 113–123.

[19] W. Hwang, C. Nam, T.S. Byun, Y.C. Kim, MACSIS: a metallic fuel performance analysis code for simulating in-reactor behavior under steady-state conditions, Nuclear Technology 123 (1998) 130–141.

[20] W. Hwang, B. Lee, Y.J. Kim, Recent improvements in modelling fission gas release and rod deformation on metallic fuel in LMR, Annals of Nuclear Energy 27 (2000) 1059–1069.

[21] Y. Tsuboi, T. Ogata, M. Kinoshita, H. Saito, Mechanistic model of fission gas behavior in metallic fuel, Journal of Nuclear Materials 188 (1992) 312–318.

[22] T. Ogata, M. Kinoshita, H. Saito, T. Yokoo, Analytical study on deformation and fission gas behavior of metallic fast reactor fuel, Journal of Nuclear Materials 230 (1996) 129–139.

[23] M. Ishida, T. Ogata, M. Kinoshita, Constituent migration model for U-Pu-Zr metallic fast reactor fuel, Nuclear Technology 104 (1993) 37–51.

[24] A. Karahan, Modeling of thermo-mechanical and irradiation behavior of metallic and oxide fuels for sodium fast reactors, Ph.D. Thesis, Nuclear Science and Engineering Department, Massachusetts Institute of Technology, Cambridge, MA, 2009.

[25] C.B. Lee, D.H. Kim, Y.H. Jung, Fission gas release and swelling model of metallic fast reactor fuel, Journal of Nuclear Materials 288 (2001) 29–42.

[26] G.A. Berna, C.E. Beyer, K.L. Davis, D.D. Lanning, FRAPCON-3: A Computer Code for the Calculation of Steady-State, Thermal-Mechanical Behavior of Oxide Fuel Rods for High Burnup, NUREG/CR-6534, Volume 2, United States Nuclear Regulatory Commission, Washington, DC, 1997.

[27] D. Olander, Fundamental Aspects of Nuclear Reactor Fuel Elements, TID-26711-P1, National Technical Information Service, Springfield, VA, 1976.

[28] D.E. Janney, Metallic Fuels Handbook, Part 1: Alloys Based on U-Zr, Pu-Zr, U-Pu, or U-Pu-Zr, Including Those with Minor Actinides (Np, Am, Cm), Rare-earth Elements (La, Ce, Pr, Nd, Gd), and Y, INL/EXT-15-36520, Revision 2 Part 1, Idaho National Laboratory, Idaho Falls, ID, 2017.

[29] J. Kim, J.W. Lee, K. Kim, J. Park, Injection casting of U-Zr and U-Zr-RE fuel slugs and their characterization, Journal of Nuclear Science and Technology 54 (2017) 648–654.

[30] F.A. Rough, An Evaluation of Data on Zirconium-Uranium Alloys, BMI-1030, Battelle Memorial Institute, Columbus, Ohio, 1955.

[31] C. Basak, G.J. Prasada, H.S. Kamath, N. Prabhu, An evaluation of the properties of as-cast U-rich U-Zr alloys, Journal of Alloys and Compounds 480 (2009) 857–862.

[32] J.H. Kim, H. Song, K.H. Kim, C.B. Lee, Fabrication of uranium alloy fuel slug for sodium-cooled fast reactor by injection casting, Journal of Radioanalytical and Nuclear Chemistry 301 (2014) 797–803.

[33] C. Nam, W. Hwang, D. Sohn, Statistical failure analysis of metallic U-10Zr/HT9 fast reactor fuel pin by considering the Weibull distribution and cumulative damage fraction, Annals of Nuclear Energy 25 (1998) 1441–1453.

[34] R.G. Pahl, C.E. Lahm, S.L. Hayes, Performance of HT9 clad metallic fuel at high temperature, Journal of Nuclear Materials 204 (1993) 141–147.

[35] R.G. Pahl, D.L. Porter, D.C. Crawford, L.C. Walters, Irradiation behavior of metallic fast reactor fuels, Journal of Nuclear Materials 188 (1992) 3–9.

[36] R.G. Pahl et al., Recent Irradiation Tests of Uranium-Plutonium-Zirconium Metal Fuel Elements, CONF-860931--9, Argonne National Laboratory, Idaho Falls, ID, 1986.

[37] R.G. Pahl, R.S. Wisner, M.C. Billone, G.L. Hofman, Steady-state Irradiation Testing of U-Pu-Zr Fuel to >18% Burnup, CONF-900804--25, Argonne National Laboratory, Idaho Falls, ID, 1990.

[38] R.G. Pahl, C.E. Lahm, H. Tsai, M.C. Billone, Irradiation Experience with HT9-clad Metallic Fuel, ANL/CP--72040, Argonne National Laboratory, Idaho Falls, ID, 1991.

APPENDIX A

ANALYTICAL SOLUTIONS FOR STEADY-STATE TEMPERATURE

DISTRIBUTIONS IN A FUEL PIN

A.1.   Analytical Solution for Steady-State Cladding Temperature

The steady-state cladding temperatures calculated by TAMU-ZFP have been compared
with the following analytical solution:

$$T^{c-s\langle j\rangle s(i)}\left(r\right)=T_{\langle j+1\rangle}^{c-s\langle j+1\rangle s(i)}+\frac{p^{s(i)}}{2\pi k^{c-s\langle j\rangle s(i)}}\ln\left(\frac{r_{\langle j+1\rangle}^{c-s(i)}}{r}\right) \qquad (A.1)$$

where $T^{c-s\langle j\rangle s(i)}\left(r\right)$ = cladding temperature at radius r in radial section $<j>$ of axial

section (i) [K]

radial section $<j>$ = an arbitrary radial section of axial section (i) in the cladding

region (radial section $<j>$ is located between radial node

$r_{\langle j\rangle}^{c-s(i)}$ and $r_{\langle j+1\rangle}^{c-s(i)}$)

$p^{s(i)}$ = average linear heat generation rate in axial section (i) [W/cm]

$k^{c-s\langle j\rangle s(i)}$ = average thermal conductivity of the cladding in radial section $<j>$ of

axial section (i) [W/cm-K]

$T_{\langle j+1\rangle}^{c-s\langle j+1\rangle s(i)}$ = cladding temperature at radial node $r_{\langle j+1\rangle}^{c-s(i)}$ in radial section $<j+1>$ of

axial section (i) [K].

147

A.2.   Analytical Solution for Steady-State Fuel Temperature

The steady-state fuel temperatures calculated by TAMU-ZFP have been compared with the following analytical solution:

First radial section (radial section _<1>_)

$$T^{f-s\langle 1\rangle s(i)}(r) = T^{f-s\langle 2\rangle s(i)}_{\langle 2\rangle} + \frac{q_{gen}^{m\,f-s\langle 1\rangle s(i)}}{4k^{f-s\langle 1\rangle s(i)}}\left[\left(r_{\langle 2\rangle}^{f-s(i)}\right)^2 - r^2\right] \tag{A.2}$$

The others (arbitrary radial section _<j>, j ≥ 2_)

$$T^{f-s\langle j\rangle s(i)}(r) = T^{f-s\langle j+1\rangle s(i)}_{\langle j+1\rangle} + \frac{q_{gen}^{m\,f-s\langle j\rangle s(i)}}{4k^{f-s\langle j\rangle s(i)}}\left[\left(r_{\langle j+1\rangle}^{f-s(i)}\right)^2 - r^2\right]$$

$$+ \sum_{n=2}^{j}\left[\frac{\left(r_{\langle n\rangle}^{f-s(i)}\right)^2}{2k^{f-s\langle j\rangle s(i)}}\left(q_{gen}^{m\,f-s\langle n-1\rangle s(i)} - q_{gen}^{m\,f-s\langle n\rangle s(i)}\right)\right]\ln\left(\frac{r_{\langle j+1\rangle}^{f-s(i)}}{r}\right) \tag{A.3}$$

where $T^{f-s\langle j\rangle s(i)}(r)$ = fuel slug temperature at radius _r_ in radial section _<j>_ of axial

section _(i)_ [K] ($r_{\langle j\rangle}^{f-s(i)} \le r \le r_{\langle j+1\rangle}^{f-s(i)}$ in radial section _<j>_)

$T^{f-s\langle j+1\rangle s(i)}_{\langle j+1\rangle}$ = fuel slug temperature at radial node $r_{\langle j+1\rangle}^{f-s(i)}$ in radial section _<j+1>_ of

axial section _(i)_ [K]

$q_{gen}^{m\,f-s\langle j\rangle s(i)}$ = average volumetric heat generation rate in radial section _<j>_ of axial

section _(i)_ [W/cm³]

$k^{f-s\langle j\rangle s(i)}$ = average thermal conductivity of the fuel in radial section _<j>_ of axial

section _(i)_ [W/cm-K].

APPENDIX B

POLYNOMIAL SOLUTIONS FOR STRESSES AND STRAINS IN THE FIRST

RADIAL SECTION OF THE FUEL

When no central void is developed, the solutions for stresses and strains (Equation 2.104 to 2.108) have a singularity at the center of the fuel. On the other hand, the solutions for average stresses and average strains (Equation 3.14 to 3.18) do not involve any singularity. Thus, the TAMU-ZFP code computes the average stresses and average strains in each mesh-cell instead of the stresses and strains at each mesh-point. If the stresses and strains at mesh-points are required, the solutions for the first radial section which contains the center of the fuel need to be approximated by the following polynomial solutions:

$$u_r^{f-s\langle 1\rangle s(i)}(r) = C_1^{f-s\langle 1\rangle s(i)} r + W_{series}^{f-s\langle 1\rangle s(i)}(r) \tag{B.1}$$

$$
\begin{aligned}
\sigma_r^{f-s\langle 1\rangle s(i)}(r) = {} & a^{f-s\langle 1\rangle s(i)}\left(1+2b^{f-s\langle 1\rangle s(i)}\right)C_1^{f-s\langle 1\rangle s(i)} + a^{f-s\langle 1\rangle s(i)}b^{f-s\langle 1\rangle s(i)}C_z^{f-s(i)} \\
& + a^{f-s\langle 1\rangle s(i)}\left[\left(1+2b^{f-s\langle 1\rangle s(i)}\right)X_{series}^{f-s\langle 1\rangle s(i)}(r) - b^{f-s\langle 1\rangle s(i)}m^{f-s\langle 1\rangle s(i)}S(r) \right. \\
& \left. \qquad + b^{f-s\langle 1\rangle s(i)}c^{f-s\langle 1\rangle s(i)} + d_r^{f-s\langle 1\rangle s(i)}\right]
\end{aligned}
\tag{B.2}
$$

$$
\begin{aligned}
\sigma_\theta^{f-s\langle 1\rangle s(i)}(r) = {} & a^{f-s\langle 1\rangle s(i)}\left(1+2b^{f-s\langle 1\rangle s(i)}\right)C_1^{f-s\langle 1\rangle s(i)} + a^{f-s\langle 1\rangle s(i)}b^{f-s\langle 1\rangle s(i)}C_z^{f-s(i)} \\
& + a^{f-s\langle 1\rangle s(i)}\left[\left(1+2b^{f-s\langle 1\rangle s(i)}\right)X_{series}^{f-s\langle 1\rangle s(i)}(r) - \left(1+b^{f-s\langle 1\rangle s(i)}\right)m^{f-s\langle 1\rangle s(i)}S(r) \right. \\
& \left. \qquad + b^{f-s\langle 1\rangle s(i)}c^{f-s\langle 1\rangle s(i)} + d_\theta^{f-s\langle 1\rangle s(i)}\right]
\end{aligned}
\tag{B.3}
$$

$$\sigma_z^{f-s\langle 1\rangle s(i)}(r) = 2a^{f-s\langle 1\rangle s(i)}b^{f-s\langle 1\rangle s(i)}C_1^{f-s\langle 1\rangle s(i)} + a^{f-s\langle 1\rangle s(i)}\left(1+b^{f-s\langle 1\rangle s(i)}\right)C_z^{f-s(i)}$$

$$+a^{f-s\langle 1\rangle s(i)}\left[2b^{f-s\langle 1\rangle s(i)}X_{series}^{f-s\langle 1\rangle s(i)}(r)-b^{f-s\langle 1\rangle s(i)}m^{f-s\langle 1\rangle s(i)}S(r)\right. \tag{B.4}$$

$$\left.+b^{f-s\langle 1\rangle s(i)}c^{f-s\langle 1\rangle s(i)}+d_z^{f-s\langle 1\rangle s(i)}\right]$$

$$\varepsilon_r^{f-s\langle 1\rangle s(i)}(r) = C_1^{f-s\langle 1\rangle s(i)} + X_{series}^{f-s\langle 1\rangle s(i)}(r) \tag{B.5}$$

$$\varepsilon_\theta^{f-s\langle 1\rangle s(i)}(r) = C_1^{f-s\langle 1\rangle s(i)} + X_{series}^{f-s\langle 1\rangle s(i)}(r) - m^{f-s\langle 1\rangle s(i)}S(r) \tag{B.6}$$

where $W_{series}^{f-s\langle 1\rangle s(i)}(r) = k^{f-s\langle 1\rangle s(i)}\dfrac{r}{2} + l^{f-s\langle 1\rangle s(i)}\dfrac{r}{2}$

$$+m^{f-s\langle 1\rangle s(i)}\left[\frac{r(r-1)^1}{1}-\frac{r(r-1)^2}{2}+\frac{r(r-1)^3}{3}-\frac{r(r-1)^4}{4}+\frac{r(r-1)^5}{5}\right] \text{ [cm]}$$

$$X_{series}^{f-s\langle 1\rangle s(i)}(r) = k^{f-s\langle 1\rangle s(i)}\frac{1}{2} + l^{f-s\langle 1\rangle s(i)}\frac{1}{2}$$

$$+m^{f-s\langle 1\rangle s(i)}\left[\frac{(r-1)^1}{1}-\frac{(r-1)^2}{2}+\frac{(r-1)^3}{3}-\frac{(r-1)^4}{4}+\frac{(r-1)^5}{5}\right]$$

$$+m^{f-s\langle 1\rangle s(i)}r\left[1-(r-1)^1+(r-1)^2-(r-1)^3+(r-1)^4\right]$$

$$S(r) = r\left[1-(r-1)^1+(r-1)^2-(r-1)^3+(r-1)^4\right]$$

$$k^{f-s\langle 1\rangle s(i)} = \left(\frac{1+v^{f-s\langle 1\rangle s(i)}}{1-v^{f-s\langle 1\rangle s(i)}}\right)\left(\alpha^{f-s\langle 1\rangle s(i)}T^{f-s\langle 1\rangle s(i)}+\varepsilon^{s-f-s\langle 1\rangle s(i)}\right)$$

$$l^{f-s\langle 1\rangle s(i)} = \frac{1}{2}\left(\frac{1-2v^{f-s\langle 1\rangle s(i)}}{1-v^{f-s\langle 1\rangle s(i)}}\right)\left(\varepsilon_r^{c-f-s\langle 1\rangle s(i)}+\varepsilon_\theta^{c-f-s\langle 1\rangle s(i)}\right)$$

$$m^{f-s\langle 1\rangle s(i)} = \frac{1}{2}\left(\frac{1-2v^{f-s\langle 1\rangle s(i)}}{1-v^{f-s\langle 1\rangle s(i)}}\right)\left(\varepsilon_r^{c-f-s\langle 1\rangle s(i)}-\varepsilon_\theta^{c-f-s\langle 1\rangle s(i)}\right)$$

150

$$a^{f-s\langle 1\rangle s(i)} = \frac{E^{f-s\langle 1\rangle s(i)}}{1+v^{f-s\langle 1\rangle s(i)}} \;\; [\text{MPa}]$$

$$b^{f-s\langle 1\rangle s(i)} = \frac{v^{f-s\langle 1\rangle s(i)}}{1-2v^{f-s\langle 1\rangle s(i)}}$$

$$c^{f-s\langle 1\rangle s(i)} = -3\left[\alpha^{f-s\langle 1\rangle s(i)}\left(T^{f-s\langle 1\rangle s(i)} - T_0^{f-s\langle 1\rangle s(i)}\right) + \varepsilon^{s-f-s\langle 1\rangle s(i)}\right]$$

$$d_g^{f-s\langle 1\rangle s(i)} = -\left[\alpha^{f-s\langle 1\rangle s(i)}\left(T^{f-s\langle 1\rangle s(i)} - T_0^{f-s\langle 1\rangle s(i)}\right) + \varepsilon^{s-f-s\langle 1\rangle s(i)} + \varepsilon_g^{c-f-s\langle 1\rangle s(i)}\right]$$

$$= \frac{c^{f-s\langle 1\rangle s(i)}}{3} - \varepsilon_g^{c-f-s\langle 1\rangle s(i)} \qquad (g = r,\ \theta,\ \text{or}\ z)$$

$T^{f-s\langle 1\rangle s(i)}$ = average temperature in radial section *<1>* of axial section *(i)* in the fuel

slug region.

When the polynomial solutions are used instead of Equation 2.103 to 2.108 for radial section *<1>* of the fuel, the equations obtained from applying the radial boundary conditions to the solutions, which are included in the simultaneous linear systems of the open-gap model and the closed-gap model, are also changed. The equation obtained from applying the radial boundary condition $\sigma_{r\langle 2\rangle}^{f-s\langle 1\rangle s(i)} = \sigma_{r\langle 2\rangle}^{f-s\langle 2\rangle s(i)}$ to the solutions for the radial stresses in radial section *<1>* and *<2>* becomes

$$
\begin{aligned}
&a^{f-s\langle 1\rangle s(i)}\left(1+2b^{f-s\langle 1\rangle s(i)}\right)C_1^{f-s\langle 1\rangle s(i)} - a^{f-s\langle 2\rangle s(i)}\left(1+2b^{f-s\langle 2\rangle s(i)}\right)C_1^{f-s\langle 2\rangle s(i)} \\
&\qquad + \frac{a^{f-s\langle 2\rangle s(i)}}{\left(r_{\langle 2\rangle}^{f-s(i)}\right)^2}C_2^{f-s\langle 2\rangle s(i)} + \left[a^{f-s\langle 1\rangle s(i)}b^{f-s\langle 1\rangle s(i)} - a^{f-s\langle 2\rangle s(i)}b^{f-s\langle 2\rangle s(i)}\right]C_z^{f-s(i)} \\
&= a^{f-s\langle 2\rangle s(i)}\left[\left(1+2b^{f-s\langle 2\rangle s(i)}\right)X_{\langle 2\rangle}^{f-s\langle 2\rangle s(i)} - b^{f-s\langle 2\rangle s(i)}m^{f-s\langle 2\rangle s(i)} \right. \\
&\left. \qquad\qquad\qquad\qquad\qquad\qquad +b^{f-s\langle 2\rangle s(i)}c^{f-s\langle 2\rangle s(i)} + d_r^{f-s\langle 2\rangle s(i)}\right]
\end{aligned}
\tag{B.7}
$$

151

$$-a^{f-s\langle 1\rangle s(i)}\left[\left(1+2b^{f-s\langle 1\rangle s(i)}\right)X_{series\langle 2\rangle}^{f-s\langle 1\rangle s(i)}-b^{f-s\langle 1\rangle s(i)}m^{f-s\langle 1\rangle s(i)}S_{\langle 2\rangle}\right.$$

$$\left.+b^{f-s\langle 1\rangle s(i)}c^{f-s\langle 1\rangle s(i)}+d_r^{f-s\langle 1\rangle s(i)}\right]$$

where $X_{series\langle 2\rangle}^{f-s\langle 1\rangle s(i)}=k^{f-s\langle 1\rangle s(i)}\dfrac{1}{2}+l^{f-s\langle 1\rangle s(i)}\dfrac{1}{2}$

$$+m^{f-s\langle 1\rangle s(i)}\left[\frac{\left(r_{\langle 2\rangle}^{f-s(i)}-1\right)^1}{1}-\frac{\left(r_{\langle 2\rangle}^{f-s(i)}-1\right)^2}{2}+\frac{\left(r_{\langle 2\rangle}^{f-s(i)}-1\right)^3}{3}\right.$$

$$\left.-\frac{\left(r_{\langle 2\rangle}^{f-s(i)}-1\right)^4}{4}+\frac{\left(r_{\langle 2\rangle}^{f-s(i)}-1\right)^5}{5}\right]$$

$$+m^{f-s\langle 1\rangle s(i)}r_{\langle 2\rangle}^{f-s(i)}\left[1-\left(r_{\langle 2\rangle}^{f-s(i)}-1\right)^1+\left(r_{\langle 2\rangle}^{f-s(i)}-1\right)^2-\left(r_{\langle 2\rangle}^{f-s(i)}-1\right)^3+\left(r_{\langle 2\rangle}^{f-s(i)}-1\right)^4\right]$$

$$S_{\langle 2\rangle}=r_{\langle 2\rangle}^{f-s(i)}\left[1-\left(r_{\langle 2\rangle}^{f-s(i)}-1\right)^1+\left(r_{\langle 2\rangle}^{f-s(i)}-1\right)^2-\left(r_{\langle 2\rangle}^{f-s(i)}-1\right)^3+\left(r_{\langle 2\rangle}^{f-s(i)}-1\right)^4\right].$$

Applying the radial boundary condition $u_{r\langle 2\rangle}^{f-s\langle 1\rangle s(i)}=u_{r\langle 2\rangle}^{f-s\langle 2\rangle s(i)}$ to the solutions for the radial

displacements in radial section *<1>* and *<2>* yields

$$C_1^{f-s\langle 1\rangle s(i)}r_{\langle 2\rangle}^{f-s(i)}-C_1^{f-s\langle 2\rangle s(i)}r_{\langle 2\rangle}^{f-s(i)}-\frac{C_2^{f-s\langle 2\rangle s(i)}}{r_{\langle 2\rangle}^{f-s(i)}}=W_{\langle 2\rangle}^{f-s\langle 2\rangle s(i)}-W_{series\langle 2\rangle}^{f-s\langle 1\rangle s(i)} \qquad (\text{B.8})$$

where $W_{series\langle 2\rangle}^{f-s\langle 1\rangle s(i)}=k^{f-s\langle 1\rangle s(i)}\dfrac{r_{\langle 2\rangle}^{f-s(i)}}{2}+l^{f-s\langle 1\rangle s(i)}\dfrac{r_{\langle 2\rangle}^{f-s(i)}}{2}$

$$+m^{f-s\langle 1\rangle s(i)}\left[\frac{r_{\langle 2\rangle}^{f-s(i)}\left(r_{\langle 2\rangle}^{f-s(i)}-1\right)^1}{1}-\frac{r_{\langle 2\rangle}^{f-s(i)}\left(r_{\langle 2\rangle}^{f-s(i)}-1\right)^2}{2}+\frac{r_{\langle 2\rangle}^{f-s(i)}\left(r_{\langle 2\rangle}^{f-s(i)}-1\right)^3}{3}\right.$$

$$\left.-\frac{r_{\langle 2\rangle}^{f-s(i)}\left(r_{\langle 2\rangle}^{f-s(i)}-1\right)^4}{4}+\frac{r_{\langle 2\rangle}^{f-s(i)}\left(r_{\langle 2\rangle}^{f-s(i)}-1\right)^5}{5}\right]$$

The equations obtained from applying the axial boundary conditions for the open-gap situation and the closed-gap situation to the solutions for axial stresses are also changed in similar ways.

APPENDIX C

INPUT INSTRUCTIONS FOR THE TAMU-ZFP CODE

TAMU-ZFP input instructions are given in Table C.1. For user-convenience purposes, the input of the TAMU-ZFP code adopted the style of the FRAPCON-3 input with which the users of fuel performance codes are already familiar.

TAMU-ZFP was designed to be flexibly applicable to various fuel designs, and it can simulate the metallic fuel pins that have fertile blankets at the top and/or bottom of the fuel slug within the fuel pin, as in the oxide fuel pins. Thus, the code user can feed information on the upper and/or lower blankets via the input. The information on axial sections and time sections is also supplied by the code user, but radial sections are configured by the code for more accurate and efficient computations. The change of the information on the radial sections requires a higher user-level.

Table C.1. Input instructions for the TAMU-ZFP code.

Input variable name	Description	Limitation
timestep	Number of time steps	Should be greater than 0.
transient	Time step at which the transient starts	Should be less than or equal to *timestep*. Steady state only if *transient* = 0.

Table C.1. Continued.

Input variable name	Description	Limitation
tdependency_cool	Time-dependency indicator of thermal-hydraulic parameters	1 = the values of thermal-hydraulic parameters are specified for each time step. 0 = a single value of each parameter is applied to all the time steps.
axsection_fuel	Number of axial sections in the fuel slug region	Should be greater than 0. More than 5 is recommended.
axsection_upb	Number of axial sections in the upper blanket region	No upper blanket if *axsection_upb* = 0.
axsection_lob	Number of axial sections in the lower blanket region	No lower blanket if *axsection_lob* = 0.
axpshape	Indicator for axial power shape	1 = default chopped-cosine shape. 2 = user-specified shape.
num_axprofiles	Number of user-supplied axial power profiles	0 when *axpshape* = 1.
cladtype	Indicator for the type of cladding	1 = SS_304L. 2 = SS_316. 3 = D9. 4 = HT9.
wtpct_pu	Weight percent of plutonium in alloy fuel (wt% Pu)	Should be less than 100.
wtpct_zr	Weight percent of zirconium in alloy fuel (wt% Zr)	Should be less than 100.
smearden	Smeared density of fuel (%TD)	Used to compute the as-cast density.
fradi	Radius of fuel slug [cm]	Should be greater than 0.
cladthi	Thickness of cladding [cm]	Should be greater than 0.
gapthi	Thickness of gap [cm]	Should be greater than 0.
fuelen	Length of fuel slug (or length of a stack of fuel pellets) [cm]	Should be greater than 0.
upblen	Length of upper blanket [cm]	0 when *axsection_upb* = 0.
loblen	Length of lower blanket [cm]	0 when *axsection_lob* = 0.

Table C.1. Continued.

Input variable name	Description	Limitation
plenmlen	Length of gas plenum [cm]	Should be greater than 0.
plenm_ipress	Initial pressure of helium in gas plenum [MPa]	Default = 0.084
sod_level	Sodium level above the fuel slug [cm]	Should be greater than 0.
pin_pitch	Fuel pin pitch (center-to-center distance between pins in a triangular coolant channel) [cm]	Should be greater than the fuel-pin diameter.
time	Array for cumulative time at the end of each time step [day]	The size of the array should be equal to *timestep*. The cumulative time at the beginning of the first time step is 0 [day]. All the values contained in the array should be greater than 0.
lhgr	Array for average linear heat generation rate of the fuel slug at each *time* [W/cm]	The size of the array should be equal to *timestep*. The linear heat generation rates averaged in the fuel slug are treated as a piecewise-constant function of t for the steady-state case and as a piecewise-linear function of t for the transient case. If *transient* = 1, the average LHGR at the beginning of the first time step is 0.
inlet_temp	Array for coolant inlet temperature at each time step [ºC]	When *tdependency_cool* = 1, the size of the array should be equal to *timestep*. When *tdependency_cool* = 0, a single value (not array).

Table C.1. Continued.

Input variable name	Description	Limitation
cmflow	Array for coolant mass flow rate at each time step [g/s]	When *tdependency_cool* = 1, the size of the array should be equal to *timestep*. When *tdependency_cool* = 0, a single value (not array).
cool_press	Array for coolant pressure at each time step [MPa]	When *tdependency_cool* = 1, the size of the array should be equal to *timestep*. When *tdependency_cool* = 0, a single value (not array).
hist_axpro	Array for index of axial power profile used for each time step	Used only if *axpshape* = 2. The size of the array should be equal to *timestep*. All the values contained in the array should be greater than or equal to 1, and should be less than or equal to *num_axprofiles*.
axpro	Array for the ratios of the linear power at each axial node to the axially-averaged value (an array represents an axial power profile and has an individual index for the identification)	Used only if *axpshape* = 2. The number of arrays should be equal to *num_axprofiles*. The size of each array should be equal to the total number of axial nodes. The values in each array are normalized.